Master Thesis

Data-Driven Study of Kilonovae from Binary Neutron Star Mergers

Sahil Jhawar

813093

Institut für Physik und Astronomie
Universität Potsdam

First Supervisor: Prof. Dr. Tim Dietrich
Second Supervisor: Dr. Peter T.H. Pang

।।विद्याधनं सर्वधनप्रधानम्।।

The wealth of knowledge is the most valuable of all wealths.

ABSTRACT

Kilonovae, the potential electromagnetic counterparts to neutron star mergers, offer crucial insights into high-energy transient phenomena and provide a unique opportunity to probe the properties of the sources powering these events. However, significant uncertainties exist in kilonova modeling, which hinder the accurate prediction and interpretation of observational data. These modeling uncertainties, if not properly accounted for, can lead to misinterpretations of key astrophysical parameters.

In this thesis, we present a novel data-driven approach for quantifying time-dependent and filter-dependent systematic uncertainties in kilonova models. By incorporating interpolation schemes that account for the non-stationary behavior of systematic errors, our methodology enhances the reliability of parameter estimation for kilonova events. Through a series of synthetic injection-recovery tests using the KA2017 and BU2019LM models, we validate the effectiveness of our approach in recovering injected parameters within credible intervals.

We apply this method to the observed kilonova `AT2017gfo`, performing parameter estimation with different time node configurations. Our results show that a combination of time- and filter-dependent systematic uncertainties leads to the most reliable recovery of the source parameters. Notably, we find a systematic error of less than 1 magnitude between 1 and 5 days after the merger. Additionally, the model reveals significant insights into the temporal and spectral evolution of systematic uncertainties, indicating the need for both early follow-up observations and improved modeling techniques for later phases of kilonovae. These findings highlight the importance of properly accounting for systematic uncertainties in kilonova modeling, contributing to more precise multi-messenger astronomy and offering a robust framework for future transient event studies.

ZUSAMMENFASSUNG

Kilonovae, die potenziellen elektromagnetischen Folgeerscheinungen von Neutronensternverschmelzungen, bieten entscheidende Einblicke in hochenergetische kurzlebige Phänomene und eine außergewöhnliche Gelegenheit, die Beschaffenheit der Quellen zu untersuchen, die diese Erscheinungen verursachen. Allerdings bestehen bei der Modellierung von Kilonovae erhebliche Unsicherheiten, die eine genaue Vorhersage und Interpretation von Beobachtungsdaten erschweren. Diese Modellierungsunsicherheiten können, wenn sie nicht richtig berücksichtigt werden, zu Fehlinterpretationen wesentlicher astrophysikalischer Parameter führen.

In dieser Arbeit stellen wir einen neuen datengesteuerten Ansatz zur Quantifizierung von zeit- und filterabhängigen systematischen Unsicherheiten in Kilonova-Modellen vor. Durch die Einbeziehung von Interpolationsmethoden, die das nicht-stationäre Verhalten von systematischen Fehlern berücksichtigen, verbessert unsere Methodik die Zuverlässigkeit der Parameterschätzung für Kilonova-Ereignisse. Durch eine Reihe von synthetischen Injection-Recovery-Tests unter Verwendung der Modelle KA2017 und BU2019LM testen wir unseren Ansatz zur Wiederherstellung der injizierten Parameter innerhalb von Glaubwürdigkeitsintervalle.

Wir wenden diese Methode für das gemessene Kilonova Signal `AT2017gfo` an und führen eine Parameterschätzung mit verschiedenen Konfigurationen der Beobachtungszeiten durch. Unsere Ergebnisse zeigen, dass eine Kombination aus zeit- und filterabhängigen systematischen Unsicherheiten die zuverlässigste Ermittlung der Quellparameter ermöglicht. Insbesondere finden wir einen systematischen Fehler von weniger als einer Magnitude zwischen einem und fünf Tagen nach der Verschmelzung. Darüber hinaus liefert das Modell wichtige Erkenntnisse über die zeitliche und spektrale Entwicklung der systematischen Unsicherheiten und zeigt, dass sowohl frühe Messungen als auch verbesserte Modellierungstechniken für spätere Phasen der Kilonovae notwendig sind. Diese Ergebnisse verdeutlichen wie wichtig die Berücksichtigung von systematische Unsicherheiten bei der Modellierung von Kilonovae ist. Unsere Methode bietet einen robusten Rahmen für zukünftige Studien dieser Ereignisse und trägt damit zu einer genaueren Multi-Messenger-Astronomie bei.

Thank you Anna N. for the translation.

Declaration of Authorship

I, Sahil Jhawar, declare that this thesis titled, *Data-Driven Study of Kilonovae from Binary Neutron Star Mergers* and the work presented in it are my own. I confirm that:

- This work was done wholly while in candidature for a research degree at the University of Potsdam.

- Where I have consulted the published work of others, this is always clearly attributed.

- Where I have quoted from the work of others, the source is always given. With the exception of such quotations, this thesis is entirely my own work.

- I have acknowledged all main sources of help.

- This thesis uses first-person plural pronouns (we, our) to refer to the author and collaborators, acknowledging the collaborative nature of the research, with the author having contributed majorly to all analyses and work presented.

In addition, I acknowledge the use of AI tools, including ChatGPT, Claude, Grok and Grammarly, to help structure and refine the flow of this thesis. Additionally, I utilized AI search engines like Perplexity to assist in finding relevant references and supporting materials. These tools significantly contributed ensuring coherence and depth in this thesis.

Potsdam	April 16, 2025	Sahil Jhawar
Place	Date	Author's signature

Acknowledgement

Published Papers

During the course of this thesis, I lead one paper and contributed to another. Additionally, the method developed in the early stages of this thesis was utilized in a third paper.

- Sahil Jhawar et al. Data-driven approach for modeling the temporal and spectral evolution of kilonova systematic uncertainties. *Phys. Rev. D*, 4 **2025**.
  DOI: 10.1103/PhysRevD.111.043046 ArXiv: 2410.21978 [astro-ph.HE]

- Malina Desai et al. Kilonova Light Curve Parameter Estimation Using Likelihood-Free Inference. **2024**.
  ArXiv: 2408.06947 [astro-ph.IM] URL: https://arxiv.org/abs/2408.06947

- T. Hussenot-Desenonges et al. Multiband analyses of the bright GRB 230812B and the associated SN2023pel. *Mon. Not. Roy. Astron. Soc.*, **2024**.
  DOI: 10.1093/mnras/stae503 ArXiv: 2310.14310 [astro-ph.HE]

Contents

List of Figures

List of Abbreviations

BNS	Binary Neutron Star
EFE	Einstein Field Equations
EM	Electromagnetic
EOS	Equation Of State
GPR	Gaussian Process Regression
GRB	Gamma-ray Burst
GW	Gravitational Waves
LIGO	Laser Interferometer Gravitational-Wave Observatory
MCMC	Markov Chain Monte Carlo
MCRT	Monte Carlo Radiative Transfer
NMMA	Nuclear-Physics And Multi-Messenger Astrophysics
NN	Neural Network
NSBH	Neutron Star-black Hole
PDF	Probability Density Function
RTE	Radiative Transfer Equation
SVD	Singular Value Decomposition
TOV	Tolman-Oppenheimer-Volkoff

1 Introduction

The detection of the binary neutron star (BNS) merger GW170817 [4,5] on August 17, 2017, by the Advanced Laser Interferometer Gravitational-Wave Observatory (LIGO) [6] and Advanced Virgo [7] marked a watershed moment in multimessenger astronomy. This event, accompanied by the short gamma-ray burst (GRB) GRB170817A detected by NASA's Fermi Gamma-ray Space Telescope [8] and the European Space Agency's INTEGRAL [9], and followed by the kilonova AT2017gfo [10,11] observed in the galaxy NGC4993, provided an unprecedented opportunity to study the Universe through multiple messengers: gravitational waves (GW) and electromagnetic (EM) waves. Occurring approximately 40Mpc away, GW170817 signature chirp lasted nearly 100 seconds, far longer than typical black hole merger signals, indicated the collision of two neutron stars with masses of about 1.1 and 1.6 solar masses, confirmed by the near-instantaneous gamma-ray flash just 1.74 seconds later. This joint detection, the first of its kind, alerted astronomers worldwide, leading to a follow-up campaign that captured the fading glow of AT2017gfo, interpreted as a kilonova—an EM transient powered by the radioactive decay of r-process elements synthesized during the merger.
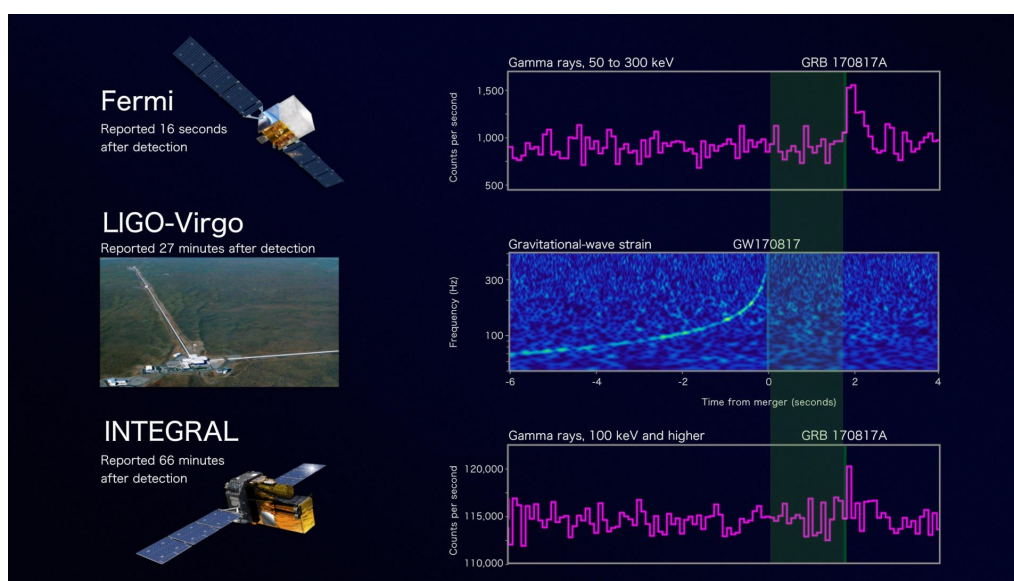
Figure 1.1: The middle panel shows the gravitational wave strain. The top and bottom panel shows the gamma-ray observations from Fermi and INTEGRAL, respectively. The shaded region indicates the 1.74 seconds delay between the GW and GRB detections. Image credit: ESA

The significance of GW170817 extends across multiple fields, enhancing our understanding of cosmology and Hubble tension [12-21], nuclear physics [4,19,22-28], modified gravity theories [29-31], and the chemical evolution of the Universe [32-37]. While GW170817 remains the only confirmed multimessenger BNS merger, observational evidence suggests that GW190425 [38], GRB211211 [39-41], and GRB230307A [42]

may also originate from similar mergers, hinting at an increasing likelihood of future detections as observational facilities improve.
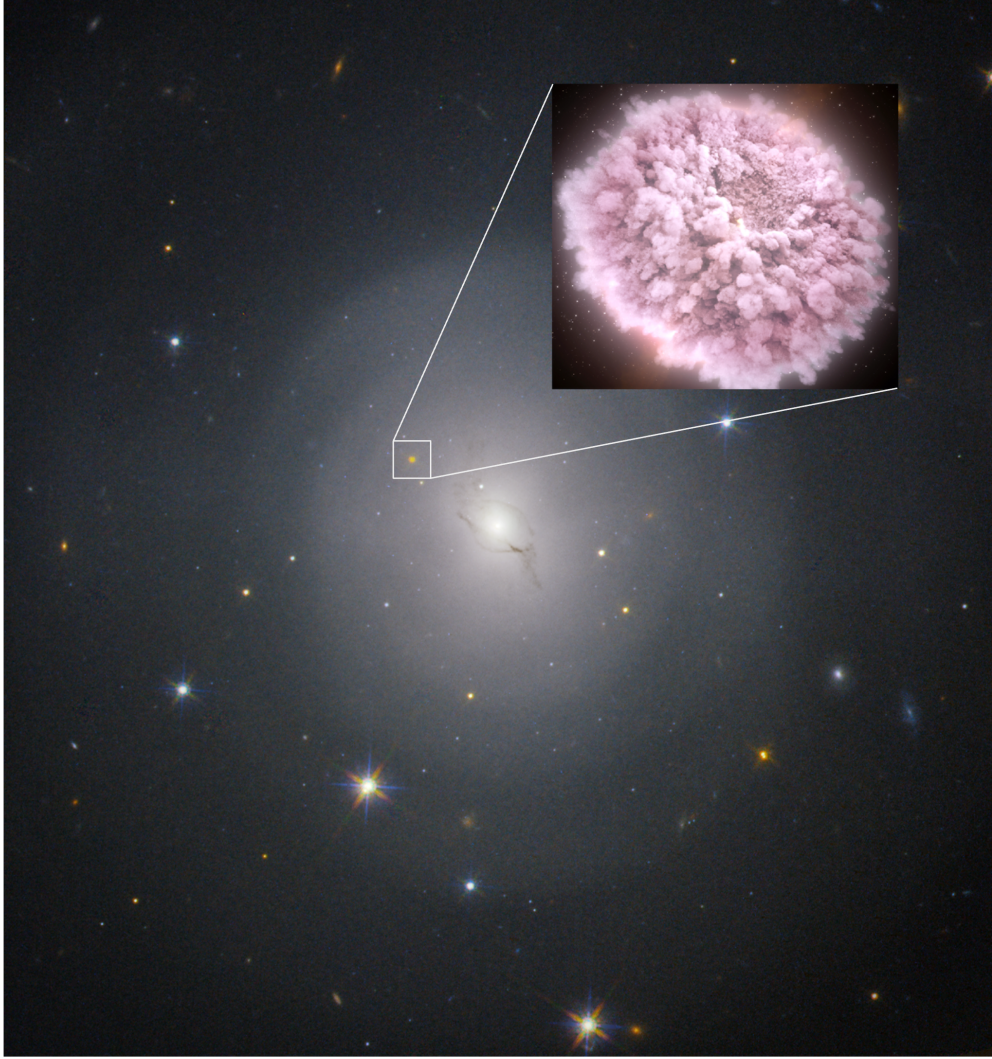
Figure 1.2: Galaxy NGC4993 as captured by Hubble showing the location of AT2017gfo. The inset shows the artistic rendition of red component of the kilonova. Image credit: NASA

The interpretation of `GW170817` and future multimessenger events relies on comparing observational data with robust theoretical models. For GWs, systematic uncertainties are well-controlled for current detectors [43–47], though next-generation observatories like the Einstein Telescope [48–50] and Cosmic Explorer [51] will demand even higher precision. However, with the EM counterpart, the challenges are more complex. Kilonovae, spanning optical, ultraviolet, and infrared wavelengths, are driven by the radioactive decay of unstable heavy elements formed via r-process nucleosynthesis [52,53]. Despite progress from simplified semi-analytical models [11,37,53–60] to sophisticated 3D radiative transfer simulations [61–66] uncertainties persist in ejecta properties (mass, velocity, composition) [67–71],

nuclear heating rates, thermalization efficiencies, and opacities of r-process elements [72–79]. These uncertainties, if unaddressed, risk biasing parameter estimates even if the data quality improves.

This thesis investigates how these uncertainties evolve over time and per filter, and how they impact the inferred ejecta properties of kilonovae. By leveraging the Nuclear-Physics and Multi-Messenger Astrophysics (NMMA) framework and high-fidelity radiative transfer simulations from `POSSIS` [64], we aim to develop a more robust methodology for incorporating time- and filter-dependent uncertainties into kilonova analyses [1]. Our study focuses on `AT2017gfo`, the best-observed kilonova to date, as a case study to assess the effects of evolving systematic uncertainties on light curve modeling and parameter estimation. The insights gained from this work will contribute to refining kilonova models for future multimessenger detections.

2 Anatomy of a Binary Neutron Star Merger

2.1 Neutron Stars

Neutron stars emerge from the remnants of massive stars after a supernova explosion expels the outer layers, leaving a core that collapses under gravity. When the core's mass exceeds the Chandrasekhar limit (approximately $1.4\ M_\odot$), electron capture and neutronization convert protons and electrons into neutrons. If the core mass exceeds a critical value (around $2-3\ M_\odot$), the collapse continues until neutron degeneracy pressure, supported by strong nuclear interactions at extreme densities, halts further collapse and forms a neutron star. Fig. 2.1 →p.4 illustrates the evolution of a BNS system, highlighting the potential outcomes based on the masses and rotational energy of the remnant.
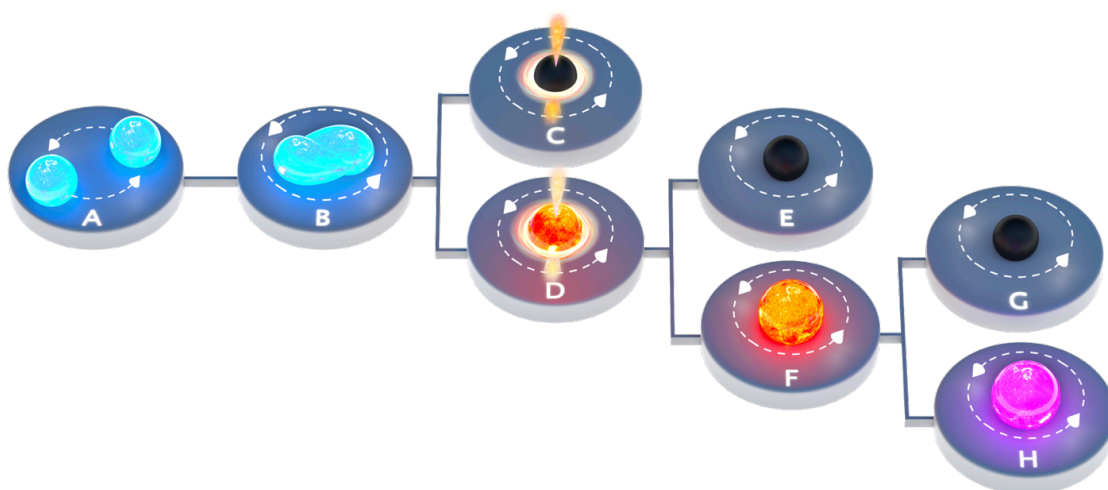
Figure 2.1: Fate of a BNS system depending on the masses and the rotational energy of the remnant. Post merger, the BNS may collapse to a black hole (C), form a neutron star (D), or evolve into a hypermassive neutron star that collapses to a black hole after losing angular momentum or remain a stable neutron star (E, F, G, H). Image credit: Ref. [80]

2.1.1 Tolman-Oppenheimer-Volkoff Equation

The Tolman-Oppenheimer-Volkoff equations [81,82] describe the structure of a static, spherically symmetric neutron star in general relativity, extending Newtonian hydrostatic equilibrium to account for relativistic effects. They emerge from solving the Einstein Field Equations [83] for a fluid ball under these conditions, providing the pressure, density, and mass profiles as functions of radius.

In Newtonian mechanics, the balance between gravitational and pressure forces in

a spherical body is governed by the equation of hydrostatic equilibrium. However, as the density increases to extreme levels within compact objects like neutron stars, relativistic corrections become essential. The TOV equations are derived from the Einstein Field Equations for a perfect fluid, under the assumptions of staticity (no motion) and spherical symmetry. The general relativistic metric for a static, spherically symmetric star is given by

$$ds^2 = -e^{2\Phi(r)}dt^2 + e^{2\lambda(r)}dr^2 + r^2(d\theta^2 + \sin^2\theta d\phi^2), \tag{2.1}$$

where $\Phi(r)$ and $\lambda(r)$ are functions of the radial coordinate r, representing the gravitational potential and the space-time curvature, respectively. The perfect fluid model is described by the stress-energy tensor $T_{\mu\nu}$, which for a static, spherically symmetric star takes the form,

$$T_{\mu\nu} = (\rho + p)u_\mu u_\nu + pg_{\mu\nu}, \tag{2.2}$$

where ρ is the energy density, p is the pressure, and u_μ is the four-velocity of the flluid.

The TOV equations are derived by solving the EFE with the metric in $\boxed{\text{Eq. (2.1)}^{\rightarrow\text{p.5}}}$ and the stress-energy tensor in $\boxed{\text{Eq. (2.2)}^{\rightarrow\text{p.5}}}$, yielding three first-order differential equations

$$\frac{dM(r)}{dr} = 4\pi r^2 \rho(r) \tag{2.3a}$$

$$\frac{dP(r)}{dr} = -\frac{Gm(r)\rho(r)}{r^2}\left(1 + \frac{P(r)}{\rho(r)}\right)\left(1 + \frac{4\pi r^3 P(r)}{m(r)}\right)\left(1 - \frac{2Gm(r)}{r}\right)^{-1} \tag{2.3b}$$

$$\frac{d\Phi(r)}{dr} = -\frac{1}{\rho + P(r)}\frac{dP(r)}{dr}, \tag{2.3c}$$

where $M(r)$ is the mass enclosed within radius r, and $P(r)$ is the pressure at that radius.

$\boxed{\text{Eq. (2.3a)}^{\rightarrow\text{p.5}}}$ expresses the mass conservation within a spherical shell of radius r, $\boxed{\text{Eq. (2.3b)}^{\rightarrow\text{p.5}}}$ describes the pressure gradient in the star, balancing the gravitational force with the pressure gradient, and $\boxed{\text{Eq. (2.3c)}^{\rightarrow\text{p.5}}}$ relates the gradient of the gravitational potential to the pressure gradient, essentially describing how the spacetime metric varies throughout the star. The TOV equations are typically solved numerically to obtain the mass, radius, and density profiles of neutron stars, providing insights into their structure and properties.

2.1.2 Equation of State

The TOV equations are fundamentally dependent on the equation of state (EOS) of neutron star material, which defines the relationship between pressure P and density ρ. The EOS encapsulates the microphysics of ultra-dense matter, governing

how neutron stars resist gravitational collapse under extreme conditions. However, the EOS at supranuclear densities ($\gtrsim 10^{14}$ g/cm^3) remains poorly constrained due to limitations in terrestrial experiments and theoretical uncertainties in quantum chromodynamics and nuclear interactions.

For instance, a soft EOS, characterized by lower pressures at high densities, results in greater compressibility, yielding smaller and less massive neutron stars with radii typically around $10 - 11$ km and maximum masses closer to $1.4 - 2\ M_\odot$ [84]. Conversely, a stiff EOS, with higher pressures resisting compression, supports more massive neutron stars—potentially exceeding 2.5 $M_\odot$ with larger radii, up to 13 km [27,85]. These variations arise because the TOV pressure gradient balances gravity more effectively with a stiff EOS, allowing greater mass accumulation before collapse to a black hole occurs, as supported by recent observational constraints from NICER and GW170817 [27,86].
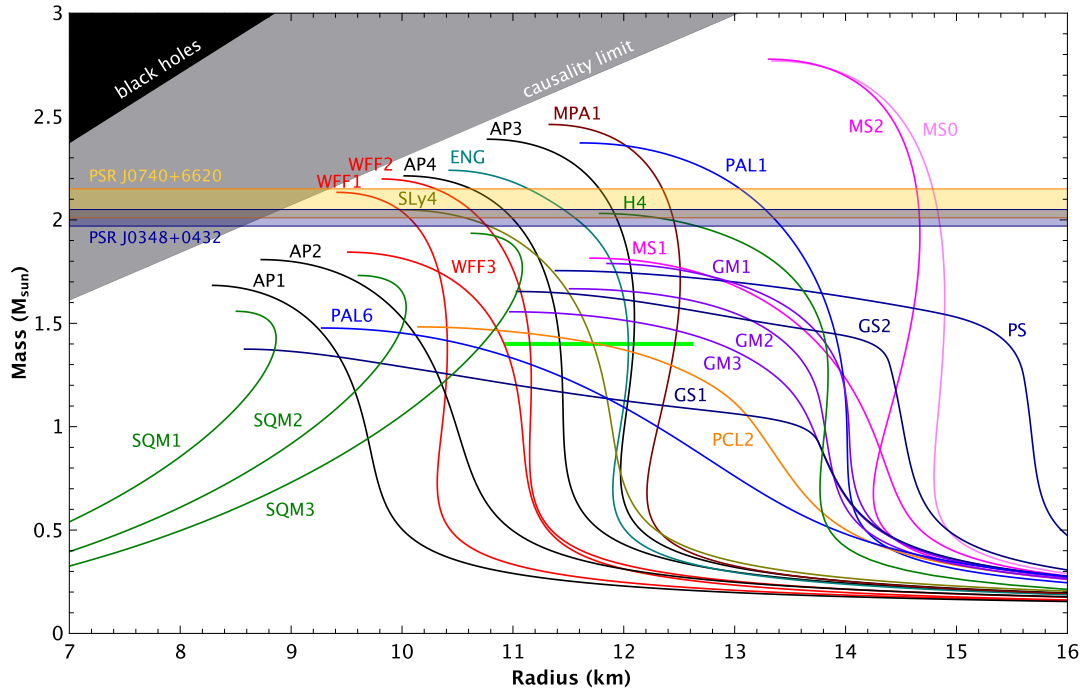
Figure 2.2: Mass-Radius curves made using several equation of states. Image credit: Norbert Wex for MPIfR

2.2   Kilonova

Kilonovae, transient electromagnetic events are triggered by the merger of neutron stars or a neutron star and a black hole. The name *kilonova* [87] stems from their luminosity, which sits roughly 1000 times above that of a classical nova yet below a typical supernova [52]. Kilonovae are characterized by their multi-wavelength emission, spanning optical, ultraviolet, and infrared bands, and exhibit a distinctive

light curve evolution over time. Few of the first possible kilonova candidates were observed as the aftermath of the short gamma-ray bursts include GRB060614 [88,89], GRB070809 [90], GRB080503 [91] GRB130603B [92], followed by the detection of AT2017gfo associated with the binary neutron star merger GW170817 [10,11].[1]

The kilonova's optical and infrared emission, peaking within a few days to weeks post-merger, is powered by the radioactive decay of r-process elements, primarily lanthanides and actinides, synthesized during the merger. The decay chain of these heavy elements releases a large amount of energy, heating the ejecta and driving the kilonova's luminosity. The kilonova's spectral evolution is characterized by a blue to red color transition, reflecting the changing composition and temperature of the expanding ejecta.

The early blue emission, peaking in the ultraviolet and optical bands, arises from the radioactive decay of light r-process elements, while the later red emission, peaking in the infrared, is powered by the decay of heavier elements. The kilonova's light curve exhibits a rapid rise to peak luminosity, followed by a gradual decline over weeks to months as the ejecta cools and expands. The kilonova's peak luminosity, color, and duration depend on the ejecta mass, velocity, composition, and thermalization efficiency, making them valuable probes of the merger dynamics and the properties of neutron star matter. Theoretical models of kilonovae have evolved from simple analytical prescriptions [52,87] to sophisticated radiative transfer simulations [61–66], capturing the complex interaction between nuclear heating, radiative transport, and opacities of r-process elements.

2.2.1 Ejecta Properties

The material ejected during a neutron star merger forms the basis of a kilonova, driving its observable signatures through radioactive decay and thermal emission. Ejecta originate from multiple mechanisms, each contributing distinct mass, velocity, and compositional profiles that shape the resulting light curves and spectra.

2.2.1.1 Dynamical Ejecta

Dynamical ejecta from NS-NS mergers consist of matter expelled on the characteristic dynamical timescale (~ 10ms) of the system, with typical masses on the order of $10^{-4} - 10^{-2}\,M_\odot$ and velocities of $0.1 - 0.3c$ [93–96]. The total mass of this ejecta depends strongly on the binary's total mass, its mass ratio, and the neutron star EOS. Eccentric NS-NS mergers can yield higher ejecta masses [97,98], but such mergers likely occur less frequently in nature due to the high stellar densities required for significant dynamical capture events [99]. Simulations also indicate that very high neutron star spin can enhance the amount of dynamically ejected

---

[1]Even though a number of GRBs have been associated with neutron star mergers (these associations arise due to the lack of a supernova like component in the spectral features of these GRBs), AT2017gfo/GRB170817A/GW170817 is the only confirmed kilonova candidate so far.

matter [100–102]. When a neutron star merges with a black hole (NSBH), the tidal disruption of the star by the black hole can unbind up to $\sim 0.1\,M_\odot$ of material, typically at similar velocities to those in NS-NS collisions [103–105].

In NS-NS systems, two hydrodynamical processes dominate the dynamical ejection. First, the contact interface between merging stars experiences strong compression and shock heating, which drives material outward as the remnant undergoes quasi-radial pulsations [93,106,107]. This "shock-driven" component of the ejecta emerges in a broad range of angular directions. Second, tidal interactions form spiral arms in the equatorial plane, and angular momentum redistribution within these arms propels additional matter outward. The relative importance of these mechanisms depends on the binary mass ratio, strongly asymmetric mergers ($q \ll 1$) tend to eject more mass [107,108]. Ejecta masses also decrease if the remnant collapses promptly into a black hole, since prompt collapse swallows the shocked interface region before much matter can be expelled.

In NSBH mergers, the dominant ejection mechanism is a tidal disruption of the neutron star by the black hole, which also focuses the outflow in the equatorial plane [104,109]. The azimuthal extent of this tidal ejecta can be limited, implying that kilonova emission may depend more sensitively on viewing angle in NSBH systems than in NS-NS mergers.

Besides mass and velocity, the electron fraction Y_e (ratio of protons to total nucleons) of the dynamical ejecta is crucial for determining its role in r-process nucleosynthesis and kilonova emission. Early simulations that neglected weak interactions found that merger outflows are highly neutron-rich ($Y_e \lesssim 0.1$), suggesting robust production of heavy elements with $A \gtrsim 130$ through fission recycling [107,110–112]. More recent calculations that include electron captures and neutrino irradiation reveal a broader range of electron fractions $Y_e \sim 0.1-0.4$, thereby allowing for the synthesis of lighter r-process elements as well [94,113,114]. In NS-NS mergers, the higher Y_e ejecta tends to be more isotropic, whereas the lower Y_e (and hence lanthanide-rich) material often remains concentrated in the equatorial plane, reflecting its origin in the tidal arms. This results in lanthanide-rich tidal ejecta ($Y_e < 0.25$) and lanthanide-poor polar ejecta ($Y_e > 0.25$), influencing the kilonova's spectral evolution and color.

2.2.1.2 Wind Ejecta

Wind ejecta are launched after the merger from the accretion disk or the central compact object, in contrast to the dynamical ejecta expelled promptly during the coalescence phase. The formation of a massive accretion disk (on the order of 0.01–0.3 $M_\odot$) is well established in numerical simulations and depends sensitively on the total mass of the binary, the mass ratio, the spins of the merging bodies, and the neutron star equation of state [53,115,116]. Prompt collapse of the merger remnant into a black hole typically leads to lower disk masses because there is little time for the remnant to redistribute its mass and angular momentum prior to collapse [117].

Once the disk forms, a combination of neutrino heating, magnetic stresses, and nuclear recombination drives sustained mass loss on timescales ranging from milliseconds to seconds. During the earliest, high-accretion phase, strong neutrino irradiation from the disk (and, if present, a hypermassive neutron star) can unbind material from the disk surface [118]. If the central neutron star survives for longer than ~ 50 ms, additional neutrino luminosity from the star itself ejects non-negligible amounts of mass [119-121], potentially enhanced further by spiral density waves excited in the disk [122]. Over time, as the disk expands viscously and its temperature drops, it transitions from an initially neutrino-cooled configuration to a radiatively inefficient, geometrically thicker state [116,123-125]. In this later phase, weak interactions "freeze out," allowing the outflows to remain neutron-rich [123,126].

The wind outflows typically attain velocities of 0.1–0.3c and can have electron fractions Y_e spanning a broad range, from below 0.25 to above 0.3, depending on the level and duration of neutrino irradiation [117,127,128]. Outflows with lower Y_e remain rich in lanthanides and produce red or infrared components of the kilonova, while higher-Y_e material can generate bluer emission [129,130].

Numerical simulations find that the fraction of the disk ultimately ejected through these winds can be substantial, ranging from a few percent for low black hole spin to as high as 30–40% or more for rapidly spinning black holes [117,127,131,132]. Even higher fractions, up to $\sim 90\%$ of the disk, may be unbound if the central remnant remains a long-lived neutron star instead of collapsing promptly to a black hole [133,134]. The wind outflows typically attain velocities of 0.1–0.3c and can have electron fractions Y_e spanning a broad range, from below 0.25 to above 0.3, depending on the level and duration of neutrino irradiation [117,127,128].

Magnetic fields also play a crucial role in shaping the wind dynamics. Turbulence generated by the magneto-rotational instability transports angular momentum outward and boosts mass loss. If the neutron star remnant is backed by a strong, large-scale magnetic field ($\sim 10^{14}$–10^{15} G), additional outflows can be driven centrifugally along open field lines [135,136]. Although the exact origin and geometry of these large-scale fields remains under investigation, they may account for particularly fast ejecta components observed in kilonovae such as GW170817 [137].

Overall, wind ejecta from the disk and central remnant can rival or exceed the mass of the prompt dynamical ejecta and thus represent a significant channel for both mass loss and the synthesis of heavy elements in neutron star mergers [128,131,138]. Their observed features, especially the broad range of velocities and electron fractions indicate that wind-driven outflows are key contributors to the multi-wavelength kilonova emission, often shaping the luminosity and color evolution on timescales of hours to days after the merger.
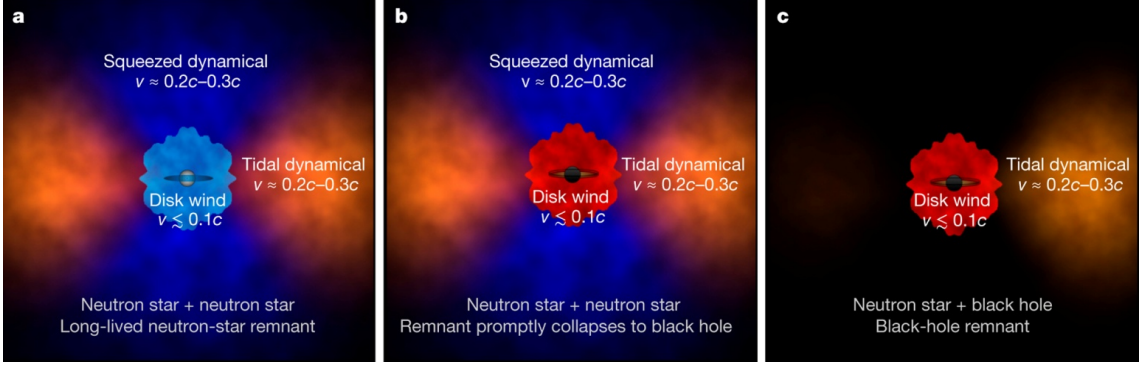
Figure 2.3: Red colours denote regions of heavy r-process elements, which radiate red/infrared light. Blue colours denote regions of light r-process elements which radiate blue/optical light. During the merger, tidal forces peel off tails of matter, forming a torus of heavy r-process ejecta in the plane of the binary. Material squeezed into the polar regions during the stellar collision can form a cone of light r-process material. Roughly spherical winds from a remnant accretion disk can also contribute, and are sensitive to the fate of the central merger remnant. **(a):** If the remnant survives as a hot neutron star for tens of milliseconds, its neutrino irradiation lowers the neutron fraction and produces a blue wind. **(b):** If the remnant collapses promptly to a black hole, neutrino irradiation is suppressed and the winds may be red. **(c):** In the merger of a neutron star and a black hole, only a single tidal tail is ejected, and the disk winds are more likely to be red. Image and caption credit: Ref. [35]

2.2.2   Chemical Composition

The chemical composition of kilonova ejecta, determined by the electron fraction Y_e, governs nucleosynthesis pathways and radiative properties of the emitted light. Y_e governs the neutron-to-proton ratio during the r-process, which occurs in the neutron-rich conditions immediately following ejection. In neutron-rich conditions ($Y_e < 0.25$) typical of tidal dynamical ejecta, enables the rapid neutron capture process onto the seed nuclei, producing isotopes far beyond the stability line that decay into heavy r-process elements, including lanthanides and actinides [139]. These elements, with their dense forest of atomic transitions, yield opacities of $\kappa \sim 10 - 100$ cm^{2}g^{-1}, reddening emission and delaying photon escape [53].

On the other hand, the lanthanide-free ejecta ($Y_e > 0.25$) prevalent in disk wind ejecta and polar dynamical ejecta exposed to neutrino irradiation, limits neutron availability, yielding lighter r-process elements such as Strontium [36] and Yttrium [140]. These elements exhibit simpler atomic structures, resulting in opacities of $\kappa \sim 1 - 10$ cm^{2}g^{-1}, permitting greater photon escape in the optical and ultraviolet bands. The transition between these regimes is not sharp; realistic ejecta likely feature Y_e gradient, blending lanthanide-rich and lanthanide-free regions within a single outflow [11]. This gradient complicates radiative transfer calculations but explains the multi-peaked light curves observed in events like AT2017gfo.
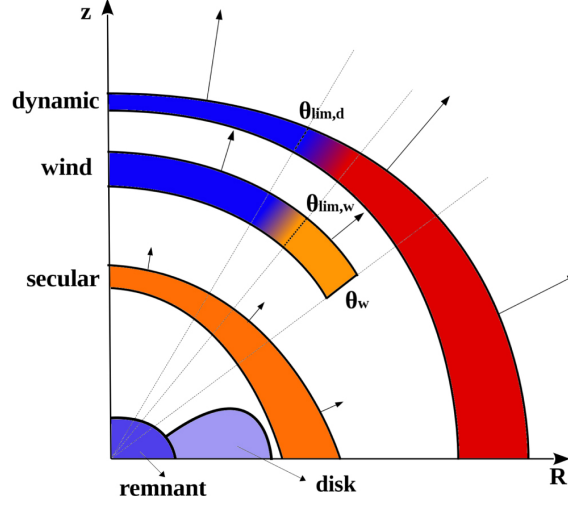
Figure 2.4: Graphical sketch of the three ejecta components radially expanding from the remnant. Different colors correspond to different matter opacity: high (red), intermediate (orange), and low (blue). Image and caption credit: Ref. [11]

2.2.3   Heating

The primary energy source of kilonovae lies in the radioactive decay of r-process nuclei within the ejecta, a process that heats the material and sustains its thermal emission. This decay process releases energy through beta decay, alpha decay, and fission, producing gamma rays, electrons, and neutrinos that deposit heat into the surrounding material [87]. Following Refs. [53,111], this heating rate can be expressed as

$$\dot{Q}_{r,v} = \delta M_v X_{r,v} \dot{e}_r(t), \tag{2.4}$$

where $X_{r,v}$ is the r-process mass fraction in mass layer M_v and e_r is the specific heating rate. For $Y_e \lesssim 0.25$ i.e. neutron-rich ejecta $\dot{e}_r$ can be approximated as

$$\dot{e}_r = 4 \times 10^{18} \varepsilon_{\text{th},v} \left(0.5 - \pi^{-1} \arctan[(t - t_0)/\sigma]\right)^{1.3} \text{erg s}^{-1}\text{ g}^{-1}, \tag{2.5}$$

where $t_0 = 1.3$s and $\sigma = 0.11$s are constants, and $\varepsilon_{\text{th,m}}$ is the thermalization efficiency. While Eq. (2.5) $^{\rightarrow \text{p.11}}$ describes a constant heating rate during the first second of the kilonova, the later times can be well approximated by a power-law decay as reflecting the cumulative contribution of multiple r-process isotopes decay,

$$\dot{e}_r \underset{t \gg t_0}{\approx} 2 \times 10^{10} \varepsilon_{th,v} \left(\frac{t}{1 \text{ day}}\right)^{-1.3} \text{erg s}^{-1}\text{ g}^{-1}. \tag{2.6}$$

This power-law behavior characterizes the long-term energy deposition that sustains kilonova emission over days to weeks.

2.2.4   Emission

The emission from kilonovae emerges as thermal radiation from the heated ejecta, evolving as photons diffuse through the expanding material. Initially, the ejecta are

optically thick, meaning radiation remains trapped until the diffusion timescale is reached, approximated by,

$$t_{\text{diff}} \sim \frac{3M\kappa}{4\pi R c},$$

(2.7)

where κ is the opacity, M is the mass of radius R, asumming an uniform average density. Until the expansion timescale $t_{\text{diff}} = t$ (Arnett's Law [141]) is reached, the diffusion time decreases with $t_{\text{diff}} \propto t^{-1}$ as the ejecta expands and eventually the radiation escapes the ejecta. The peak luminosity of the kilonova occurs when the diffusion time matches the expansion time, marking the transition from the optically thick to the optically thin regime, given by,

$$t_{\text{peak}} \equiv \left(\frac{3M\kappa}{4\pi\beta v c}\right)^{1/2} \approx 1.6 \text{ d} \left(\frac{M}{10^{-2}M_\odot}\right)^{1/2} \left(\frac{v}{0.1c}\right)^{-1/2} \left(\frac{\kappa}{1 \text{ cm}^2 \text{ g}^{-1}}\right)^{1/2},$$

(2.8)

where $\beta \approx 3$ depends on the density profile of the ejecta [107]. By varying the opacity κ over a broad range from lanthanide-free to lanthanide-rich matter ($0.5 - 30 \text{ cm}^2\text{g}^{-1}$ [142]), Eq. (2.8)$^{\rightarrow\text{p.12}}$ yeilds characteristic kilonova durations from 1 day to 1 week.

2.3 Toy Model

From Eq. (2.8)$^{\rightarrow\text{p.12}}$, it is evident that kilonova observables are sensitive to the ejecta mass, velocity, opacity and the sources contributing to the ejecta heating $\dot{Q}(t)$. As discussed in Sec. 2.2.1$^{\rightarrow\text{p.7}}$ and Sec. 2.2.2$^{\rightarrow\text{p.10}}$, the different ejecta components and their characteristics can be combined to model the overall kilonova emission. Following from Sec. 2.2.3$^{\rightarrow\text{p.11}}$, we construct a one-dimensional analytical toy model from Ref. [53], under the assumption of homologous expansion [143]. In this framework, the velocity of the ejecta is proportional to its distance from the merger center and can be expressed as,

$$v_i = \frac{r_i}{t - t_{\text{merger}}},$$

(2.9)

where r_i is the radius of the material at time $t - t_{\text{merger}}$. In simpler terms, this implies that material located farther from the center moves at a higher velocity. We first describe the mass distribution of the ejecta, to this end we define it as a power-law function of the velocity,

$$M_v = M\left(\frac{v}{v_0}\right)^{-\beta}, v \geq v_0,$$

(2.10)

where M is the total mass of the ejecta, v_0 is the minimum velocity of the ejecta, and β is the power-law index and takes the value ≈ 3. Given the simplicity of this model and complexity of numerical simulations, a single power-law index cannot truly capture the diversity of ejecta properties, however this framework is flexible enough in order to use multiple power-law indices to describe the ejecta mass distribution.

Similar to Eq. (2.7) →p.12, the radiation escapes from a given mass layer M_v on a diffusion timescale $t_{d,v}$, which can be expressed as,

$$t_{d,v} = \frac{3 M_v \kappa_v}{4 \pi \beta R_v c},$$

(2.11)

where κ_v is the opacity of the mass layer M_v and $R_v = vt$ reflects the homologously expanding ejecta. Subsitiuting the power-law distribution Eq. (2.10) →p.12 into the diffusion timescale, we obtain,

$$t_{d,v} = \frac{M_v^{4/3} \kappa_v}{4 \pi M^{1/3} v_0 t c}.$$

(2.12)

Setting $t_{d,v} = t$ defines the mass depth from which radiation peaks at time t

$$M_v(t) = \begin{cases} M(t/t_{\text{peak}})^{3/2}, & t < t_{\text{peak}} \\ M & t > t_{\text{peak}} \end{cases},$$

(2.13)

where t_{peak} is the time when diffusion occurs through the entire ejecta mass, typically evaluated at $v = v_0$. Outer layers (lower M_v) emit first, while the innermost shell ($M_v \sim M$) peaks at t_{peak}, often dominating the total light curve unless heating rates or opacities vary significantly with depth (e.g., due to free neutrons in outer layers). As the ejecta expands, the radius of each mass layer evolves simply as:

$$\frac{dR_v}{dt} = v,$$

reflecting free expansion. The thermal energy δE_v of a layer with mass δM_v evolves according to

$$\frac{d(\delta E_v)}{dt} = -\frac{\delta E_v}{R_v} \frac{dR_v}{dt} - L_v + \dot{Q},$$

(2.14)

where the first term represents adiabatic losses due to expansion, L_v is the luminosity, and $\dot{Q}$ accounts for heating sources. The luminosity is given by,

$$L_v = \frac{\delta E_v}{t_{d,v} + t_{lc,v}},$$

(2.15)

where $t_{lc,v} = R_v/c$ (the light-crossing time) ensures energy loss does not exceed physically realistic limits, particularly when the layer becomes optically thin. Heating arises from multiple mechanisms

$$\dot{Q}(t) = \dot{Q}_{r,v} + \dot{Q}_{\text{mag}} + \dot{Q}_{\text{fb}},$$

(2.16)

including radioactive decay ($\dot{Q}_{r,v}$), a millisecond magnetar ($\dot{Q}_{\text{mag}}$), or fallback accretion ($\dot{Q}_{\text{fb}}$). For radioactive heating, the energy input is typically smaller than the initial kinetic energy, allowing the initial power-law distribution to hold. However,

significant energy contribution from a central engine restricts the free expansion. In such cases, the innermost shell's velocity v_0 (mass M, energy E_{v_0}) evolves as,

$$Mv_0\frac{dv_0}{dt} = \frac{E_{v_0}}{R_0}\frac{dR_0}{dt}, \tag{2.17}$$

where R_0 is the inner shell's radius, and the right-hand side balances adiabatic losses, neglecting relativistic effects (at $M_{\rm ej} \lesssim 10^{-2}\ M_\odot$) or secondary shocks in outer layers for simplicity. Assuming blackbody emission, the effective temperature is

$$T_{\rm eff} = \left(\frac{L_{\rm tot}}{4\pi\sigma R_{\rm ph}^2}\right)^{1/4}, \tag{2.18}$$

where $L_{\rm tot} = \int L_v \frac{dM_v}{dv} dv$ sums the luminosity across all layers, and $R_{\rm ph}$ is the photosphere radius, defined where optical depth $\tau_v = 1$. The spectral flux density at frequency ν is then given by,

$$F_\nu(t) = \frac{2\pi h\nu^3}{c^2}\frac{1}{\exp\left(\frac{h\nu}{kT_{\rm eff}(t)}\right) - 1}\frac{R_{\rm ph}^2(t)}{D^2}, \tag{2.19}$$

where D is the distance to the source, and cosmological corrections are omitted for simplicity.

3 Radiative Transfer

15

Radiative Transfer

While an analytical toy model from Sec. 2.3[→p.12] offer valuable insights into the basic physical principles governing kilonovae, they rely on simplifying assumptions that limit their applicability to real events. In reality, modeling kilonovae poses formidable challenges due to the intricate physics of their ejecta. The material expelled during a neutron star merger is neither uniform nor spherically symmetric, often comprising regions with diverse compositions—some rich in lanthanides and actinides, others relatively free of these heavy elements. These compositional variations lead to significant differences in opacity, influencing the radiation. Furthermore, the ejecta expand rapidly, necessitating models that account for time-dependent changes in density, temperature, and chemical makeup. To study the observable signatures of kilonovae—such as spectra, light curves, and polarization—radiative transfer simulations are important. These simulations trace the journey of photons through the ejecta, bridging the gap between theoretical predictions and observed data collected.

At the core of radiative transfer simulations is the radiative transfer equation (RTE), which describes how photons interact with matter as they traverse,

$$\frac{dI_\nu}{ds} = j_\nu - \alpha_\nu I_\nu, \tag{3.1}$$

where I_ν is the specific intensity of radiation at frequency ν, j_ν is the emission coefficient, α_ν is the absorption coefficient, and s is the distance traveled by the photons. Solving the RTE analytically is often impractical, particularly in optically thick media or complex geometries, so numerical methods are employed. One approach is the Monte Carlo method, which simulates the trajectories of many individual photons or photon packets. It tracks their interactions—absorption, scattering, or transmission—with the medium and uses a large sample to build a statistical picture of the radiation field. This method works well for three-dimensional setups and frequency-dependent opacities but requires significant computational resources.

In this work, we primarily use the 3-dimensional Monte Carlo Radiative Transfer (MCRT) code, POSSIS [64] and 1-dimensional models from SEDONA [35].

3.1 POSSIS

POSSIS is a radiative transfer code which leverages the Monte Carlo method as its computational backbone, a probabilistic approach ideally suited to study the radiation transport in kilonova ejecta. In this technique, the photon packets are characterized by frequency, direction, and position, as they traverse through the expanding medium. These packets originate from the thermal energy pool, driven primarily by radioactive decay, undergoing scattering, absorption, or re-emission

based on local physical conditions. By tracking individual photon histories, POSSIS preserves the full complexity of the system, enabling detailed predictions of how emission varies with viewing angles, time, and frequency.

The physical foundation of POSSIS begins with the ejecta model typically a 3-dimensional grid from Numerical Relativity simulations, which describes the structure and evolution of the material expelled during the neutron star merger. This geometry is setup in such that, we have a lanthanide rich component in the equatorial region and lanthanide free component around in the polar region.
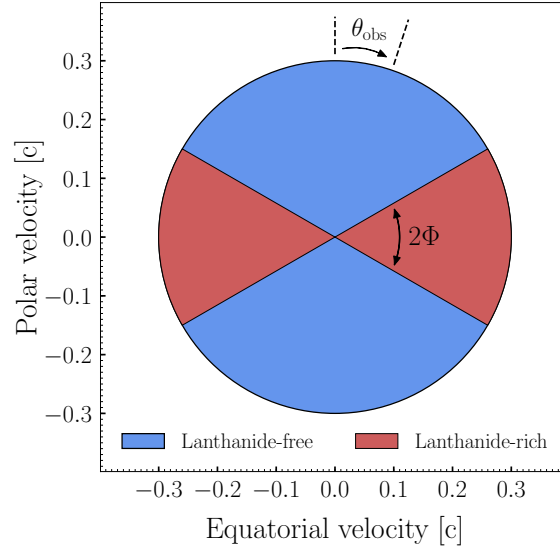
Figure 3.1: Cross-sectional view of the ejecta model used in POSSIS. The high-opacity, lanthanide-rich material is concentrated around the equatorial region (merger plane) with a half-opening angle Φ, while the polar region consists of low-opacity, lanthanide-free ejecta. The synthetic observables (cf. Sec. 3.1.1 →p.17) are computed for various viewing angles Θ_{obs}. Image credit: Ref. [64]

A key assumption is homologous expansion, where the velocity of each ejecta element scales linearly with its radial distance from the explosion's center, expressed as $v \propto r$. This approximation reflects the rapid, free expansion following the merger's dynamical phase. As the ejecta expands, the density scales as,

$$\rho_{ij} = \rho_{i,0}\left(\frac{t_0}{t_j}\right)^3, \tag{3.2}$$

where ρ_{ij} is the density at grid cell i at time t_j, $\rho_{i,0}$ is the initial density, t_0 is the initial time, and t_j is the time step. The factor of 3 arises from the volumetric expansion of the ejecta, directly influencing the optical depth and the timescales over which radiation escapes. As already established in Sec. 2.2 →p.6, the ejecta's composition is crucial, with lanthanides and actinides playing a significant role in shaping the kilonova's emission. POSSIS accounts for this by incorporating several opacity sources, including bound-bound (lanthanide rich: $Y_e \leq 0.25$, lanthanide free: $Y_e > 0.25$), electron scattering, bound-free, and free-free opacities. Bound-bound opacities, κ_{bb}, govern the interaction of radiation with spectral lines. Electron

scattering opacity, $\kappa_{\rm es}$, is critical for polarization calculations, while bound-free $\kappa_{\rm bf}$ and free-free $\kappa_{\rm ff}$ contribute to continuum absorption. Opacities may be specified at each time step or interpolated from a reference time using an appropriate functional form (based on atomic calculations from Ref. [142]), facilitating efficient modeling of time-dependent spectra.

At each simulation time step, a predetermined number of photon packets is generated, each characterized by an initial position, propagation direction, energy, frequency, and polarization state. The frequency of a packet is assigned by sampling the thermal emissivity function,

$$S(\nu) = B(\nu, T)\kappa_{\rm tot}(\nu), \tag{3.3}$$

where $B(\nu, T)$ is the Planck function and $\kappa_{\rm tot}(\nu)$ is the total opacity. The photon packets propagate through the ejecta, interacting with the medium via absorption, re-emission, and scattering processes. These interactions are computed in the comoving frame, with appropriate transformations applied to ensure proper treatment of relativistic effects.

Photon packets travel through the ejecta until they reach the computational boundary, where they are either absorbed, scattered, or allowed to escape. The propagation path of each photon is determined probabilistically based on the mean free path associated with the local opacity. In the case of electron scattering, the photon direction is altered while its frequency remains unchanged. If absorption occurs, the packet is re-emitted with a new frequency determined by the thermal emissivity. This iterative process continues until all photon packets either escape the system or are fully absorbed.

3.1.1 Synthetic Observables

To extract synthetic observables, `POSSIS` employs two complementary techniques: the direct counting technique (DCT) and the event-based technique (EBT). In the DCT approach, escaping photon packets are binned according to their final propagation directions to generate spectra and light curves. The EBT, in contrast, assigns probabilities to virtual packets at each interaction site, weighting them according to their likelihood of reaching the observer. This method significantly reduces Monte Carlo noise and improves the accuracy of polarization predictions.

The synthetic observables generated by `POSSIS` include spectral energy distributions (SEDs), broadband light curves, and polarization spectra. The SEDs provide wavelength-dependent flux predictions at different epochs and viewing angles, revealing the interaction between the ejecta's composition and its radiative properties. Broadband light curves, computed in various photometric filters, enable direct comparisons with observational data from transient surveys. Polarization spectra further constrain ejecta asymmetries by quantifying the anisotropic scattering of photons.

Broadband light curves exhibit significant viewing-angle dependence, reflecting the asymmetric nature of the ejecta. When viewed along the polar axis, the light curves

appear brighter and decay more rapidly, whereas equatorial views lead to fainter, longer-lasting emission due to increased opacity from lanthanide-rich material. This anisotropy is particularly pronounced in kilonovae, where distinct ejecta components contribute differently across various wavelengths. The analysis of broadband light curves allows for the inference of key parameters such as the total ejecta mass, lanthanide fraction, and inclination angle relative to the observer.
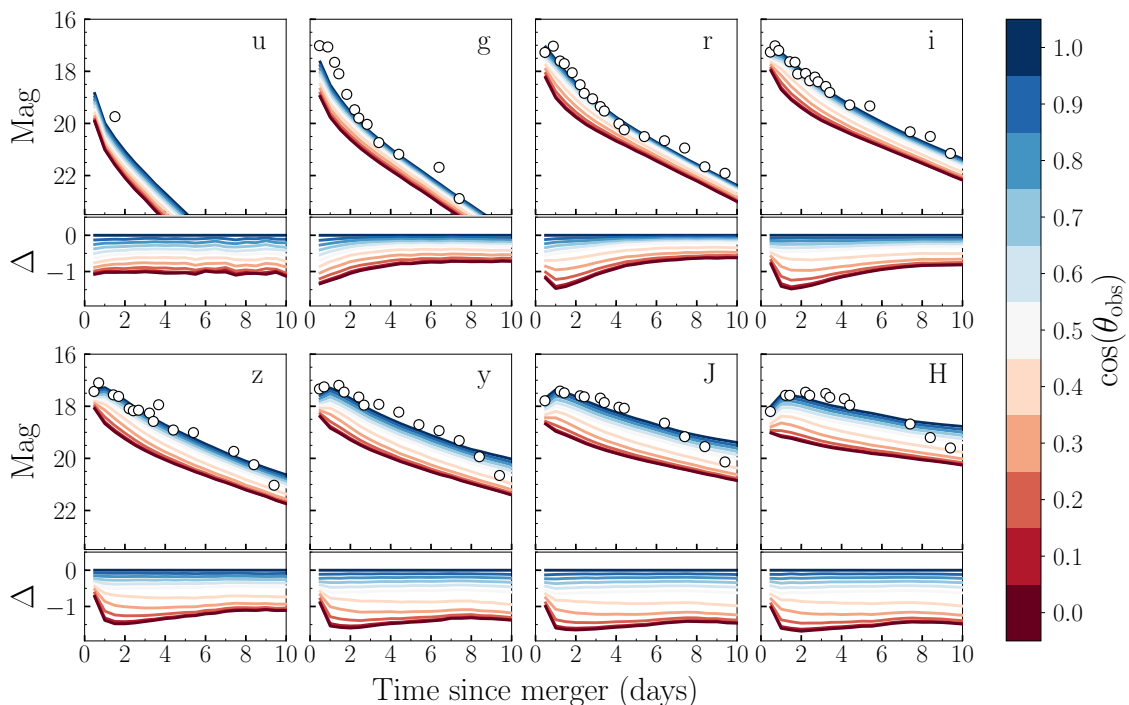
Figure 3.2: Fiducial light curve for a kilonova event generated by `POSSIS`. Color bar shows 11 observing angles ranging from $\cos\Theta_{\rm obs} = 0$ (equatorial) to 1 (polar). The light curves exhibit significant viewing-angle dependence, with polar views showing brighter, longer-lasting emission compared to equatorial views. Each subpanel shows the difference between the light curve observed at that angle and polar angle. Open circles represents the kilonova `AT2017gfo` corrected for Milky Way extinction. Image credit: Ref. [64]

3.2 SEDONA

Although `SEDONA` is a 3D code, in this thesis, we focus on a grid of one-dimensional spherically symmetric models presented in Ref. [35]. This model is parameterized by the ejecta total mass $M_{\rm ej}$, average velocity $v_{\rm ej}$, and lanthanide fraction $X_{\rm lan}$. The bulk of the freely expanding ejecta is determined by the ejecta mass $M_{\rm ej}$. The density profile of the ejecta is described using a broken power-law that transits from the gradually declining interior with $v_{\rm ej}t/r$ to the steeply dropping outer layer with $(v_{\rm ej}t/r)^{10}$. Finally, the lanthanide fraction $X_{\rm lan}$ influences the opacity and color evolution of the kilonova, where larger lanthanide fractions result in increased opacity and longer-duration emissions shifted towards the infrared.

The energy source powering the kilonova emission is the radioactive decay of r-process nuclei synthesized during the merger. The heating rate follows a power-law which is very similar to the on defined in $\boxed{\text{Eq. (2.6)}^{\rightarrow\text{p.11}}}$, $\dot{\varepsilon}_{\text{nuc}} \propto t^{-1.3}$, due to the wide distribution of half-lives of these freshly formed isotopes. Consequently, the radiation escapes once the diffusion timescale becomes comparable to the expansion time, and the time-dependent luminosity is primarily governed by the product $\kappa M/v$, where κ is the opacity. This opacity is highly sensitive to the composition—lanthanide-rich ejecta have significantly higher opacities (up to ~ 10 cm^2 g^{-1}) than lanthanide-poor material (<1 cm^2 g^{-1}), due to the dense forest of line transitions from f-shell electrons in heavy elements.

As a result, low-X_{lan} ($\leq 10^{-4}$) material emits briefly and in the optical (a "blue" kilonova), while high-X_{lan} ($\geq 10^{-2}$) ejecta lead to longer, redder, infrared-dominated emission (a "red" kilonova). In `AT2017gfo`, both components are observed, the early-time optical light is attributed to fast ($\sim 0.3c$), lanthanide-poor ejecta likely from polar shock-driven outflows; the longer infrared tail arises from slower ($\sim 0.1-0.2c$), lanthanide-rich material, possibly originating from disk winds or tidal ejecta.

4 Statistical Methods

Repeated observations of astronomical phenomena are often characterized by complex, noisy data that require sophisticated statistical techniques for their analysis. In this chapter, we introduce the fundamental concepts of probability theory and Bayesian statistics, which form the basis of our approach to parameter estimation and model comparison in multi-messenger astronomy. We also discuss the computational techniques required for practical Bayesian inference in complex astrophysical problems.

4.1 Bayesian Statistics

4.1.1 Probability Theory

Probability theory forms the mathematical backbone of statistical inference. A probability distribution describes how probability mass or density is assigned to possible values of a random variable. For a discrete random variable X, the probability of an event A occurring is given by,

$$P(A) = \sum_i P(A_i),\tag{4.1}$$

where A_i are mutually exclusive outcomes. For a continuous variable θ, the probability density function (PDF) is given by,

$$P(A) = \int_A p(\theta)d\theta.\tag{4.2}$$

One of the fundamental properties of probability theory is the law of total probability, which states that for any partition B_i of the sample space, the probability of an event A is given by,

$$P(A) = \sum_i P(A|B_i)P(B_i).\tag{4.3}$$

Another key principle is conditional probability, which quantifies the probability of an event A given that another event B has occurred, given by

$$P(A|B) = \frac{P(A \cap B)}{P(B)}.\tag{4.4}$$

In the context of astrophysical inference, we are often interested in estimating the parameters θ of a model, given some observed data D. The interpretation of probability in such problems can be broadly categorized into two perspectives:

- **Frequentist Interpretation:** Probability is defined as the long-run relative frequency of an event in repeated trials. This approach underlies classical statistical methods, including confidence intervals and hypothesis testing, but does not incorporate prior knowledge in parameter estimation.

- **Bayesian interpretation:** Probability represents a degree of belief in an event, updated as new evidence is obtained. This approach allows for the incorporation of prior information through Bayes' theorem, making it particularly suited for problems where data are limited or where prior knowledge is available.

In astrophysical applications, particularly in transient event analysis, the frequentist approach is often inadequate because no two astronomical events are strictly identical. Consequently, Bayesian inference, which systematically updates prior knowledge with new observations, provides a more robust framework for parameter estimation in such scenarios.

4.1.2 Bayes' Theorem

Bayes' theorem is derived directly from the definition of conditional probability. For two events A and B, can be rewritten as

$$P(A|B)P(B) = P(A \cap B) = P(B|A)P(A), \tag{4.5}$$

which can be rearranged to yield Bayes' theorem as follows,

$$P(A|B) = \frac{P(B|A)P(A)}{P(B)}, \tag{4.6}$$

where each term carries a specific statistical interpretation. The prior probability, $P(A)$, quantifies the initial probability of event A based on pre-existing information or assumptions, established prior to observing the specific event. The likelihood, $P(B|A)$ quantifies the probability of observing data B given that the hypothesis A is true. The posterior probability, $P(B|A)$ is the updated probability of A after accounting for the data B. The evidence, or marginal likelihood, $P(B)$, acts as a normalization factor, ensuring that the posterior is a valid probability distribution. For discrete hypothesis, it is calculated as

$$P(B) = \sum_i P(B|A_i)P(A_i), \tag{4.7}$$

summing over all possible states A_i and for continuous hypothesis, it is given by

$$P(B) = \int P(B|\theta)P(\theta)d\theta, \tag{4.8}$$

where θ denotes the parameter vector and the integral spans the prior distribution.

This is the fundamental form of Bayes' theorem, which allows the inversion of conditional probabilities based on prior knowledge. The real power of Bayes' theorem

lies in its systematic way to update our beliefs about a parameter as more data become available. This makes it particularly powerful in astrophysical applications, where observations are often sequentially obtained over time, such as in the case of transient events.

4.1.3 Parameter Estimation

To perform parameter estimation in a Bayesian framework, we seek to infer the posterior distribution of the model parameters $\vec{\theta}$ given the observed data d under the assumption of some hypothesis $\mathcal{H}$. This is achieved by combining the likelihood function, which quantifies the probability of observing the data given the model parameters, with the prior distribution, which encodes our prior knowledge about the parameters. To this end, Bayes' theorem takes the form

$$P(\vec{\theta}|d,\mathcal{H}) = \frac{P(d|\vec{\theta},\mathcal{H})P(\vec{\theta}|\mathcal{H})}{P(d|\mathcal{H})},\tag{4.9}$$

or more familiarly as

$$P(\vec{\theta}|d,\mathcal{H}) = \frac{\mathcal{L}(\vec{\theta})\pi(\vec{\theta}|\mathcal{H})}{\mathcal{Z}},\tag{4.10}$$

and the evidence is given by

$$\mathcal{Z} = \int_{\Omega_{\vec{\theta}}} \mathcal{L}(\vec{\theta})\pi(\vec{\theta}|\mathcal{H})d\vec{\theta},\tag{4.11}$$

where integration is performed over the entire parameter space $\Omega_{\vec{\theta}}$.

In this context, the hypothesis $\mathcal{H}$ represents the underlying model or theoretical framework that we assume to be true when performing our analysis. It encapsulates our fundamental assumptions about the system under study and defines the space of possible parameter values $\vec{\theta}$ that can describe the data. For instance, in astronomical observations, $\mathcal{H}$ might represent the hypothesis that Newton's law of gravitation correctly describes the motion of celestial bodies, or alternatively, that Einstein's theory of general relativity is the correct framework. The explicit conditioning on $\mathcal{H}$ throughout the equations reminds us that all our inferences about parameters $\vec{\theta}$ are conditional on the validity of the underlying model. The posterior distribution $P(\vec{\theta}|d,\mathcal{H})$ provides the probability of different parameter values given both the observed data and our assumed model. Similarly, the prior $P(\vec{\theta}|\mathcal{H})$ encodes our beliefs about parameter values within the context of hypothesis $\mathcal{H}$ before observing any data. The evidence, cf. , also known as the marginal likelihood, quantifies how well the hypothesis $\mathcal{H}$ explains the observed data, averaged over all possible parameter values weighted by their prior probabilities.

4.1.4 Hypothesis Testing

In Bayesian hypothesis testing, we extend the framework of parameter estimation to evaluate the relative plausibility of competing hypotheses given observed data.

Unlike parameter estimation, where we infer the distribution of parameters within a single model, hypothesis testing involves comparing multiple models or hypotheses to determine which one provides a better explanation for the observed phenomena.

Consider two competing hypotheses, $\mathcal{H}_1$ and $\mathcal{H}_2$, each representing different models or theoretical frameworks. Eq. (4.9)$^{\rightarrow \text{p.22}}$ can be transformed to represent the posterior probability of hypothesis $\mathcal{H}_i$ given the data d as follows

$$P(\mathcal{H}_i|d) = \frac{P(d|\mathcal{H}_i)P(\mathcal{H}_i)}{P(d)}, \tag{4.12}$$

where $P(d|\mathcal{H}_i)$ is the evidence for hypothesis $\mathcal{H}_i$, $P(\mathcal{H}_i)$ is the prior probability assigned to hypothesis $\mathcal{H}_i$ before observing the data, and $P(d)$ is the total probability of observing the data across all possible hypotheses.

The ratio of posterior probabilities for two competing hypotheses, known as the posterior odds or odds ratio, provides a direct measure of their relative plausibility

$$\frac{P(\mathcal{H}_1|d)}{P(\mathcal{H}_2|d)} = \frac{P(d|\mathcal{H}_1)}{P(d|\mathcal{H}_2)} \cdot \frac{P(\mathcal{H}_1)}{P(\mathcal{H}_2)}. \tag{4.13}$$

The first term on the right-hand side is the Bayes factor, denoted as $\mathcal{B}_2^1$, which quantifies the relative evidence provided by the data in favor of $\mathcal{H}_1$ over $\mathcal{H}_2$

$$\mathcal{B}_2^1 = \frac{P(d|\mathcal{H}_1)}{P(d|\mathcal{H}_2)} = \frac{\mathcal{Z}_1}{\mathcal{Z}_2}, \tag{4.14}$$

where $\mathcal{Z}_i$ represents the evidence for hypothesis $\mathcal{H}_i$ as defined in Eq. (4.11)$^{\rightarrow \text{p.22}}$. The second term in Eq. (4.13)$^{\rightarrow \text{p.23}}$ is the prior odds, which represents the relative plausibility of the hypotheses before observing the data,

$$\Pi_2^1 = \frac{P(\mathcal{H}_1)}{P(\mathcal{H}_2)}. \tag{4.15}$$

With Eq. (4.14)$^{\rightarrow \text{p.23}}$ and Eq. (4.15)$^{\rightarrow \text{p.23}}$, the odds ratio can be expressed as,

$$\mathcal{O}_2^1 = \mathcal{B}_2^1 \Pi_2^1, \tag{4.16}$$

In practical applications, the prior odds are often set to unity under the assumption that both hypotheses are equally likely, hence the posterior odds are same as the Bayes factor.

The Bayes factor $\mathcal{B}_2^1$ provides an objective measure of the strength of evidence in the data, independent of prior beliefs about the hypotheses.

When the Bayes factor $\mathcal{B}_2^1 > 1$, the data provides evidence in favor of $\mathcal{H}_1$ over $\mathcal{H}_2$, with larger values indicating stronger evidence. Conversely, when $\mathcal{B}_2^1 < 1$, the

data supports $\mathcal{H}_2$ over $\mathcal{H}_1$. The magnitude of the Bayes factor can be interpreted according to established scales, with values above 10 typically considered strong evidence and values above 100 decisive evidence.

For nested models, where hypothesis $\mathcal{H}_1$ represents a more general model that includes $\mathcal{H}_2$ as a special case, the Bayes factor automatically implements Occam's razor by penalizing unnecessary complexity. If the additional parameters in $\mathcal{H}_1$ do not significantly improve the fit to the data, the evidence will favor the simpler model $\mathcal{H}_2$, as expressed by

$$\mathcal{B}_2^1 = \frac{\int_{\Omega_{\vec{\theta}_1}} P(d|\vec{\theta}_1, \mathcal{H}_1)\pi(\vec{\theta}_1|\mathcal{H}_1)d\vec{\theta}_1}{\int_{\Omega_{\vec{\theta}_2}} P(d|\vec{\theta}_2, \mathcal{H}_2)\pi(\vec{\theta}_2|\mathcal{H}_2)d\vec{\theta}_2}. \tag{4.17}$$

When dealing with multiple hypotheses $\{\mathcal{H}_1, \mathcal{H}_2, \ldots, \mathcal{H}_n\}$, we can compute the posterior probability of each hypothesis as

$$P(\mathcal{H}_i|d) = \frac{P(d|\mathcal{H}_i)}{\sum_{j=1}^n P(d|\mathcal{H}_j)}. \tag{4.18}$$

This formulation allows for a coherent assessment of the relative plausibility of all competing hypotheses simultaneously, rather than through pairwise comparisons alone.

4.2   Computational Methods

The Bayesian approach to parameter estimation and hypothesis testing, while theoretically elegant, presents significant computational challenges in practical applications. In particular, evaluating the posterior distribution, cf. $\boxed{\text{Eq. (4.10)}^{\rightarrow\,\text{P.22}}}$, requires computing the multidimensional integral $\boxed{\text{Eq. (4.11)}^{\rightarrow\,\text{P.22}}}$ for the evidence $\mathcal{Z}$. For all but the simplest problems with analytic solutions, this integral is intractable using traditional numerical integration methods, especially as the dimensionality of the parameter space increases—a phenomenon known as the "curse of dimensionality".

In astrophysical applications, we typically encounter complex likelihood functions that may be multimodal, exhibit strong parameter degeneracies, or contain sharp peaks in high-dimensional spaces. For instance, in multi-messenger astronomy, the joint analysis of gravitational wave and electromagnetic signals involves parameter spaces with dimensions often exceeding 10-15 parameters. Direct numerical integration in such spaces would require an exponentially increasing number of function evaluations that quickly becomes computationally expensive, more often than not, prohibitive.

Consequently, stochastic sampling methods have emerged as the preferred approach for Bayesian computation for astrophysical problems. These methods approximate

the posterior distribution by drawing samples from it, without requiring the explicit calculation of the normalizing evidence. The generated samples can then be used to estimate parameter values, construct credible intervals, and compute quantities of interest. Additionally, some sampling methods provide estimates of the evidence $\mathcal{Z}$, enabling rigorous model comparison through Bayes factors as described in Eq. $(4.14)^{\rightarrow \mathrm{p.23}}$.

In the following texts, we discuss two principal sampling techniques that have proven particularly effective for astronomical applications: Markov Chain Monte Carlo (MCMC) methods, which excel at efficiently exploring posterior distributions for parameter estimation, and nested sampling, which was specifically designed to compute the evidence while simultaneously providing posterior samples.

4.2.1 Markov Chain Monte Carlo

MCMC methods constitute a class of algorithms designed to draw samples from a probability distribution by constructing a Markov chain whose equilibrium distribution converges to the target posterior distribution. The fundamental principle underlying MCMC is that, after an initial "burn-in" period, the states of the chain represent correlated samples from the posterior distribution, which can be used to estimate any quantity of interest.

The Metropolis-Hastings algorithm [144,145], a canonical MCMC method, generates samples from the posterior distribution, $P(\vec{\theta}|d, \mathcal{H})$, through the following procedure:

Algorithm 1: Metropolis-Hastings Algorithm

---

1 Initialize the chain at position $\vec{\theta}_0$ in parameter space.

2 for *each iteration t* **do**

3 $\quad$ Propose a new position $\vec{\theta}'$ according to a proposal distribution $q(\vec{\theta}'|\vec{\theta}_t)$
$\quad$ Compute the acceptance ratio:

$$\alpha = \min\left(1, \frac{P(\vec{\theta}'|d, \mathcal{H})}{P(\vec{\theta}_t|d, \mathcal{H})} \frac{q(\vec{\theta}_t|\vec{\theta}')}{q(\vec{\theta}'|\vec{\theta}_t)}\right) \tag{4.19}$$

$\quad$ Draw $u \sim \mathcal{U}(0,1)$ **if** $u < \alpha$ **then**

4 $\quad \quad$ Set $\vec{\theta}_{t+1} = \vec{\theta}'$

5 $\quad$ **else**

6 $\quad \quad$ Set $\vec{\theta}_{t+1} = \vec{\theta}_t$

7 $\quad$ **end if**

8 end for

For symmetric proposal distributions, where $q(\vec{\theta}'|\vec{\theta}_t) = q(\vec{\theta}_t|\vec{\theta}')$, this simplifies to the

Metropolis algorithm with acceptance ratio,

$$\alpha = \min\left(1, \frac{P(\vec{\theta}'|d, \mathcal{H})}{P(\vec{\theta}_t|d, \mathcal{H})}\right). \tag{4.20}$$

A crucial aspect of the Metropolis-Hastings algorithm is that it only requires evaluating the posterior up to a normalizing constant, as the ratio in $\boxed{\text{Eq. (4.20)}^{\,\rightarrow\,\text{p.26}}}$ cancels out the evidence term $\mathcal{Z}$

$$\frac{P(\vec{\theta}'|d, \mathcal{H})}{P(\vec{\theta}_t|d, \mathcal{H})} = \frac{\mathcal{L}(\vec{\theta}')\pi(\vec{\theta}'|\mathcal{H})}{\mathcal{L}(\vec{\theta}_t)\pi(\vec{\theta}_t|\mathcal{H})}. \tag{4.21}$$

While conceptually straightforward, the practical performance of MCMC methods depends critically on the choice of proposal distribution. Proposals that are too conservative (small step sizes) result in high acceptance rates but slow exploration of the parameter space, whereas proposals that are too ambitious (large step sizes) lead to many rejections and inefficient sampling. This challenge is especially pronounced in high-dimensional spaces with strong parameter correlations, which are common in astrophysical applications.

A critical aspect of MCMC implementation is the handling of burn-in samples. Since the Markov chain typically starts from an arbitrary position in parameter space, the initial samples do not accurately represent the target posterior distribution. These early iterations, known as the burn-in phase, must be discarded to ensure that only samples from the converged stationary distribution are used for inference. Formally, if B represents the number of burn-in iterations, the samples used for analysis are $\vec{\theta}_{B+1}, \vec{\theta}_{B+2}, \dots, \vec{\theta}_N$.

The primary output of MCMC methods, after discarding burn-in samples, is a set of samples that approximates the posterior distribution. From these samples, we can estimate moments, compute credible intervals, and construct marginal posterior distributions. The posterior mean for each parameter θ_i is estimated as,

$$\bar{\theta}_i = \frac{1}{N}\sum_{j=1}^{N}\theta_{i,j}. \tag{4.22}$$

Similarly, the posterior covariance between parameters θ_i and θ_j is estimated as,

$$\text{Cov}(\theta_i, \theta_j) = \frac{1}{N-1}\sum_{k=1}^{N}(\theta_{i,k} - \bar{\theta}_i)(\theta_{j,k} - \bar{\theta}_j). \tag{4.23}$$

4.2.2 Nested Sampling

While MCMC methods are well-suited for exploring the posterior distribution for parameter estimation, they are less efficient at computing the evidence $\mathcal{Z}$, which is
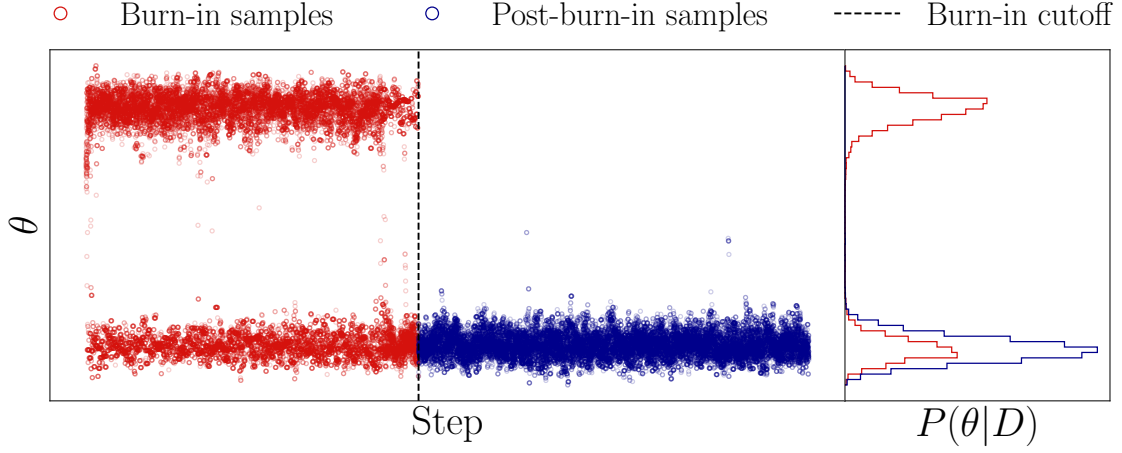
Figure 4.1: Trace plot showing the MCMC burn-in and post burn-in samples. The initial burn-in phase (red) exhibits erratic behavior before the chain converges to a steady state. The burn-in cutoff (black dashed line) marks the transition to the post burn-in phase (blue), where the samples are representative of the posterior distribution $P(\theta|D)$.

essential for model comparison. nested sampling, introduced by Skilling [146], is a computational method specifically designed to efficiently calculate the evidence $\mathcal{Z}$ while simultaneously generating samples from the posterior distribution. Unlike MCMC methods, which focus primarily on exploring the posterior, nested sampling deliberately targets the evidence integral in Equation (4.11). The key idea of nested sampling is to transform the multidimensional evidence integral over parameter space, $\Omega_{\vec{\theta}}$, into a one-dimensional integral over the prior volume. We define the prior volume $X(\lambda)$ as the fraction of prior volume enclosed by the iso-likelihood contour $\mathcal{L}(\vec{\theta}) = \lambda$,

$$X(\lambda) = \int_{\{\vec{\theta}:\mathcal{L}(\vec{\theta})>\lambda\}} \pi(\vec{\theta}|\mathcal{H})d\vec{\theta}. \qquad (4.24)$$

As λ increases from 0 to the maximum likelihood value, $X(\lambda)$ decreases monotonically from 1 to 0. This allows us to rewrite the evidence integral as a one-dimensional integral over the prior volume,

$$\mathcal{Z} = \int_0^1 \mathcal{L}(X)dX, \qquad (4.25)$$

where $\mathcal{L}(X)$ is the inverse function of $X(\lambda)$, representing the likelihood value that corresponds to prior volume X.

Stopping Criterion

Since nested sampling proceeds by iteratively removing the point with the lowest likelihood and replacing it with a new sample, the algorithm must determine when to terminate. A common stopping criterion is based on the remaining prior volume contributing negligibly to the evidence estimate. Specifically, the algorithm terminates when the change in evidence between successive iterations falls below a

---

Algorithm 2: Nested Sampling Algorithm

---

1 Initialize N *live points* $\{\vec{\theta}_i\}_{i=1}^N$ sampled from the prior $\pi(\vec{\theta})$.

2 $i \leftarrow 0$

3 **while** *termination criterion not met* **do**

4 $\quad$ Compute the likelihoods $\mathcal{L}_i = \mathcal{L}(\vec{\theta}_i)$ for all *live points*

5 $\quad$ Identify the point $\vec{\theta}_{\min}$ with the lowest likelihood $\mathcal{L}_i = \mathcal{L}(\vec{\theta}_{\min})$ among the *live points*

6 $\quad$ Remove $\vec{\theta}_{\min}$ from the set of *live points* and save it as a *dead point*

7 $\quad$ Generate a new *live point* $\vec{\theta}_{\text{new}}$ from the prior distribution, subject to the constraint $\mathcal{L}(\vec{\theta}_{\text{new}}) > \mathcal{L}_i$

8 $\quad$ Compute termination criterion $\Delta\hat{Z}_i$

9 $\quad$ $i \leftarrow i + 1$

10 **end while**

---

specified threshold. At a given iteration i we compute an estimate $\hat{Z}_i$ of the accumulated evidence and compare it with the remaining evidence $\Delta\hat{Z}_i$. However, this remaining evidence is unknown, but one can put strict upper bounds on it by considering the maximum likelihood ever encountered in the entire parameter space and the remaining prior volume X_i. Under this assumption, the remaining evidence can be bounded as,

$$\Delta\hat{Z}_i \leq \mathcal{L}_{\max} X_i. \tag{4.26}$$

With this bound, the stopping criterion can be expressed as the log ratio of evidences,

$$\Delta\hat{Z}_i \equiv \ln\left(\frac{\hat{Z}_i + \mathcal{L}_{\max} X_i}{\hat{Z}_i}\right) < \varepsilon. \tag{4.27}$$
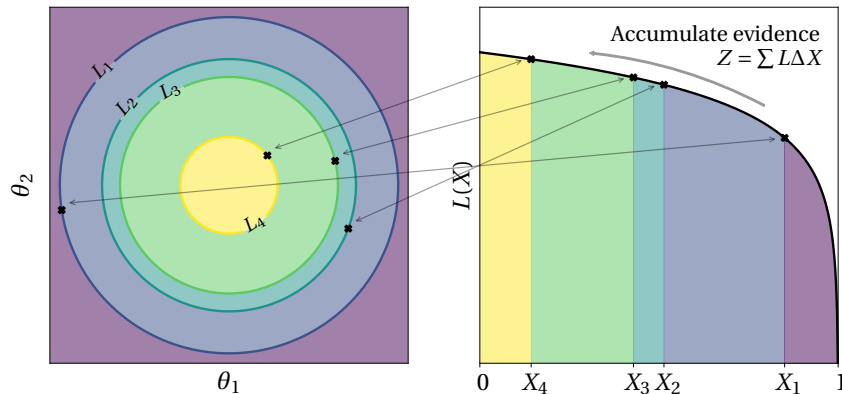
Figure 4.2: Illustration of the nested sampling algorithm in a two-dimensional parameter space $\theta \in \{\theta_1, \theta_2\}$. Nested sampling progressively explores regions of higher likelihood, moving from points X_1 to X_4. The algorithm accumulates evidence by summing the product of likelihood values and change in prior volume, $Z = \sum \mathcal{L}\Delta X$, integrating over the posterior distribution. Image credit: [147].

Evidence and Posterior

Once the nested sampling algorithm terminates, we can estimate the evidence $\mathcal{Z}$ by integrating the likelihood values of the removed dead points weighted by the change in prior volume,

$$\mathcal{Z} = \int_0^1 \hat{\mathcal{L}}(X)dX. \tag{4.28}$$

Since, the entire discussion is based on how unfeasible it is to compute the integral, we can approximate the integral using the trapezoidal sum as follows,

$$\begin{aligned}
\mathcal{Z} &\approx \frac{1}{2}\sum_{i=1}^{N}(\mathcal{L}_{i-1} + \mathcal{L}_i)(X_{i-1} - X_i) \\
&\equiv \sum_{i=1}^{N} w_i.
\end{aligned} \tag{4.29}$$

The posterior distribution can be estimated from the *dead points* by weighing each sample by the importance weight p_i,

$$p_i = \frac{w_i}{\sum_{i=1}^{N} w_i}. \tag{4.30}$$

5
Nuclear-Physics and Multi-Messenger Astrophysics

Building upon the foundations established in the preceding chapters, we have developed a comprehensive understanding of the physical mechanisms governing BNS mergers, the EM signatures they produce, and the statistical frameworks required to extract meaningful constraints from observational data.

All of these components converge in the `NMMA` framework, which serves as an advanced Bayesian inference tool for the simultaneous analysis of gravitational wave signals, kilonova light curves, and other multi-messenger data. `NMMA` synthesizes information from different observational channels while incorporating nuclear-physics constraints and gravitational wave data to provide a self-consistent framework for understanding BNS mergers.

5.1 Overview

The `NMMA` framework is designed to address several fundamental problems in neutron star astrophysics. The equation of state (EOS) of neutron star matter remains one of the central unresolved questions, as it governs the internal structure and dynamics of these compact objects. Constraints on the EOS can be obtained from gravitational-wave observations of the tidal deformations experienced by neutron stars during inspiral, from X-ray and radio measurements of pulsars, and from nuclear theory calculations. Similarly, the properties of BNS and neutron star-black hole (NSBH) mergers, including their ejecta masses, velocities, and composition can be constrained by analyzing the EM signals emitted following the merger. Additionally, multi-messenger observations of neutron star mergers provide an independent means of measuring the Hubble constant, thus offering a novel probe of cosmology. The `NMMA` framework integrates all of these constraints into a unified inference pipeline, ensuring that information from different messengers is combined in a statistically rigorous manner.

At its core, `NMMA` is based on Bayesian inference (through `BILBY` [148,149]), allowing for a consistent incorporation of prior knowledge, observational data and physical measurements to estimate posterior probability distributions of physical parameters. The framework primarily uses nested sampling to efficiently explore the high-dimensional parameter space of BNS mergers. The likelihood function within `NMMA` is constructed as a product of the likelihoods associated with different observational channels: gravitational waves, kilonova light curves, and, when available, GRB afterglows. This multi-component likelihood function enables `NMMA` to leverage all available information to obtain more precise constraints on neutron star properties and merger physics.

5.1.1   Nuclear Physics Constraints

`NMMA` incorporates nuclear physics constraints into the inference process to ensure that the derived properties of neutron stars and their mergers are physically consistent with our understanding of dense nuclear matter. The EOS of neutron star matter, is a critical component that influences both gravitational wave signals through tidal deformabilities and kilonova emission through the properties of merger ejecta. The framework employs a two-region approach to model the EOS. At low densities (up to approximately $2n_{\text{sat}}$, where $n_{\text{sat}} = 0.16$ fm^{-3} is the nuclear saturation density), `NMMA` utilizes Quantum Monte Carlo calculations based on Chiral Effective Field Theory (EFT), providing a systematic description of nuclear interactions with quantifiable uncertainties. For the higher densities reached in neutron star cores, where Chiral EFT becomes unreliable, `NMMA` implements a model independent speed-of-sound extension scheme bounded only by causality ($c_s \leq c$) and mechanical stability ($c_s \geq 0$).[1]

This methodology allows `NMMA` to generate EOS realizations that are consistent with known nuclear physics while adequately exploring uncertainties at high densities. For each sampled EOS, the framework solves the TOV equations to determine neutron star properties such as the mass-radius relationship and tidal deformabilities, which directly influence observable gravitational wave and EM signatures.

5.1.2   Gravitational Waves

Gravitational-wave data play a fundamental role in `NMMA`'s inference pipeline. The inspiral phase of a BNS merger encodes crucial information about the component masses and tidal deformabilities, which in turn provide constraints on the EOS. To extract this information, `NMMA` utilizes various waveform models from `LALSuite` [152]. The likelihood function for gravitational-wave data is computed by cross-correlating the observed detector strain with theoretical waveform templates, weighted by the detector's noise power spectral density. The likelihood $\mathcal{L}_{\text{GW}}$ for gravitational wave data, given a set of parameters θ, is defined as,

$$\mathcal{L}_{\text{GW}} \propto \exp\left(-\frac{1}{2}\langle d - h(\theta) \mid d - h(\theta)\rangle\right), \tag{5.1}$$

where d is the detector strain data, $h(\theta)$ is the GW signal generated from parameters θ, and $\langle \cdot \mid \cdot \rangle$ is the inner product defined as,

$$\langle a \mid b \rangle = 4\,\text{Re} \int_{f_{\text{min}}}^{f_{\text{max}}} \frac{\tilde{a}(f)\tilde{b}^*(f)}{S_n(f)}\,\mathrm{d}f, \tag{5.2}$$

where $\tilde{a}(f)$ and $\tilde{b}(f)$ are the Fourier transforms of $a(t)$ and $b(t)$, respectively, $S_n(f)$ is the one-sided noise power spectral density of the noise, and $*$ is the complex

---

[1]Refer to Ch. 6.2.1 $^{\rightarrow\,\text{p.76}}$ and Ch. 9.2.1 $^{\rightarrow\,\text{p.122}}$ of Ref. [150] and Sec. Methods $^{\rightarrow\,\text{p.6}}$ of Ref. [151] for a detailed discussion.

conjugate. The integration limits $f_{\min}$ and $f_{\max}$ are chosen to match the frequency range of the signal.

5.1.3   Kilonovae and Gamma-Ray Bursts

Beyond gravitational waves, `NMMA` incorporates EM data from kilonovae and GRB afterglows to further constrain the properties of neutron star mergers. To model kilonovae, `NMMA` primarily employs `POSSIS`. Additionally, `NMMA` models the GRB afterglows using `afterglowpy` [153,154], a semi-analytic code that simulates the synchrotron emission from relativistic jets produced in neutron star mergers. The likelihood $\mathcal{L}_{\mathrm{EM}}$ for kilonova and GRB can be combined as a single EM likelihood, given a set of parameters θ as

$$\mathcal{L}_{\mathrm{EM}} \propto \exp\left(-\frac{1}{2}\sum_{ij} \frac{\left(m_i^j - m_i^{j,\,\mathrm{est}}\left(\vec{\theta}\right)\right)^2}{\left(\sigma_i^j\right)^2 + \left(\sigma_{\mathrm{sys}}\right)^2}\right), \tag{5.3}$$

where m_i^j is the AB magnitude in filter j at time i with the corresponding measurement error $\sigma_i^j \equiv \sigma^j(t_i)$, $m_i^{j,\,\mathrm{est}}\left(\vec{\theta}\right)$ is the estimated AB magnitude for the source parameters $\vec{\theta}$ (e.g., ejecta masses, velocities) from the model and σ_{sys} is the additional uncertainty to account for systematic errors in the kilonova and afterglow modelling. Computing likelihood in this form is equivalent to including an additional shift to the light curve by Δm, and marginalizing it with a normal distribution with a mean of 0 and variance σ_{sys}.

Using $\boxed{\text{Eq. (5.1)}^{\to\,\text{P.31}}}$ and $\boxed{\text{Eq. (5.3)}^{\to\,\text{P.32}}}$, `NMMA` combines GW and EM to obtain a joint likelihood function,

$$\mathcal{L} = \mathcal{L}_{\mathrm{GW}} \times \mathcal{L}_{\mathrm{EM}}, \tag{5.4}$$

in order to capture the full multi-messenger picture.

5.1.4   Measurements from Isolated Neutron Stars

While the primary focus of `NMMA` is on BNS and NSBH mergers, the framework also incorporates information from isolated neutron stars to further constrain the EOS and priors on neutron star properties. This information includes measurements of neutron star masses and radii from NICER X-ray observations, as well as radio pulsar timing data.[2]

5.2   Surrogate Modelling

Radiative transfer simulations, such as those performed by `POSSIS` and `SEDONA` (hereafter referred to interchangeably as Bu2019lm and Ka2017, respectively, in order

---

[2]Refer to $\boxed{\text{Ch. 6.2.3}^{\to\,\text{P.77}}}$ and $\boxed{\text{Ch. 8}^{\to\,\text{P.109}}}$ of Ref. [150], $\boxed{\text{Sec. Methods}^{\to\,\text{P.6}}}$ of Ref. [151], and Ref. [155] for a detailed discussion.

to be coherent with their names within the `NMMA` community), are computationally expensive, making them impractical to run repeatedly for any arbitrary set of parameters during the Bayesian inference sampling. To address this challenge, `NMMA` employ surrogate models [156] that efficiently interpolates between pre-computed simulation grids in order to reduce the memory footprint and overall computational cost of the inference process. To this end, `NMMA` employs two step approach, first reducing the dimensionality of the data using singular value decomposition (SVD), and then training a surrogate model either using Gaussian Process Regression (GPR) or Neural Network (NN) to interpolate between the reduced data points.

5.2.1   Dimensionality Reduction

While one can directly train a machine learning model on the observables, it is much efficient to first perform some kind of dimensionality reduction in order to get a more compact representation of the data. This is achieved using SVD. For a given set of light curves $\mathbb{L}^j$, generated from a set of parameters θ^j, the full light curve matrix is represented as $\mathbb{L}_i^j \equiv [\mathbb{L}_i(\theta^j)]$, where i indexes the time steps of the light curve. The singular value decomposition of $\mathbb{L}_i^j$ is performed first by normalizing the light curves using MinMax Normalisation and then decomposing the matrix as

$$\mathbb{L} = V\Sigma U^\top, \tag{5.5}$$

where U are the left singular vectors, Σ is the diagonal matrix of singular values, and V are the right singular vectors. With these new basis vectors, the original light curve $\mathbb{L}$ can be projected onto the left singular vectors

$$s_k(\theta^j) = V_{ki}^\top \mathbb{L}_i(\theta^j), \tag{5.6}$$

where $s_k(\theta^j)$ are the weights of the principal components of the input light curve matrix $\mathbb{L}_i^j$. In general, this allows for a more compact representation of the light curves, such that, in `NMMA` only first 10 basis vectors are enough to capture the majority of the information in the light curves.

5.2.2   Interpolation Methods

Once the dimensionality of the data has been reduced, the next step is to train a surrogate model that can interpolate between the pre-computed simulation grids. However, in cases such as, the requested time interval is larger than the original data, a simpler linear interpolation is used.

5.2.2.1   Gaussian Process Regression

GPR provides a non-parametric method for estimating smooth functions while incorporating uncertainty quantification. A Gaussian process is defined by a mean function $m(\theta)$ and a covariance function $k(\theta, \theta')$, such that the function values at

any set of points θ are jointly Gaussian distributed such that the coefficients s_k can be represented as

$$s_k(\theta) \sim \mathcal{GP}(m(\theta), k(\theta, \theta')). \tag{5.7}$$

Consequently, the coefficients s_k are then interpolated with a rational-quadratic kernel [157]

$$k(\vec{\theta}, \vec{\theta}') = \left(1 + \frac{|\vec{\theta} - \vec{\theta}'|^2}{2\alpha l^2}\right)^{-\alpha}, \tag{5.8}$$

where $\vec{\theta}$ and $\vec{\theta}'$ are vectors of input parameters and hyperparameters α and l are chosen by maximizing the evidence for the data under a zero-mean Gaussian process. Post interpolation, the full light curve can be reconstructed by projected the interpolated coefficients back onto the original basis vectors

$$\mathbb{L}_i(\theta^j) = V_{ik}s_k(\theta^j). \tag{5.9}$$

NMMA uses `scikit-learn` [158] to implement the GPR interpolation.

5.2.2.2   Neural Networks

Following Ref. [159], NMMA has implemented a NN based interpolation method to reduce memory consumption and accelerate inference compared to the GPR implementation. The primary advantage of this approach is its ability to efficiently handle high-dimensional kilonova models as opposed to GPR, which tends to breakdown with more than 4 model parameters.[3]

Similar to GPR, the NN is trained on a reduced set of data points and then used to interpolate between them. The neural network follows a feed-forward architecture implemented using `TensorFlow` [160] with Adam optimizer [161], a mean squared error loss function and Rectified linear unit (ReLU) [162] activation function. Once trained, the NN can rapidly generate interpolated values across the parameter space, significantly reducing the computational cost associated with traditional interpolation methods. Similar to the GPR approach, the full light curve can be reconstructed by performing inverse transformations on the interpolated coefficients.

The specific architecture, hyperparameter choices, and further implementation details of the neural networks used in this work are discussed below.

POSSIS

The NN surrogate model is trained on 1596 parameter combinations and their corresponding light curves generated from the POSSIS simulation. The NN architecture consists of three fully connected hidden layers with 128, 256, and 128 neurons, respectively. The input layer has neurons corresponding the total number model parameters (Φ, ι, $\log_{10} M_{\mathrm{ej}}^{\mathrm{wind}}$ and $\log_{10} M_{\mathrm{ej}}^{\mathrm{dyn}}$, cf. Sec. 3.1 $^{\rightarrow\, \mathrm{p.15}}$). The output layer

---

[3]Refer Ref. [159] for a detailed discussion on NN accelerated kilonova surrogate modeling.

consists of neurons corresponding to the number of principal components, which is set to 10 in our case. The model is trained for 100 epochs with a batch size of 128, using a learning rate of 10^{-3}. To ensure numerical stability and consistency in the output range, output is rescaled using a MinMax scaler, which normalizes them to a fixed range before applying the inverse transformation to reconstruct the light curves. Additionally, 20% of the dataset is set aside for validation to monitor the model's generalization performance and prevent overfitting.

SEDONA

The total number of publicly available[4] light curves for `SEDONA` is relatively small, comprising only 329 parameter combinations. Despite the limited dataset, the pre-training steps remain the same as those used for `POSSIS`. However, due to the reduced data volume, a different neural network architecture is adopted.

Here we used a single hidden layer of 2048 neurons, with input a layer of three neurons corresponding to the model parameters ($\log_{10} v_{\mathrm{ej}}$, $\log_{10} M_{\mathrm{ej}}$, and $\log_{10} X_{\mathrm{lan}}$, cf. Sec. 3.2 $^{\rightarrow\,\mathrm{p.18}}$). As in the case of `POSSIS`, the output layer consists of 10 neurons, corresponding to the number of principal components used to reduce the dimensionality of the light curves. To improve generalization and mitigate overfitting, a dropout layer with a rate of 0.6 is included during training.

5.2.3   Neural Network Benchmarking

Since the two radiative transfer models, `POSSIS` and `SEDONA`, have fundamentally different geometries and are trained on distinct datasets, their corresponding NN surrogate models are also distinct. This difference implies that the performance of the two models should not be directly compared without careful consideration of their respective training datasets and methodologies.

To assess the accuracy of the NN surrogate models, we use the root mean square error (RMSE) as a metric to quantify the average deviation between the predicted and actual light curves. The RMSE is defined as

$$\mathrm{RMSE} = \sqrt{\frac{1}{N}\sum_{i=1}^{N}(y_i - \hat{y}_i)^2}, \tag{5.10}$$

where y_i is the actual value obtained through the radiative-transfer simulation at time t_i, $\hat{y}_i$ denotes the prediction from the surrogate model, and N is the total number of time points.

We compute this metric across the entire parameter grid and all photometric filters. The median RMSE values are found to be 0.103 mag for Bu2019lm (computed over a 14-day period) and 0.485 mag for Ka2017 (computed over a 7-day period). The rationale behind selecting these specific time intervals will be discussed in the next sections.

---

[4] https://github.com/dnkasen/Kasen_Kilonova_Models_2017
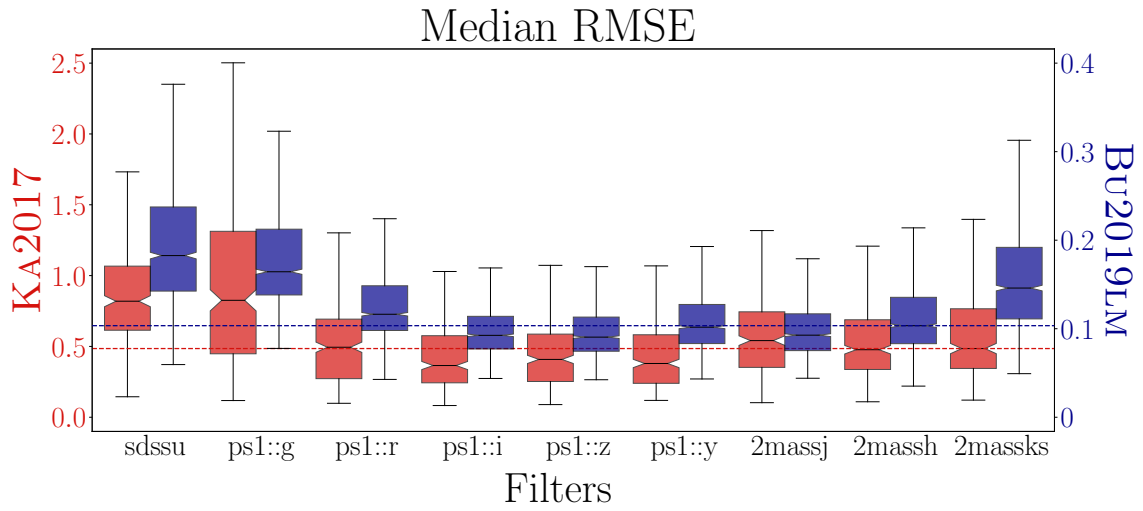
Figure 5.1: Median RMSE values across different photometric filters for the two neural network surrogate models: KA2017 (red, right y-axis) and BU2019LM (blue, left y-axis). Individual box plot represent the median (center-notch), interquartile range (box), and 1.5 times the interquartile range (whiskers) of the RMSE values. Dashed line represents the median RMSE value across entire parameter grid and photometric filters. The BU2019LM model exhibits lower RMSE values across all filters, indicating better agreement with the radiative transfer simulations. The KA2017 model exhibits consistently higher RMSE values across all filters, reflecting greater deviations from the radiative transfer simulations. The disparity between the two models underscores differences in their training datasets, methodologies, and underlying physics. *Note: Extreme outliers are not shown for clarity.*

6 Systematic Uncertainties

*Parts of this chapter are based on the article **Data-driven approach for modeling the temporal and spectral evolution of kilonova systematic uncertainties** by **Sahil Jhawar**, Thibeau Wouters, Peter T. H. Pang, Mattia Bulla, Michael W. Coughlin, and Tim Dietrich published in Physical Review D, Volume 111, Issue 4, February 2025.*

Despite the robustness of `NMMA`'s inference methodology, one of the key challenges in kilonova modeling is the presence of uncertainties, which arise from factors such as nuclear heating rates, opacities, and ejecta morphology, cf. $\boxed{\text{Ch. 2}^{\rightarrow \text{p.4}}}$, all of which evolve over time. Historically, the `NMMA` $\boxed{[151]}$ framework has addressed these uncertainties by applying a fixed systematic uncertainty of 1 magnitude $\boxed{[19,41,151,163]}$, a choice validated by studies demonstrating consistency across different ejecta morphologies $\boxed{[67]}$. However, assuming a fixed uncertainty in the kilonova likelihood function (σ_{sys} in $\boxed{\text{Eq. (5.3)}^{\rightarrow \text{p.32}}}$) can lead to biases in parameter estimation.

More recent approaches have sought to refine this treatment by allowing systematic uncertainty to be sampled as a free parameter $\boxed{[3,164]}$[1], with some works incorporating filter-dependent priors $\boxed{[165]}$. However, systematic uncertainty in kilonova models is not solely filter-dependent but also evolves over time, reflecting changes in opacity descriptions at early epochs $\boxed{[74,142]}$ and non-local thermal equilibrium effects that become significant after about one week $\boxed{[166,167]}$. To address this limitation, this thesis and the corresponding paper introduce a time-dependent error model, which accounts for variations in kilonova properties across different observational epochs. Additionally, the methodology allows for a combined treatment of filter- and time-dependent uncertainties, providing a more nuanced representation of systematic effects. Additionally, we also the treatment of systematic uncertainty as a sampling parameter. These modifications, already implemented in `NMMA`,[2] is model-agnostic and can be applied to any EM model irrespective of the nature of the transient, e.g., also for gamma-ray-burst afterglows or supernovae.

6.1 Implementation Details

6.1.1 Freely Sampled Systematic Uncertainty

In this implementation, systematic uncertainty is treated as a free parameter, denoted by σ_{sys}, which is sampled from a predefined prior probability distribution rather than being fixed. This is expressed as

---

[1]Ref. $\boxed{[3]}$ used the freely sampled systematic error treatment as implemented in commit $\boxed{\text{32aadf8}}$.

[2]See PRs $\boxed{\text{⊙ 383}}$ and $\boxed{\text{⊙ 387}}$.

$$\sigma_{\text{sys}} \sim P(\sigma_{\text{sys}}), \tag{6.1}$$

where $P(\sigma_{\text{sys}})$ represents the prior distribution. The choice of prior can vary depending on empirical constraints, with common choices including a uniform or log-uniform distribution

$$P(\sigma_{\text{sys}}) = \mathcal{U}(a, b), \tag{6.2}$$

or

$$P(\log \sigma_{\text{sys}}) = \mathcal{U}(\log a, \log b). \tag{6.3}$$

During inference, σ_{sys} is sampled along with other parameters, and its effect is incorporated into the likelihood function as the quadrature sum of statistical and systematic uncertainties as illustrated in the denominator of Eq. (5.3) $^{\rightarrow\,\text{p.32}}$. This allows for a more flexible treatment of systematic effects by marginalizing over σ_{sys} in the posterior distribution,

$$P(\vec{\theta}, \sigma_{\text{sys}} \mid d) \propto \mathcal{L}(d \mid \vec{\theta}, \sigma_{\text{sys}}) P(\vec{\theta}) P(\sigma_{\text{sys}}), \tag{6.4}$$

where $\vec{\theta}$ represents the set of model parameters, d is the data, and $\mathcal{L}$ is the likelihood function.

By defining σ_{sys} as a variable sampled from a prior probability distribution, we allow the inference process to adaptively account for systematic effects without fixing them a priori. This flexibility is critical when empirical constraints on systematic uncertainties are uncertain or context-dependent, as it permits the model to adaptively explore the plausible range of σ_{sys} during sampling. As the posterior distribution, Eq. (6.4) $^{\rightarrow\,\text{p.38}}$, integrates this nuisance parameter alongside the model parameters $\vec{\theta}$, this approach also provides a mechanism to assess the goodness of fit by examining the marginalized behavior of σ_{sys} [3].

Model selection

The inclusion of the systematic uncertainty parameter σ_{sys} in the Bayesian evidence is crucial for obtaining an accurate and representative inference of model parameters, particularly in cases where systematic effects may significantly influence the data.

Incorporating σ_{sys} into the Bayesian evidence ensures that all potential systematic effects are properly integrated into the analysis, thus reflecting a more complete description of the data. If σ_{sys} were excluded, the evidence would effectively disregard the systematic uncertainties, leading to an incomplete or biased model of the data. By allowing σ_{sys} to be sampled from a prior distribution, it is possible to marginalize over these uncertainties and evaluate the likelihood of the data under

varying assumptions about the magnitude of systematic errors. This marginaliza-
tion is particularly important in cases when the prior knowledge does not provide
exact estimates for systematic uncertainties, but rather offers a range of plausible
values.

Furthermore, σ_{sys} influences the Bayesian model comparison by affecting the model
evidence, which becomes important while determining the relative plausibility of
competing models. As systematic uncertainties may significantly alter the interpre-
tation of the data, their treatment in the evidence calculation directly impacts the
model selection. Ignoring these uncertainties would undermine the validity of model
comparisons and potentially lead to misleading conclusions about the best-fitting
model. Hence, one may need to be cautious when interpreting the Bayesian evidence
when using such a nuisance parameter.[3]

6.1.2   Time-Dependent Systematic Uncertainty

Radiative transfer models have made significant progress in kilonova modeling, yet
discrepancies persist, particularly at very early times ($<$1 day) and late times
($>$1 week). At early times, the ejecta is extremely hot, dense, and expanding
rapidly, leading to highly ionized atomic states for which opacity data remains incom-
plete [142,168]. Additionally, aspherical geometries complicate spectral modeling,
while inefficient thermalization of radioactive decay products [74,78] affects early
light curve predictions. These challenges hinder accurate parameter estimation from
observed early-time spectra, such as those from `AT2017gfo`.

At later times, as the ejecta expands and cools, it transitions into a nebular phase
where local thermodynamic equilibrium (LTE) approximations break down. The
spectrum becomes dominated by line emission, requiring a full non-LTE treatment,
which is computationally demanding [166]. Furthermore, evolving opacities due to
the recombination of lanthanides and actinides introduce additional uncertainties in
the predicted light curves [169]. Multi-component ejecta structures and viewing-
angle dependencies further complicate light curve interpretations [170]. While
recent advances, such as improved atomic databases and multi-dimensional radiative
transfer models, have helped mitigate these issues, systematic uncertainties remain
a critical challenge for inferring merger properties from kilonova observations.

To address these challenges, we introduce a time-dependent systematic uncertainty
model that accounts for the evolving nature of kilonova properties across different
epochs. Specifically, we define σ_{sys} as a function of time, $\sigma_{\mathrm{sys}}(t)$, allowing systematic
effects to vary over the course of the kilonova event. The systematic uncertainty
is modeled using a piecewise linear interpolation scheme, where $\sigma_{\mathrm{sys}}(t)$ is sampled
from a prior distribution at fixed time intervals during the inference process and
then linearly interpolated at measurement times. Mathematically, this is expressed
as

---

[3]Subtle foreshadowing regarding the analysis of `AT2017gfo`.

$$\sigma_{\text{sys}}(t) = \sigma_n + \frac{\sigma_{n+1} - \sigma_n}{t_{n+1} - t_n} \cdot (t - t_n), \quad \text{for} \quad t_n \leq t < t_{n+1}, \tag{6.5}$$

where $n = 0, 1, ..., N - 1$, N is the total number of sampling times, and σ_n follows a prior distribution $P(\sigma_{\text{sys}})$.

The likelihood function for parameter inference, incorporating both statistical and systematic uncertainties, is given by

$$\mathcal{L}(\vec{\theta}) \propto \exp\left(-\frac{1}{2} \sum_{ij} \frac{\left(m_i^j - m_i^{j,\,\text{est}}(\vec{\theta})\right)^2}{\left(\sigma_i^j\right)^2 + (\sigma_{\text{sys},i})^2}\right), \tag{6.6}$$

where m_i^j is the observed AB magnitude in filter j at time t_i with corresponding measurement error $\sigma_i^j \equiv \sigma^j(t_i)$, while $m_i^{j,\,\text{est}}(\vec{\theta})$ is the estimated AB magnitude for the source parameters $\vec{\theta}$ (e.g., ejecta masses, velocities) from the model. The term $\sigma_{\text{sys},i}$ represents the interpolated systematic error at time t_i.

The described procedure is illustrated in Fig. 6.1 , where black crosses represent the mock data and red line denotes the best-fit light curve.[4] The red-shaded region corresponds to the systematic uncertainty in the best-fit posterior. Additionally, the surrounding Gaussian distribution represents the denominator of Eq. (6.6) , encapsulating both statistical and systematic uncertainties.
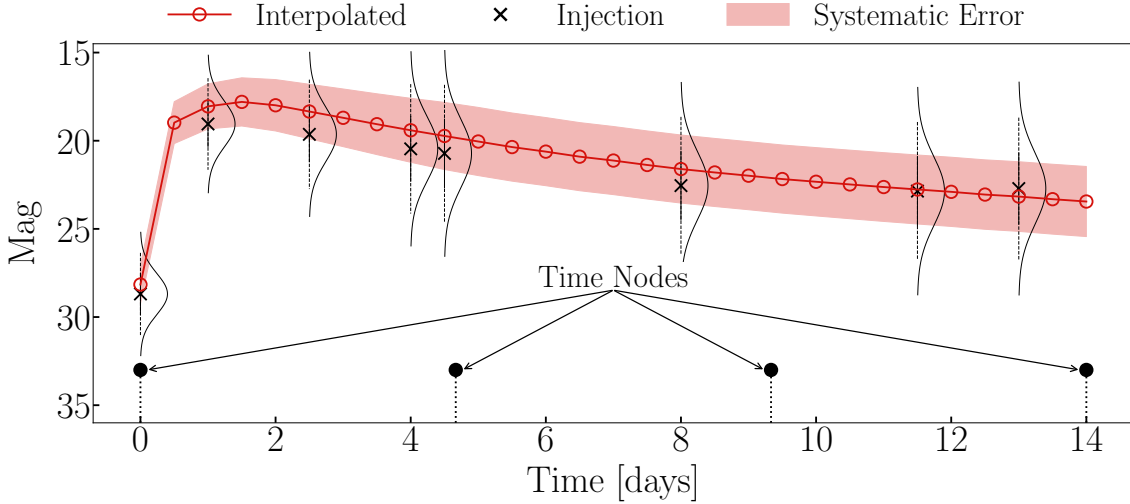
Figure 6.1: The stem plot shows the placement of four time nodes at 0, 4.67, 9.34, and 14 days used for interpolation.

---

[4]Best-fit light curves are obtained by maximizing the likelihood function, also known as Maximum Likelihood Estimation (MLE), where the MLE estimate $\hat{\theta}$ given by, $\hat{\theta} = \arg\max_{\theta \in \Theta} \mathcal{L}(\theta)$. This $\hat{\theta}$ is the set of parameters that maximizes the likelihood function $\mathcal{L}(\theta)$. The light curves are then generated using the best-fit parameters $\hat{\theta}$.

6.1.3   Time- and Filter-Dependent Systematic Uncertainty

At early times, when emission peaks in the ultraviolet and blue bands, significant uncertainties arise due to incomplete atomic data, relativistic expansion effects, and deviations from spherical symmetry. In contrast, late-time infrared emission is affected by non-local thermodynamic equilibrium (non-LTE) conditions, evolving opacities of lanthanides and actinides, and uncertainties in atomic structure data. The distinct sources of error across different spectral regions necessitate a systematic treatment that accounts for their wavelength dependence to improve parameter inference from kilonova observations.

A single, time-independent uncertainty model is insufficient given the spectral evolution of kilonovae, as different opacity sources and thermalization efficiencies dominate at different wavelengths and epochs. The early-time blue emission is particularly sensitive to uncertainties in the opacity of light r-process elements, while late-time infrared emission depends on the complex atomic physics of heavy elements.

To address these challenges, we extend the time-dependent interpolation scheme to incorporate filter-specific systematic errors. This is achieved by defining σ_{sys} as a function of time and filter, $\sigma_{\mathrm{sys}}^{j}(t_i)$, where j denotes the filter index. The selection of filters requiring independent and joint treatment of systematic uncertainties is determined by evaluating the Mean Absolute Deviation (MAD) for each filter and comparing it to the overall MAD computed across all filters. The MAD serves as a statistical measure of dispersion, by determining the variability within individual filters relative to the entire dataset. The filter-specific MAD is computed as

$$\mathrm{MAD}_j = \frac{1}{n_j} \sum_{i=1}^{n_j} |x_{i,j} - \mu_j|, \tag{6.7}$$

where $x_{i,j}$ is the AB magnitude in filter j at time t_i, μ_j is the mean of all AB magnitudes in filter j, and n_j is the total number of data points in filter j. Similarly, the total MAD is calculated as

$$\mathrm{MAD} = \frac{1}{n} \sum_{i=1}^{n} |x_i - \mu|, \tag{6.8}$$

where x_i is the AB magnitude at time t_i, μ is the mean of all AB magnitudes and n is the total number of data points across all available filters.

Given this, the likelihood in is modified to include filter-specific systematic uncertainties, resulting in

$$\mathcal{L}(\vec{\theta}) \propto \exp\left(-\frac{1}{2} \sum_{ij} \frac{\left(m_i^j - m_i^{j,\,\mathrm{est}}(\vec{\theta}) \right)^2}{\left(\sigma_i^j\right)^2 + \left(\sigma_{\mathrm{sys},i}^j\right)^2} \right), \tag{6.9}$$

where $\sigma_{\mathrm{sys},i}^j$ is the interpolated systematic error at time t_i and filter j.

6.2   Validation

To assess the validity of our approach, we performed a series of injection-recovery tests on synthetic light curves generated using the Ka2017 and Bu2019lm models. These synthetic light curves were constructed with a uniform time step of 0.5 days over a duration of 20 days. To simulate real-world observational constraints, such as weather conditions, instrumental limitations, and scheduling gaps, we randomly selected 45% of the data points for analysis.

Since the synthetic light curves generated by these models provide single values at each time step without measurement (statistical) uncertainties, we introduced a random noise to each data point. This noise follows a Gaussian distribution with zero mean and a standard deviation of 0.1 mag, thereby mimicking realistic observational noise. The perturbed light curves then serve as injections for our parameter estimation pipeline.

Given the limitations of the underlying models, we restrict the data used for parameter estimation to the first seven days for Ka2017 and the first fourteen days for Bu2019lm. In particular, we limit the Ka2017 model to one week because some light curves exhibit unphysical features at later epochs, such as an artificial increase in luminosity, likely due to the low signal-to-noise ratio in the underlying simulations at late times (cf. Ch. C$^{\rightarrow\text{p.71}}$).

We then performed cross-matching injection-recovery tests, wherein the light curves generated from Ka2017 were injected into the Bu2019lm model and vice versa. A total of four injection-recovery tests were performed, incorporating different systematic uncertainty treatments: (1) a fixed 1 mag systematic uncertainty, (2) a freely sampled systematic uncertainty, (3) a time-dependent systematic uncertainty, and (4) a time- and filter-dependent systematic uncertainty.

The injection parameters used in this work are motivated by the observed properties of AT2017gfo and are summarized in Tab. 6.1$^{\rightarrow\text{p.43}}$, along with the respective priors. To facilitate a direct comparison between the posterior distributions of the two competing models, we focus primarily on their shared parameters—namely, the luminosity distance, D_L, and the total ejecta mass, $\log_{10} M_{\text{ej}}$. In the case of the Bu2019lm model, the total ejecta mass is defined as the sum of the wind and dynamical ejecta components, $M_{\text{ej}} = M_{\text{ej,wind}} + M_{\text{ej,dyn}}$.

6.2.1   Fixed Systematic Uncertainty

Following Refs. [19,67,151], we first consider a fixed systematic uncertainty of 1 mag for all data points. From Fig. 6.2$^{\rightarrow\text{p.44}}$, it is evident that the assumed 1 mag uncertainty is sufficient for the recovered light curves to reliably approximate the injected light curves, even when different models are used for the injection and recovery. Regarding the recovery of the injected parameters, we find that when the same model is used for both the injection and recovery, the injected parameters are

Parameter \ Model	Bu2019lm		Ka2017	
	Injection	Priors	Injection	Priors
D_L[Mpc]	40	$\mathcal{N}(40, 1.89)$	40	$\mathcal{N}(40, 1.89)$
$\log_{10} M_{\mathrm{ej}}[M_\odot]$			-1.43	$\mathcal{U}(-3, -1)$
$\log_{10} v_{\mathrm{ej}}[\mathrm{c}]$	$-$	$-$	-0.74	$\mathcal{U}(-1, -0.6)$
$\log_{10} X_{\mathrm{lan}}$			-3.38	$\mathcal{U}(-5, -2)$
Φ[deg]	68.69	$\mathcal{U}(15, 75)$		
ι[rad]	0.43	$\mathcal{U}(0, \frac{\pi}{2})$	$-$	$-$
$\log_{10} M_{\mathrm{ej}}^{\mathrm{dyn}}[M_\odot]$	-1.18	$\mathcal{U}(-3, -1)$		
$\log_{10} M_{\mathrm{ej}}^{\mathrm{wind}}[M_\odot]$	-2.25	$\mathcal{U}(-3, -0.5)$		

Table 6.1: Injection values and priors used to generate the mock light curves and perform parameter estimation to test the implemented algorithm.

recovered reliably within the statistical uncertainties, without any noticeable bias. However, when a different model is used for recovery, we observe systematic biases in the recovered posteriors of the source parameters.

In general, the Bu2019lm model recovers the injected values more accurately for both models than the Ka2017 model. This difference can be attribute to the fact, that, the two-component ejecta in the Bu2019lm model provides greater flexibility during light curve fitting.

6.2.2   Freely Sampled Systematic Uncertainty

The inclusion of systematic uncertainty as a freely sampled parameter provides a more realistic representation of the uncertainties encountered in real-world kilonova observations. In this test, the systematic uncertainty is allowed to vary, drawn from a uniform prior between 0 and 2, thereby enabling the inference framework to marginalize over potential deviations between the models and the observed data. The results of this analysis are shown in . While the recovered light curves are largely consistent with the injected light curves, the recovered posteriors exhibit significant deviations, particularly in the ejecta mass parameter.

6.2.2.1   Self-Consistent Injection and Recovery

When performing injection and recovery with the same model, Bu2019lm for both injection and recovery, the light curve fits remain consistent with the injected data. However, despite this agreement in photometric evolution, the posterior distributions indicate that the ejecta mass parameter is not well recovered within the 90% credible interval (CI). The systematic uncertainty posterior is notably high, indicating that the inference framework is compensating for model discrepancies through
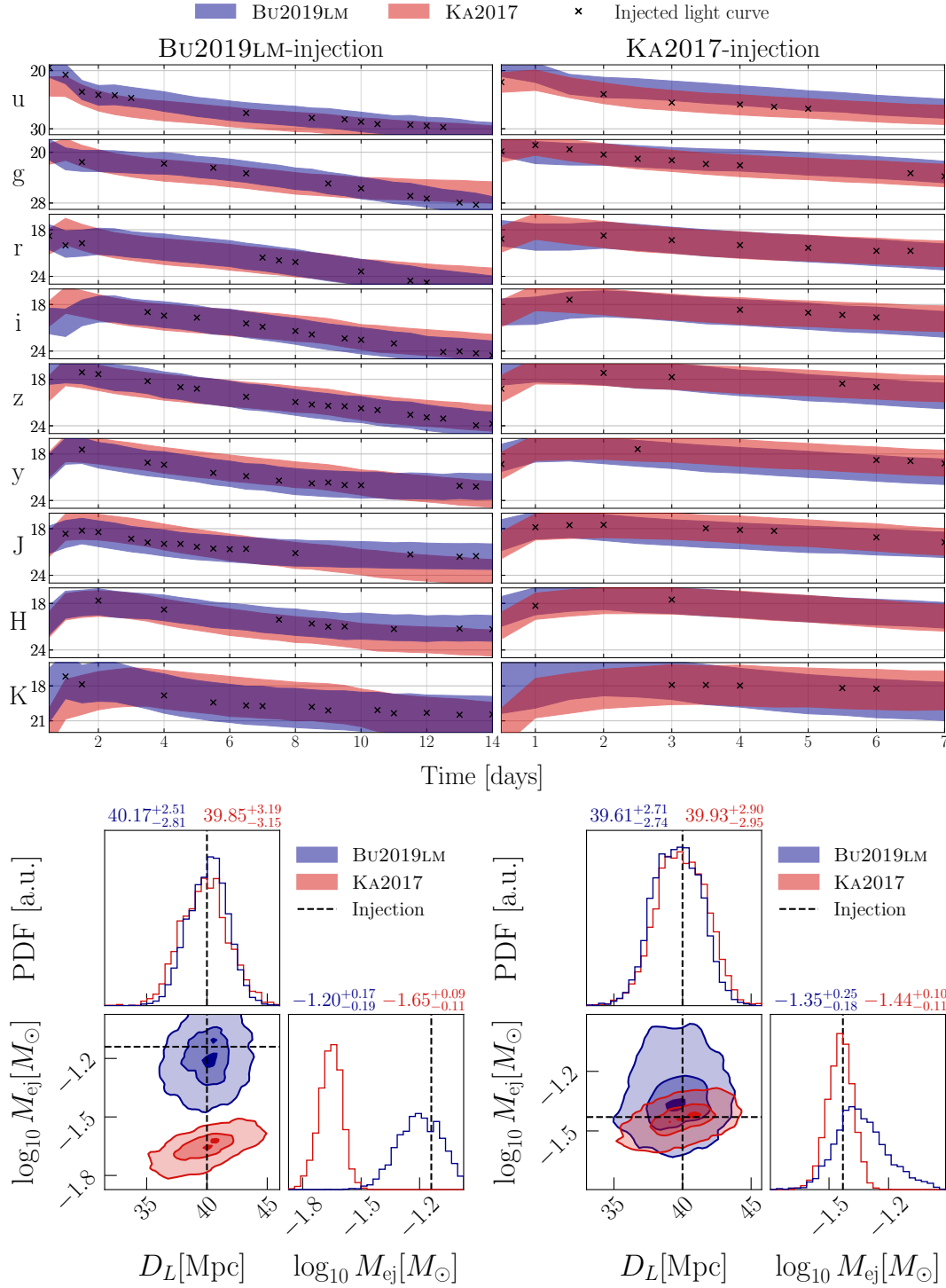
Figure 6.2: *Top panels:* Light curves for the validation test employing a constant 1-magnitude uncertainty. The crosses represent the injected light curve employed as input for the Bayesian inference. The band represents the 90% credibility region of the light curves generated from the posterior samples. *Bottom panels:* 2D marginalised posteriors of Bu2019lm (left) and Ka2017 (right) with injected parameters are indicated by dash lines and shaded region represents the 2σ credible intervals.

systematic uncertainty rather than constraining the physical parameters. This behavior suggests that even within a self-consistent framework, freely sampling systematic uncertainty can obscure the true ejecta properties by absorbing differences between the model and the data.

Similarly, for the KA2017 self-consistent case, the light curve fit remains accurate, and the systematic uncertainty posterior is relatively lower. However, despite the lower inferred systematic uncertainty, the ejecta mass parameter is still not recovered within the 90% CI, suggesting that, KA2017, despite being self-consistent in this scenario, lacks the necessary complexity to fully constrain the ejecta mass.

6.2.2.2 Cross-Model Injection and Recovery

When injecting with the BU2019LM model and recovering with KA2017, the light curve fits remain satisfactory, but the ejecta mass is not recovered reliably. The posterior distribution of systematic uncertainty remains low, suggesting that the KA2017 model can adequately fit the light curves without requiring significant adjustments to systematic uncertainty. However, this comes at the cost of parameter accuracy, as the ejecta mass is poorly constrained. This indicates that KA2017, being a simpler model compared to BU2019LM, forces a fit to the data rather than fully capturing the underlying ejecta physics.

Conversely, when injecting with KA2017 and recovering with BU2019LM, the inference framework is able to recover both the ejecta mass and luminosity distance parameters. However, the posteriors exhibit increased uncertainties, as reflected in the broader light curve credible regions and parameter distributions. This suggests that BU2019LM, having a more flexible two-component ejecta prescription, can better accommodate the KA2017 injection while maintaining some level of parameter recovery. Nonetheless, this flexibility results in wider uncertainties, indicating that while BU2019LM avoids strong biases, it does not necessarily lead to tighter constraints on source properties as compared to KA2017while also trying to compensate for the systematic uncertainties.

6.2.2.3 Discussion

The results indicate a fundamental trade-off between light curve fitting and parameter recovery. In cases where systematic uncertainty is inferred to be low, the light curves are well-matched to the observed data, but the parameter recovery is poor. On the other hand, when systematic uncertainty is inferred to be high, the parameter recovery improves but at the expense of larger uncertainties in both the light curves and posteriors.

Furthermore, model mismatch between injection and recovery plays a significant role in parameter biases. KA2017 recovery struggles to capture the ejecta mass of BU2019LM injections, whereas BU2019LM is more flexible and can accommodate KA2017 injections, albeit with increased uncertainties. This suggests that more

complex models, while providing better overall recovery, may introduce additional uncertainty in their predictions.

A key observation is that KA2017 recovery fails to constrain the ejecta mass, even in self-consistent scenarios. This suggests that the issue is not merely due to systematic uncertainty but is intrinsic to the KA2017 model's ability to constrain the ejecta mass from light curve data. On the other hand, BU2019LM exhibits greater flexibility but at the cost of increased uncertainty.

6.2.3 Time-Dependent Systematic Uncertainties

Relaxing the assumption of a constant 1 mag systematic uncertainty and instead allowing for a time-dependent uncertainty significantly impacts the accuracy of the recovered light curves. This approach acknowledges that systematic uncertainties evolve over time, better reflecting the complexity of real observational data. By permitting systematic uncertainty to vary dynamically, we aim for a more realistic marginalization over model discrepancies and data uncertainties.

6.2.3.1 Self-Consistent Injection and Recovery

Performing self-consistent injection and recovery represents an idealized, best-case scenario where the inference model fully encapsulates the physics governing the injected kilonova light curve. In such a case, we expect the estimated systematic uncertainty, $\sigma_{\mathrm{sys}}(t)$, to remain minimal throughout the entire evolution of the light curve. This expectation is confirmed in our analysis and is evident in $\boxed{\text{Fig. } 6.4^{\rightarrow\,\text{p.49}}}$. The 90% posterior light curve bands remain tightly bound around the injected data, with the injected light curve consistently falling within these bands across all filters and times.

The inferred systematic uncertainty remains on the order of $\mathcal{O}(0.1\mathrm{mag})$, which primarily stems from the observational uncertainties artificially introduced into the injection data. This improved accuracy of the recovered light curves translates directly into more precise parameter inference. Specifically, the posterior distributions of source parameters exhibit a faithful parameter recovery and reduced spread around the injected values, with the width of the posterior shrinking by up to a factor of two. As seen in $\boxed{\text{Fig. } 6.4^{\rightarrow\,\text{p.49}}}$, the posterior distributions for distance and ejecta mass are more tightly constrained around the true injected values compared to the previous scenarios.

6.2.3.2 Cross-Model Injection and Recovery

The impact of time-dependent systematic uncertainty becomes more complex when performing cross-model injection and recovery. When injecting KA2017 light curves, both the KA2017 and BU2019LM models are able to recover the injected parameters within reasonable accuracy. However, a significant difference emerges in the uncertainty of the recovered parameters. The BU2019LM model's posteriors exhibit
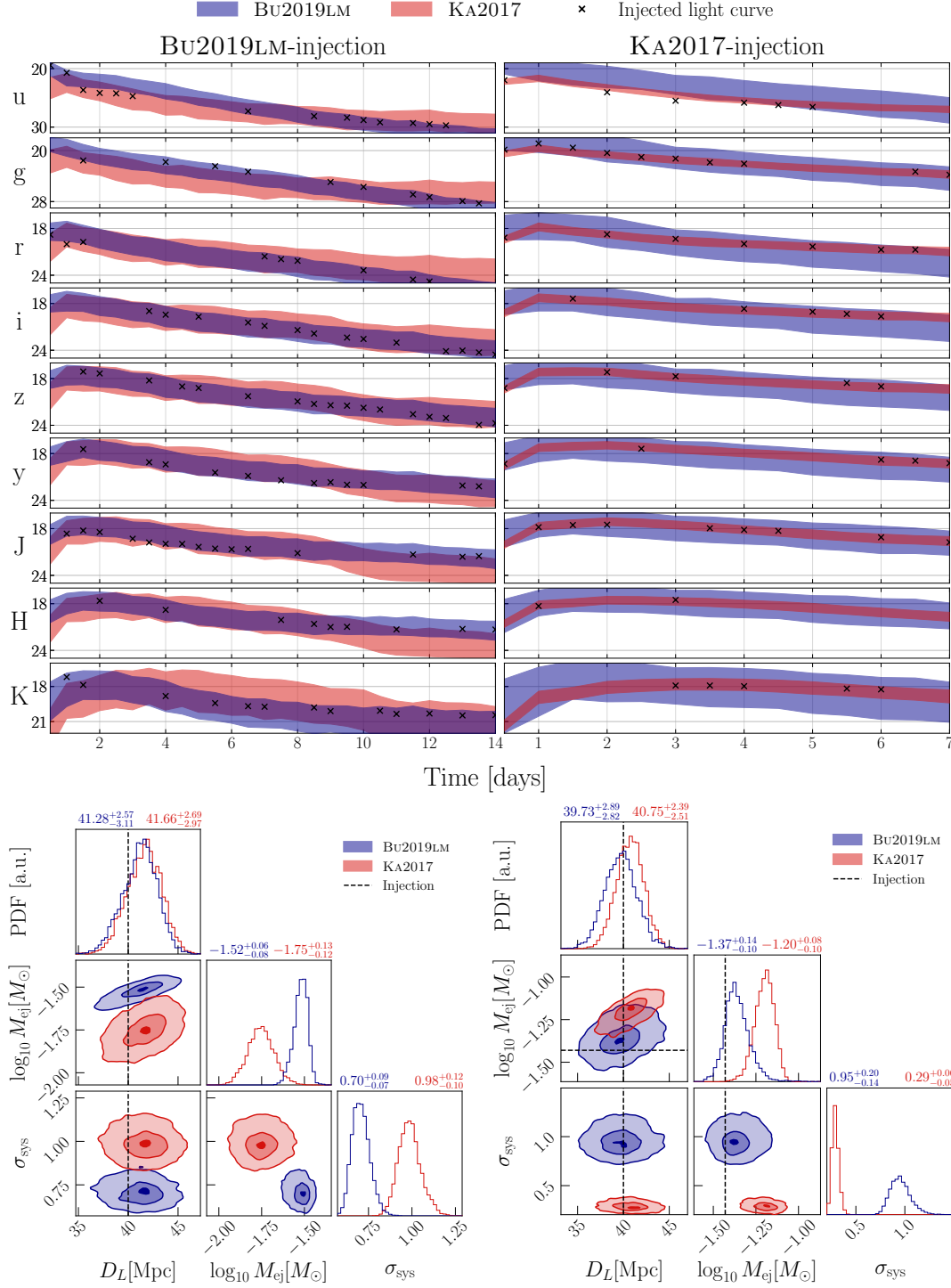
Figure 6.3: Same as Fig. 6.2 → p·44 , for a freely sampled systematic uncertainty.

considerably broader distributions—over five times larger than those of Ka2017. This suggests that Bu2019lm has the flexibility to fit the injected light curves well, but at the cost of increased uncertainty in the recovered parameters. The systematic uncertainty posterior further supports this interpretation, as it shows that Bu2019lm compensates for discrepancies between the models by inflating the inferred uncertainty.

Conversely, the situation is different when injecting Bu2019lm light curves and attempting to recover them using the Ka2017 model. In this case, the recovered ejecta mass deviates significantly from the injected value, indicating a substantial bias in the recovered parameters. The root cause of this discrepancy lies in the fundamental differences between the models. The Ka2017 model, being a spherically symmetric, single-component ejecta model, lacks the flexibility to fully capture the complex structure of Bu2019lm light curves. As a result, it struggles to accurately recover the source parameters, leading to biased posteriors and poor parameter inference.

6.2.3.3   Discussion

These finding underscores the importance of selecting physically motivated models that adequately capture the multi-component nature of kilonovae. While time-dependent systematic uncertainty certainly improves light curve fitting, it cannot fully compensate for a model that lacks the necessary physical complexity. The failure of Ka2017 to recover Bu2019lm injections exhibits the limitations of simplistic ejecta prescriptions.

Nonetheless, time-dependent systematic uncertainty provides a more flexible and realistic approach to modeling observational uncertainties in kilonova light curves. By allowing $\sigma_{\mathrm{sys}}(t)$ to evolve dynamically, we achieve improved light curve fits and reduced parameter uncertainty, particularly when the inference model closely matches the injected model.

The key takeaway is that while systematic uncertainty marginalization can mitigate some model discrepancies, it cannot fully correct for an inadequate physical description. The failure of Ka2017 to recover Bu2019lm injections demonstrates that kilonova models must capture multi-component ejecta structures to provide reliable parameter estimates.

6.2.4   Time- and Filter-Dependent Uncertainties

In our final test analysis, we introduce a time- and filter-dependent uncertainty model, allowing systematic uncertainties to vary not only with time but also across different photometric bands. This approach is motivated by initial tests, particularly those analyzing `AT2017gfo`, which revealed the most significant differences in the ultraviolet (u-band) and infrared (K-band) filters. To account for this, we allow separate systematic uncertainties for the u- and K- bands while grouping all other
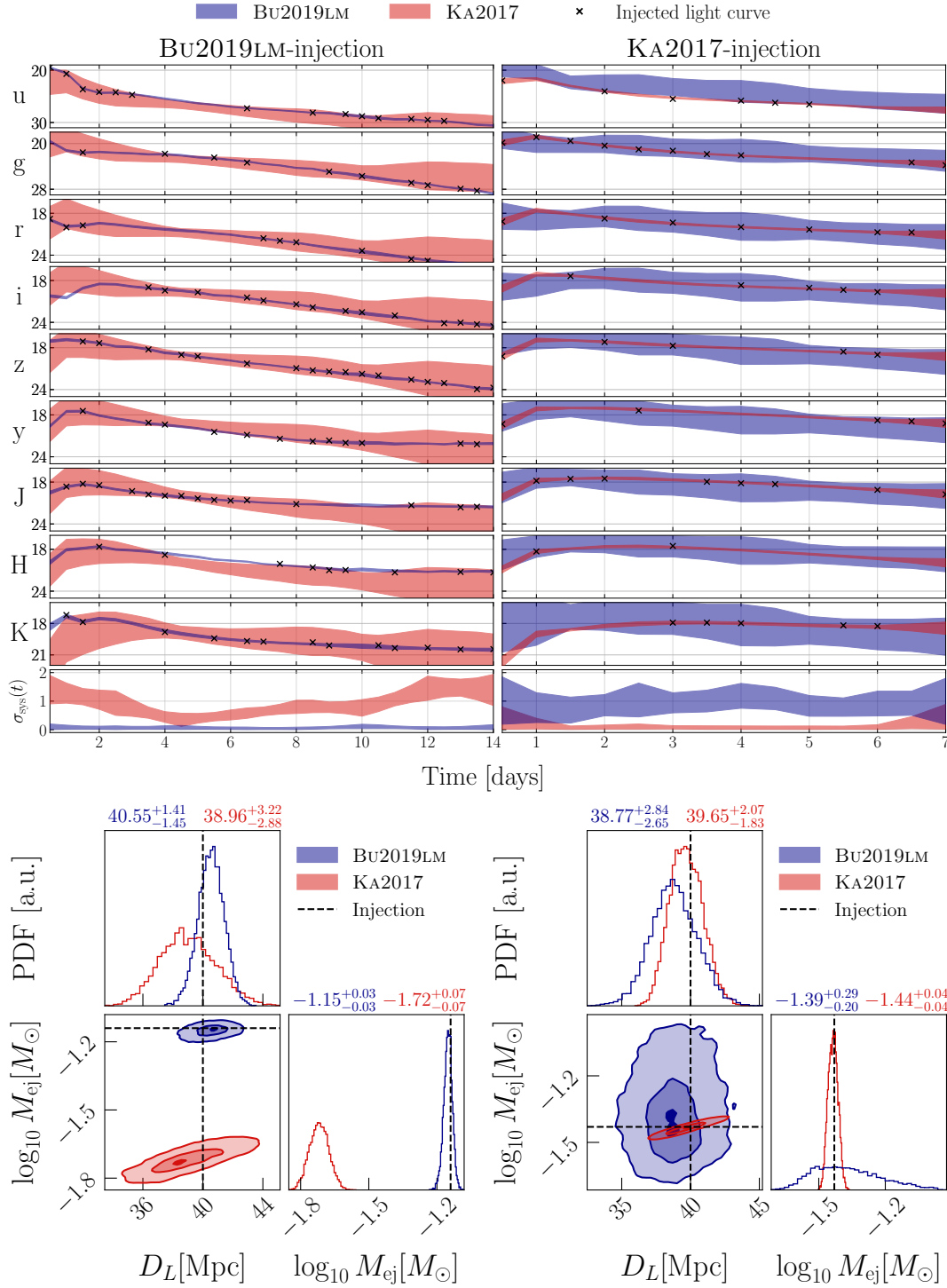
Figure 6.4: Same as Fig. 6.2 $^{\rightarrow\,p.44}$, for time-dependent systematic uncertainty. The bottom panel in the light curve plots illustrates the time-discretized systematic uncertainty, where the band represents the 90% credibility region of the re-interpolated systematic uncertainty, $\sigma_{\mathrm{sys}}(t)$.

bands (g to H) under a single uncertainty parameter.

This choice, while practical, is not unique. A fully generalized approach would involve assigning independent systematic uncertainties to each filter, which could provide even finer control over model discrepancies. However, increasing the number of free uncertainty parameters also introduces computational challenges. Compared to the purely time-dependent uncertainty model discussed in the previous section, our filter-dependent analysis requires three times as many free parameters, significantly increasing the runtime of the inference process. Despite this trade-off, incorporating filter-dependent uncertainties allows us to better assess the impact of model discrepancies in different spectral regions.

6.2.4.1 Self-Consistent Injection and Recovery

As expected, when using the same model for both injection and recovery, the resulting light curve reconstruction remains highly accurate. The inferred systematic uncertainties remain small across all filters, reflecting the fact that the model is trying it's best to encapsulate the underlying physics of the injected kilonova light curve. As a result, the recovered source parameters show minimal deviation from the injected values, with uncertainties comparable to those observed in the purely time-dependent uncertainty case.

This result reinforces our previous findings: when the inference model is well-matched to the true underlying kilonova physics, marginalizing over systematic uncertainty (whether time-dependent or filter-dependent) does not introduce significant bias. Instead, the recovered light curves and posteriors exhibit only minor broadening, reflecting the observational uncertainties rather than fundamental modeling limitations. The consistency of these results suggests that incorporating filter-dependent uncertainties does not fundamentally alter the conclusions drawn from the time-dependent uncertainty approach, at least in the case of self-consistent injection and recovery.

6.2.4.2 Cross-Model Injection and Recovery

The limitations of model-dependent recovery become more pronounced when applying this filter-dependent approach to cross-model injection and recovery. When attempting to recover Bu2019lm injections using the Ka2017 model, we again observe a failure to accurately infer the ejecta mass. This is consistent with our previous findings, where the Ka2017 model—being a single-component ejecta model—lacks the flexibility to fully capture the complex, multi-component structure of Bu2019lm injections.

Despite the added degrees of freedom introduced by filter-dependent uncertainties, the underlying model discrepancies persist. While the inferred light curves may achieve better fits due to the additional flexibility, the posteriors remain biased. This suggests that marginalizing over systematic uncertainties—whether through a time-
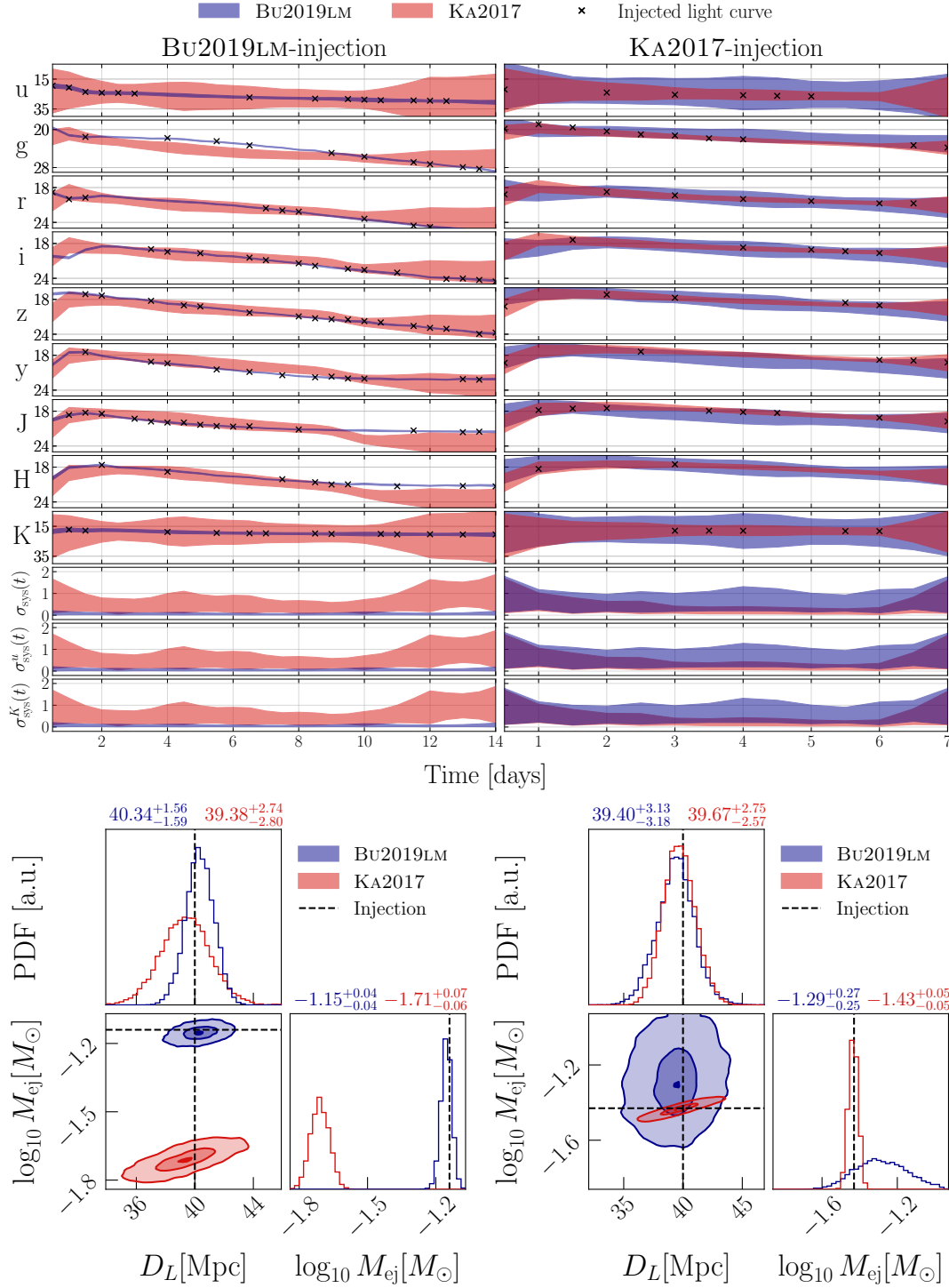
Figure 6.5: Same as $\boxed{\text{Fig. 6.4} \to \text{p.49}}$ for time- and filter-dependent systematic uncertainty. $\sigma_{\text{sys}}^{u}(t)$ and $\sigma_{\text{sys}}^{K}(t)$ represents systematic uncertainty for independently sampled u and K bands, $\sigma_{\text{sys}}(t)$ is for rest all the bands sampled together.

dependent or filter-dependent approach—cannot fully compensate for a fundamental mismatch between the injection and recovery models.

In contrast, when injecting Ka2017 light curves and recovering them with Bu2019lm, the results mirror those of the time-dependent case. The Bu2019lm model successfully fits the injected light curves, perhaps with broader posteriors, particularly for the ejecta mass. This suggests that while Bu2019lm has the flexibility to accommodate Ka2017-like light curves, it does so at the cost of increased parameter uncertainty. The systematic uncertainty posteriors further confirm this interpretation, as they remain elevated, indicating that Bu2019lm compensates for model discrepancies by inflating the inferred uncertainty.

6.2.4.3   Discussion

Our results demonstrate that incorporating filter-dependent uncertainties does not fundamentally alter the conclusions drawn from time-dependent uncertainty models. While allowing systematic uncertainties to vary across different photometric bands improves light curve fits, it does not resolve the underlying issue of model mismatch. In particular, simplistic models like Ka2017 continue to struggle when applied to complex, multi-component ejecta structures, leading to biased parameter inference.

While, the systematic uncertainty marginalization, whether time-dependent or filter-dependent, is a valuable tool for addressing observational uncertainties it still cannot fully correct for deficiencies in the physical modeling of kilonovae. Hence, even with the added flexibility of time- and filter-dependent uncertainties, the uncertainties must be limited at the physical modeling stage.

7 Analyzing `AT2017gfo`

Parts of this chapter are based on the article **Data-driven approach for modeling the temporal and spectral evolution of kilonova systematic uncertainties** *by* **Sahil Jhawar**, *Thibeau Wouters, Peter T. H. Pang, Mattia Bulla, Michael W. Coughlin, and Tim Dietrich published in Physical Review D, Volume 111, Issue 4, February 2025.*

In the previous section, we validated our uncertainty quantification method using synthetic injections. These tests confirmed the robustness of our approach but also highlighted the importance of employing more physically complete models, such as those incorporating non-spherical symmetry when interpreting real observational data. Building on these results, we now apply our uncertainty framework to the observed kilonova `AT2017gfo`. Given the relatively better performance of the Bu2019lm model during our validation tests, we focus exclusively on this model for further analysis. Tab. 7.1 $^{\rightarrow\text{p.53}}$ reports the priors used for the analysis of `AT2017gfo`.

Parameter	Prior
D_L [Mpc]	$\mathcal{N}(40, 1.89)$
Φ [deg]	$\mathcal{U}(15, 75)$
ι [rad]	$\mathcal{U}(0.37, 0.04)$
$\log_{10} M_{\text{ej}}^{\text{dyn}}$ [$M_\odot$]	$\mathcal{U}(-3, -1)$
$\log_{10} M_{\text{ej}}^{\text{wind}}$ [$M_\odot$]	$\mathcal{U}(-3, -0.5)$
σ_{sys}	$\mathcal{U}(0, 2)$

Table 7.1: Priors used for the analysis of `AT2017gfo`.

7.1 Time-Dependent Systematic Uncertainties

An important aspect of this investigation is to assess the impact of the number of time nodes on the inferred posteriors. To this end, we perform parameter estimation using seven different time node configurations, with $N \in \{4, 6, 8, 10, 12, 14, 16\}$. For comparison, we also analyze `AT2017gfo` using a constant 1 mag systematic uncertainty, as well as a freely sampled systematic error modeled as $\sigma_{\text{sys}} = \mathcal{U}(0, 2)$. The results of these analyses are summarized in Tab. 7.2 $^{\rightarrow\text{p.55}}$. The best-fit light curves for different time node configurations are shown in Fig. 7.1 $^{\rightarrow\text{p.54}}$. The recovered posteriors are visualized in Fig. B.5 $^{\rightarrow\text{p.68}}$ and further summarized in Tab. 7.2 $^{\rightarrow\text{p.55}}$.

7.1.1 Impact of Time Nodes on Posterior Distributions

Our results indicate that the number of time nodes has a relatively minor influence on the recovered source parameters. The inferred posteriors remain consistent across
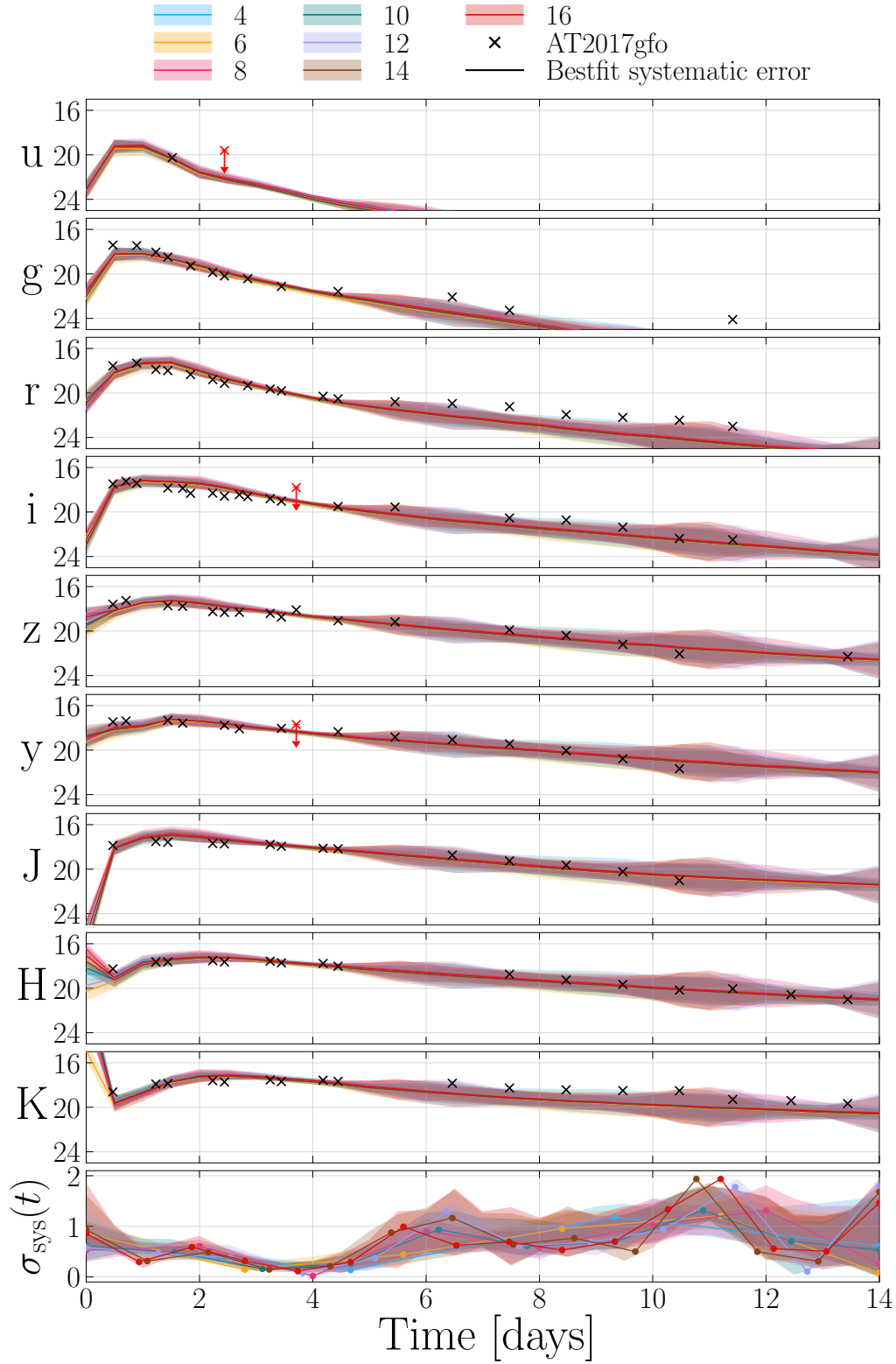
Figure 7.1: Recovered light curves for `AT2017gfo` in different observational bands employing the time-dependent uncertainty method described in the main text. Different colors represent different numbers of employed time nodes. Observational data are marked with black crosses, while red crosses mark the non-detections. The bottom panel illustrates the time-discretized systematic uncertainty, where the circle represents the systematic uncertainty corresponding to the placement of time nodes, and the band represents the 90% highest density interval of the re-interpolated systematic uncertainty, $\sigma_{\mathrm{sys}}(t)$.

Nodes \ Parameter	D_L	Φ	ι	$\log_{10} M_{\mathrm{ej}}^{\mathrm{dyn}}$	$\log_{10} M_{\mathrm{ej}}^{\mathrm{wind}}$	$\ln \mathcal{L}^{\max}$	$\ln \mathcal{L}_{\mathrm{ref}}^{\max}$	Runtime
–	$40.33^{+2.76}_{-2.48}$	$60.53^{+4.77}_{-4.88}$	$0.40^{+0.07}_{-0.09}$	$-1.97^{+0.09}_{-0.07}$	$-1.27^{+0.06}_{-0.05}$	-145.162	-51.648	05 m 57 s
–	$40.53^{+3.05}_{-2.85}$	$60.65^{+7.19}_{-8.99}$	$0.37^{+0.08}_{-0.08}$	$-1.96^{+0.13}_{-0.13}$	$-1.26^{+0.09}_{-0.08}$	-119.275	-25.762	11 m 16 s
4	$42.83^{+2.53}_{-2.78}$	$60.65^{+3.57}_{-4.48}$	$0.40^{+0.08}_{-0.08}$	$-1.91^{+0.08}_{-0.10}$	$-1.27^{+0.07}_{-0.07}$	-98.971	-5.457	20 m 15 s
6	$43.28^{+2.46}_{-2.75}$	$60.64^{+3.50}_{-3.92}$	$0.40^{+0.08}_{-0.08}$	$-1.93^{+0.08}_{-0.10}$	$-1.31^{+0.07}_{-0.08}$	-97.729	-4.215	33 m 47 s
8	$42.75^{+2.52}_{-2.60}$	$60.30^{+3.57}_{-4.76}$	$0.40^{+0.07}_{-0.08}$	$-1.89^{+0.07}_{-0.09}$	$-1.27^{+0.06}_{-0.07}$	-93.514	ref.	46 m 52 s
10	$42.83^{+2.53}_{-2.77}$	$59.97^{+3.74}_{-4.52}$	$0.40^{+0.08}_{-0.08}$	$-1.92^{+0.08}_{-0.10}$	$-1.30^{+0.08}_{-0.08}$	-93.630	-0.116	1 h 02 m 48 s
12	$42.61^{+2.59}_{-2.72}$	$60.81^{+3.58}_{-4.47}$	$0.40^{+0.08}_{-0.08}$	$-1.91^{+0.08}_{-0.10}$	$-1.28^{+0.08}_{-0.08}$	-92.676	0.838	1 h 06 m 50 s
14	$42.54^{+2.52}_{-2.59}$	$60.36^{+3.40}_{-3.91}$	$0.40^{+0.08}_{-0.08}$	$-1.92^{+0.08}_{-0.09}$	$-1.31^{+0.07}_{-0.07}$	-92.530	0.984	1 h 40 m 02 s
16	$42.25^{+2.56}_{-2.70}$	$59.98^{+3.58}_{-4.31}$	$0.40^{+0.08}_{-0.08}$	$-1.91^{+0.07}_{-0.09}$	$-1.31^{+0.08}_{-0.08}$	-92.382	1.132	1 h 46 m 40 s

Table 7.2: Posterior values with 2σ CI, maximum log-likelihoods ($\ln \mathcal{L}^{\max}$), and maximum log-likelihood ratios ($\ln \mathcal{L}_{\mathrm{ref}}^{\max}$) values for `AT2017gfo` with different systematic configuration. *First row:* Values with a constant systematic error of 1 mag. *Second row:* Values with a freely sampled systematic error with a prior of $\mathcal{U}(0,2)$. For runtime comparison, we use 10 cores on an Intel Xeon Platinum 8270 CPU for each run.

different configurations, with their uncertainties overlapping significantly. This suggests that our method remains relatively stable regardless of the specific choice of time nodes, as long as a sufficient number is used to capture the variability of the kilonova light curve.

However, an important trend emerges when examining the behavior of the systematic uncertainty as a function of time. As shown in the bottom panel of Fig. 7.1 [→ p.54], the inferred systematic uncertainty is largest at early times (< 1 day) and at late times (> 5 days). This can be attributed to two key factors:

- Sparse Observational Coverage at Early Times: The scarcity of early-time data points introduces larger uncertainties in the inferred light curves (for e.g., until 2 days there is only one data point in u band and ≤ 4 data points in $zyJHK$ bands). This highlights the critical need for rapid follow-up observations of kilonovae, as emphasized in recent observational studies (e.g., [171]).

- Limitations of the Bu2019lm Model: The systematic uncertainties at early ($\lesssim 1$ day) and late ($\gtrsim 5$ days) times likely reflect intrinsic limitations in the underlying assumptions of the Bu2019lm model. Specifically, early-time uncertainties arise due to the opacities implemented in `POSSIS`, which are computed only for low-ionization states [74,142]. At late times, systematic uncertainties increase as the assumption of local thermodynamic equilibrium starts to break down [166,167].

7.1.2 Selecting an Optimal Time Node Configuration

While all time node configurations yield broadly consistent posterior distributions, an important consideration is determining which setup is sufficiently flexible to represent the underlying systematic uncertainties without introducing excessive computa-
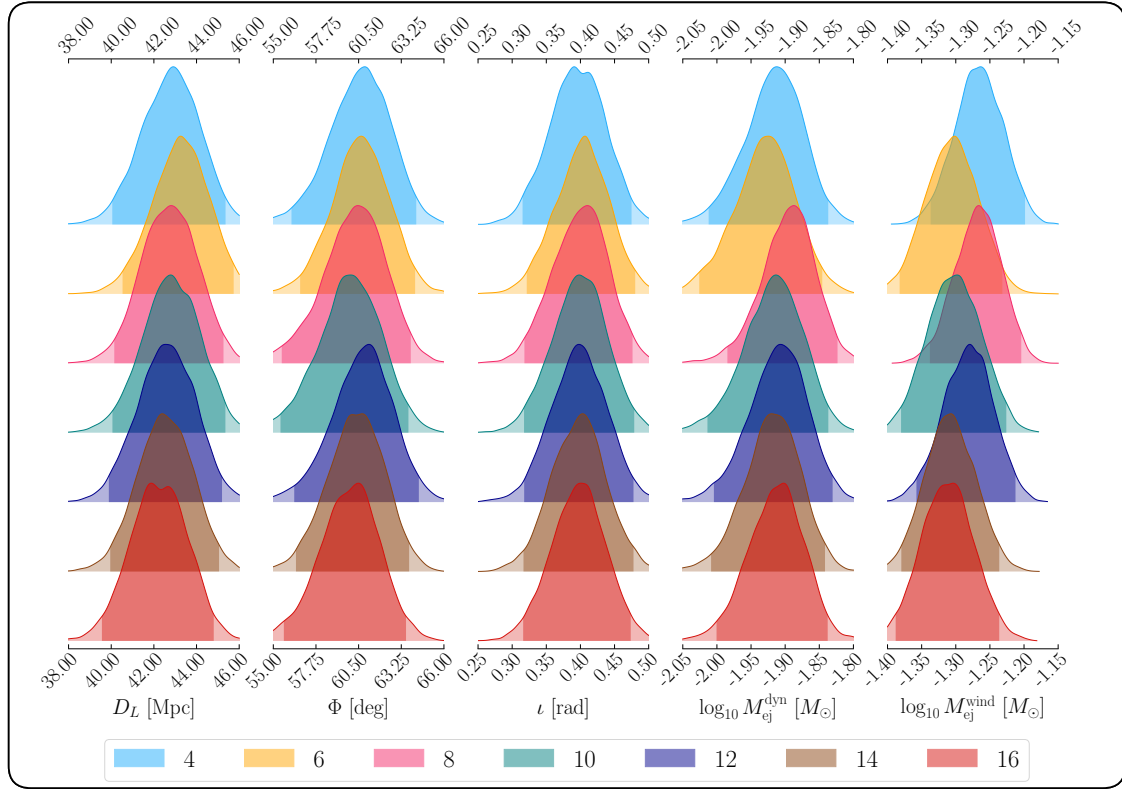
Figure 7.2: Posterior distribution of the recovered source parameters of `AT2017gfo`. Different colors represent different employed number of time nodes.

tional overhead. As mentioned in Sec. 4.1.4$^{\rightarrow\text{p.22}}$, model selection is often performed using Bayes factors. However, in our case, the systematic uncertainty parameters do not represent physical quantities but rather introduce artificial degrees of freedom. To avoid invoking Occam's razor[1] inappropriately, we instead compare the maximum log-likelihood across different configurations, as reported in Tab. 7.2$^{\rightarrow\text{p.55}}$.

As expected, the most flexible configuration, with 16 time nodes, achieves the highest maximum log-likelihood. However, the improvement in log-likelihood is marginal compared to configurations with fewer time nodes, while the computational cost increases substantially. Beyond the eight-time-node configuration, the runtime scales significantly, making higher node configurations computationally expensive without offering proportional gains in model accuracy. Based on this trade-off, we adopt the eight-time-node configuration as our reference for further time- and filter-dependent analysis.

---

[1]Occam's razor is a philosophical principle stating that, among competing hypotheses that explain the same phenomenon, the simplest one is preferred. It suggests that unnecessary complexity should be avoided unless additional assumptions significantly improve explanatory power.

7.2 Time- and Filter-Dependent Systematic Uncertainties

In addition to the previous analyses, we apply our method to `AT2017gfo` while incorporating time- and filter-dependent uncertainties.

The choice of filters to be sampled independently is motivated by the MAD, cf. Sec. 6.1.3$^{\to p.41}$. From Fig. 7.3$^{\to p.57}$, we observe that the u and K bands exhibit the highest positive deviation from the baseline MAD. This indicates that the systematic uncertainties in these bands biases the parameter estimation from those in the other bands, justifying the need to sample them independently.
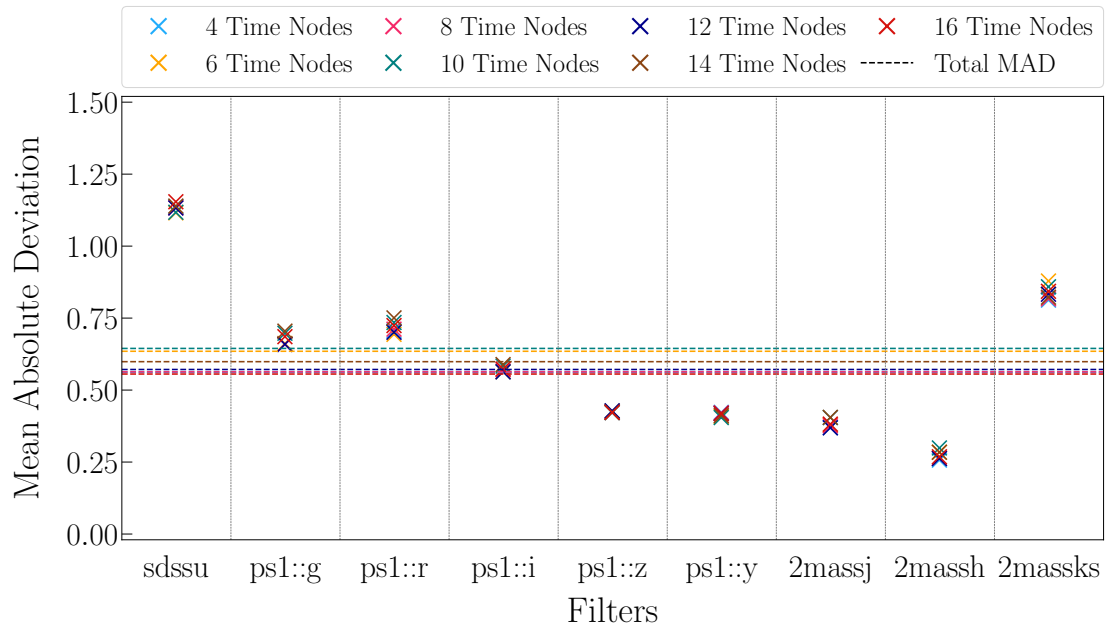
Figure 7.3: MAD plot for `AT2017gfo`. The crosses represent the MAD values for per filter and per time node configuration (Eq. (6.7)$^{\to p.41}$)and dashed line represents the total MAD value per time node configuration (Eq. (6.8)$^{\to p.41}$).

The best-fit light curves obtained from this analysis are presented in Fig. 7.4$^{\to p.59}$, and the recovered source parameters are summarized in Tab. 7.2$^{\to p.55}$.[2] From Fig. 7.4$^{\to p.59}$, it is evident that the systematic uncertainty in the u band remains relatively low, below 1 magnitude for the first six days, despite the presence of only a single detection point. However, after six days, the uncertainty increases as the model struggles to provide an accurate fit due to the sparsity of observational data. For the K band, while for first six days, the error is below 0.5 magnitudes, the uncertainty increases to as high as 2 magnitudes at later times. This is likely due to the fact that for K model is likely to breakdown due to reason discussed previously. The other bands,

---

[2]See Ch. B$^{\to p.68}$ for full posteriors and light curves.

such as z, y, and J, exhibit a more stable behavior, with uncertainties remaining below 1 magnitude throughout the observed time range.

Although, introducing the filter-dependent systematic uncertainty leads to a substantial increase and decrease in the maximum log-likelihood compared to the 8 time nodes configuration of filter-independent uncertainty approach, the recovered parameters themselves remain largely unchanged (cf. Tab. B.1$^{\rightarrow\text{p.68}}$). This suggests that model uncertainties are absorbed by the systematic error term, there by inflating the uncertainties in the light curves.
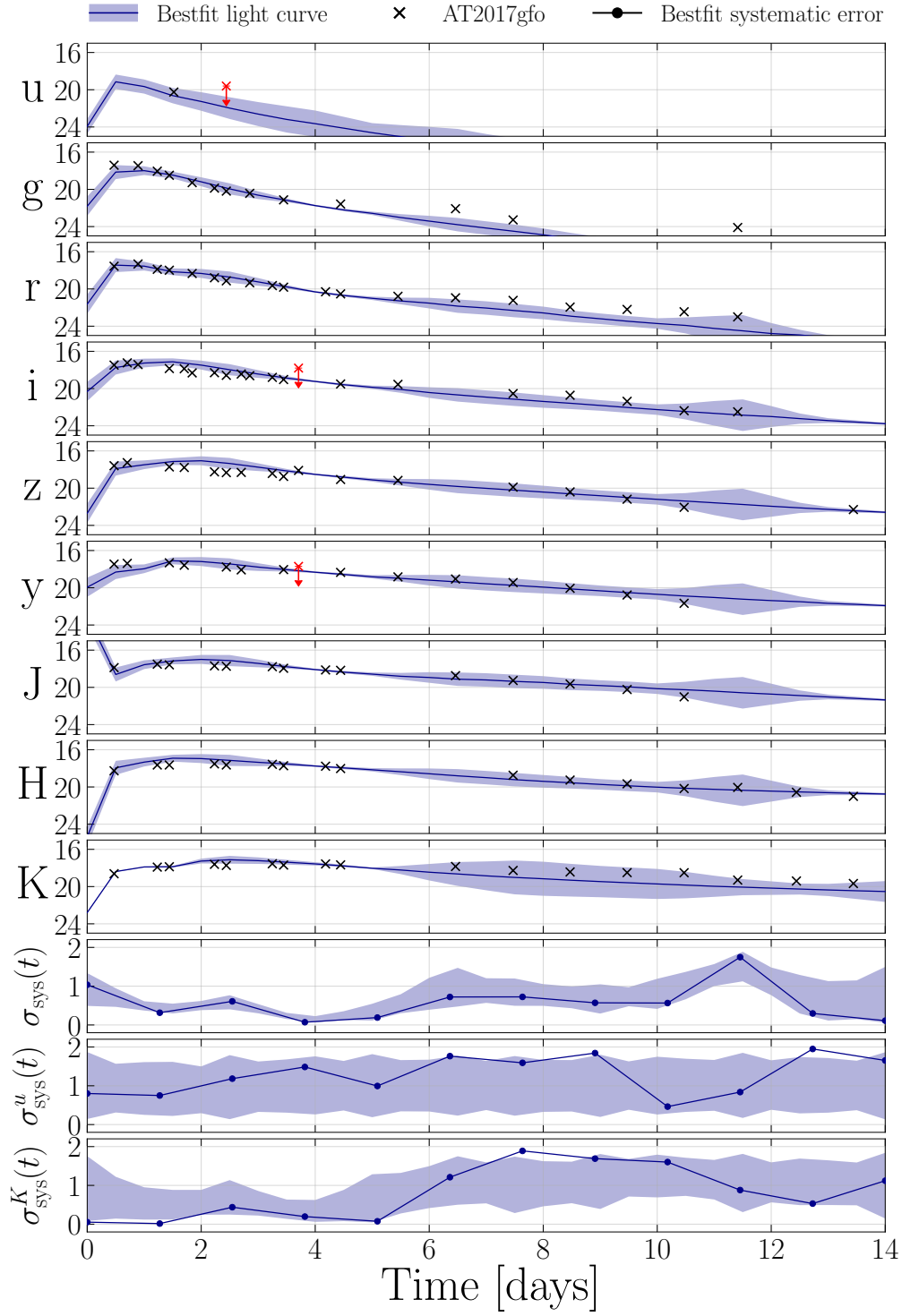
Figure 7.4: Same as Fig. 7.1 →p.54 , for 12 time nodes. $\sigma_{\mathrm{sys}}^{u}(t)$ and $\sigma_{\mathrm{sys}}^{K}(t)$ represents systematic uncertainty for independently sampled u and K band, $\sigma_{\mathrm{sys}}(t)$ represents the systematic uncertainty for all other bands sampled together.

*8*Conclusion

In this thesis, we have developed and validated a comprehensive framework for quantifying systematic uncertainties in kilonova light curve modeling, with particular emphasis on their time and filter dependencies. Through a systematic investigation of different uncertainty parameterizations, we have demonstrated that properly accounting for these uncertainties is crucial for accurate parameter inference in kilonova observations.

Our validation tests using synthetic light curves from the Ka2017 and Bu2019lm models revealed several important findings. First, when using a fixed systematic uncertainty approach (1 mag), we observed that parameters could be recovered accurately within statistical uncertainties when the same model was used for both injection and recovery. However, significant biases emerged during cross-model analyses, highlighting the inherent limitations of simplistic models and uncertainty treatments.

The freely sampled systematic uncertainty approach, while providing more flexibility, illustrated a fundamental trade-off between light curve fitting and parameter recovery. Low inferred systematic uncertainties often corresponded to well-fitted light curves but poor parameter recovery, while high inferred uncertainties improved parameter recovery at the cost of larger uncertainties in light curves and posteriors.

A key insight from our work is that time-dependent systematic uncertainties significantly improved parameter recovery across all scenarios. By allowing uncertainties to evolve dynamically over time, we achieved more accurate light curve fits and reduced parameter uncertainty, particularly when the inference model closely matched the injected model. This approach proved especially valuable in self-consistent scenarios, where the estimated systematic uncertainty remained minimal throughout the light curve evolution.

Our most sophisticated approach, involving both time and filter dependence in systematic uncertainties, provided additional flexibility by allowing uncertainties to vary not only with time but also across different photometric bands. While this approach improved light curve fits, it did not fundamentally alter our conclusions regarding model mismatch. In particular, simplistic models like Ka2017 continued to struggle when applied to complex, multi-component ejecta structures, leading to biased parameter inference regardless of uncertainty treatment.

Application of our methodology to `AT2017gfo` revealed that systematic uncertainties are most prominent at early times (<1 day) and late times (>5 days). This pattern reflects both observational limitations (sparse early-time coverage) and inherent model limitations (opacity approximations at early times and breakdown of local thermodynamic equilibrium assumptions at late times). Our analysis of `AT2017gfo` using different time node configurations showed that while all configurations yielded

broadly consistent posterior distributions, an eight-time-node configuration offered the optimal balance between flexibility and computational efficiency.

Perhaps most significantly, our work demonstrates that while systematic uncertainty marginalization can mitigate some model discrepancies, it cannot fully compensate for fundamental limitations in physical modeling. The persistent failure of KA2017 to recover BU2019LM injections underscores the critical importance of employing physically complete models that accurately capture the multi-component nature of kilonovae.

The framework developed in this thesis represents a significant advancement in uncertainty quantification for kilonova modeling and can be readily extended to other electromagnetic transient phenomena. By providing a more nuanced approach to systematic error treatment, our work contributes to improving the reliability of parameter estimation in future kilonova observations, which will be crucial for extracting meaningful astrophysical insights from upcoming gravitational wave events with electromagnetic counterparts.

As we enter an era of multi-messenger astronomy with increasingly sensitive gravitational wave detectors and rapid electromagnetic follow-up capabilities, the accurate characterization of kilonova properties will play an essential role in constraining neutron star equation of state, heavy element nucleosynthesis, and cosmological parameters. The methodologies developed in this thesis provide a robust foundation for these future endeavors by ensuring that parameter uncertainties accurately reflect both statistical and systematic sources of error.

$\mathcal{A}$ POSSIS Systematics

As highlighted in Ch. 2$^{\rightarrow p.4}$ and Sec. 3.1$^{\rightarrow p.15}$, the luminosity of a kilonova is affected the opacity of the ejecta material, governed by how easily photons can escape from the expanding ejecta, thereby shaping both the peak brightness and the temporal evolution of the light curve.

To systematically investigate the role of opacity in shaping the observable light curves, we perform POSSIS simulations by scaling the opacity κ by a scaling factor $\alpha \in \{0.5, 1, 2\}$ and compute the synthetic light curves. These scalings do not correspond to physically different compositions but rather mimic the uncertainty or variability in opacities due to, for example, incomplete atomic data or variations in ejecta ionization states.

Fig. A.1$^{\rightarrow p.63}$ shows the resultant broadband light curves for 11 viewing angles (uniformly distributed in cosine of observation angle), across three values of opacity scaling. With $\alpha = 1$, the fiducial opacity κ is used without modification. The case of $\alpha = 0.5$ corresponds to a reduced opacity, allowing photons to diffuse more readily through the ejecta, resulting in a brighter and earlier-peaking kilonova. In contrast, increasing the opacity by a factor of two ($\alpha = 2$) leads to a delayed and fainter emission profile due to longer photon diffusion timescales and increased trapping of radiation within the ejecta.

An additional observation from the opacity-scaling is that light curves computed with higher opacity values (i.e., $\alpha = 2$) exhibit more erratic and noisy behavior. This effect is most noticeable in the $\theta = 90°$ (equatorial) viewing direction, where the line-of-sight optical depth is already higher due to the geometry of the ejecta. This variability can be attributed to the fact that, with higher opacity, photons undergo more scatterings and absorptions before escaping the ejecta. This results in a more complex and stochastic propagation history for each photon packet. Even small differences in the location of emission or path taken can significantly affect the final observed flux, leading to increased variability in the light curve, especially when sampled over discrete time bins.

Moreover, at high opacity, photon packets can become "trapped" for longer periods, undergoing a large number of interactions. This increases the computational burden and decreases the statistical efficiency of the sampling. Unless the number of photon packets is dramatically increased (which becomes computationally expensive), this leads to larger shot noise and visible fluctuations in the synthetic light curves.

Relevance to Systematic Uncertainties in Kilonova Modeling

This opacity-scaling analysis provides a physically motivated illustration of how microphysical modeling uncertainties propagate into observable features of kilonova light curves. Variations in opacity encapsulate systematic errors arising from un-
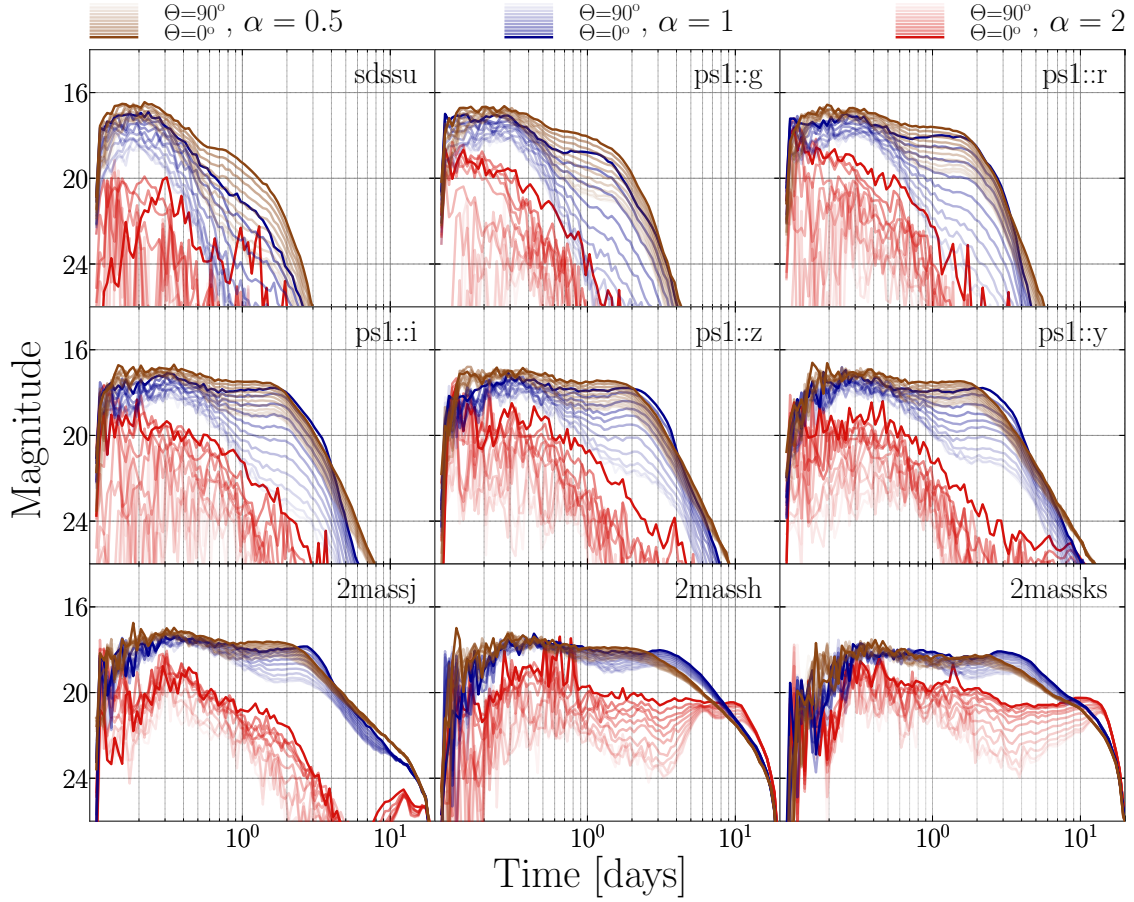
Figure A.1: Light curve plots from `POSSIS` simulations with scaled opacity. The light curves are shown for opacities scaled by factor of α (0.5, 1.0, and 2.0). All magnitudes are computed assuming a luminosity distance of 40 Mpc.

certain atomic physics, ionization conditions, and thermalization processes—factors that are particularly impactful at early and late times. Because opacity[1] directly influences photon diffusion, even small deviations can lead to observable differences in brightness and temporal structure, introducing degeneracies between ejecta properties and radiative transfer assumptions.

The increased irregularity observed at higher opacities further highlights the interplay between physical uncertainty and numerical limitations. These effects underscore the necessity of modeling frameworks that do not assume fixed or static uncertainties but instead allow for time- and filter-dependent treatments, as developed in this thesis.

---

[1]We encourage the readers to refer Refs. [74,76,142,172] for a detailed discussion on the opacities.

AT2017gfo Plots

Constant Systematic Uncertainty
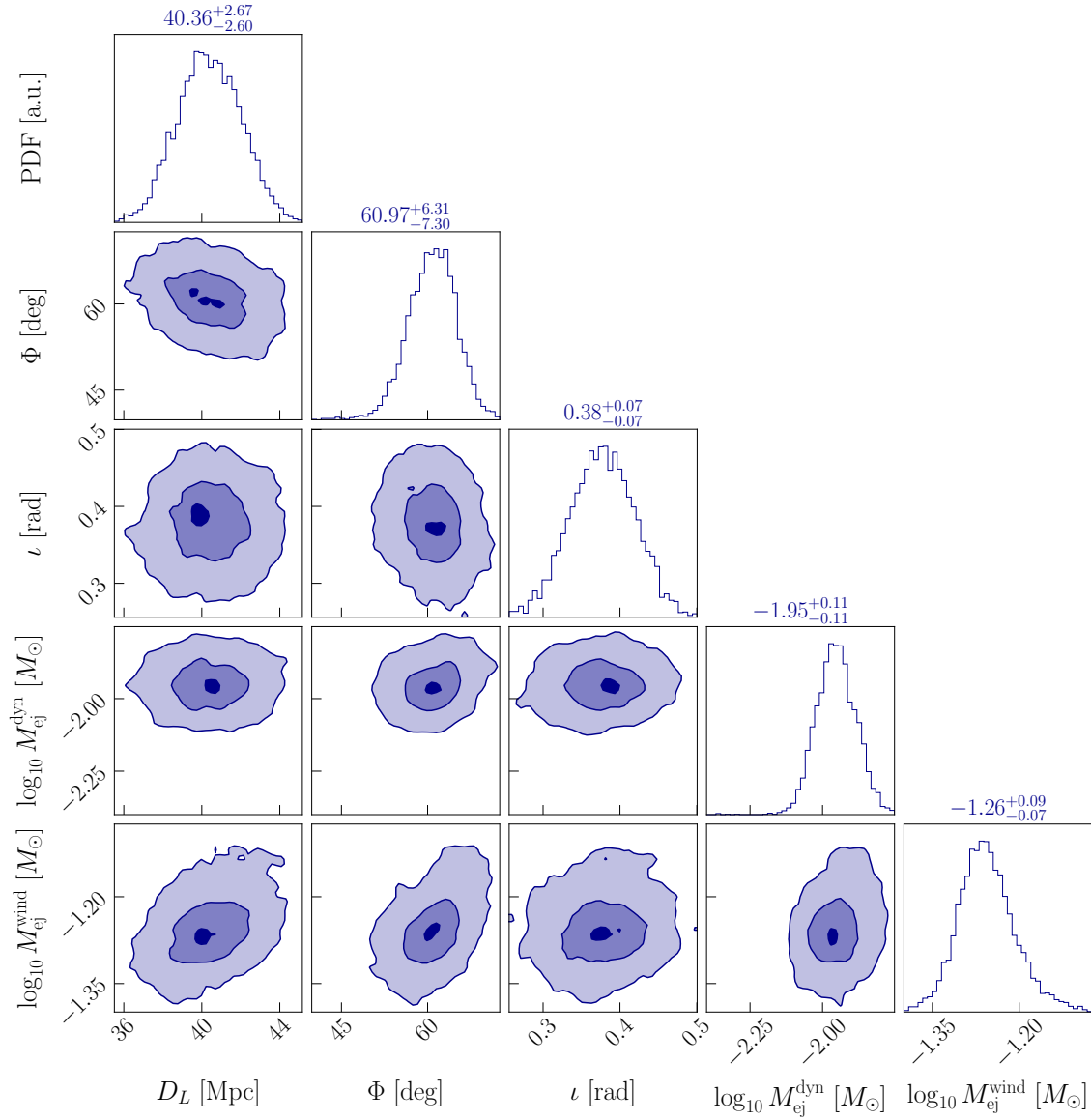
Figure B.1: 2D posterior distributions for the AT2017gfo with a constant systematic uncertainty of 1 mag.
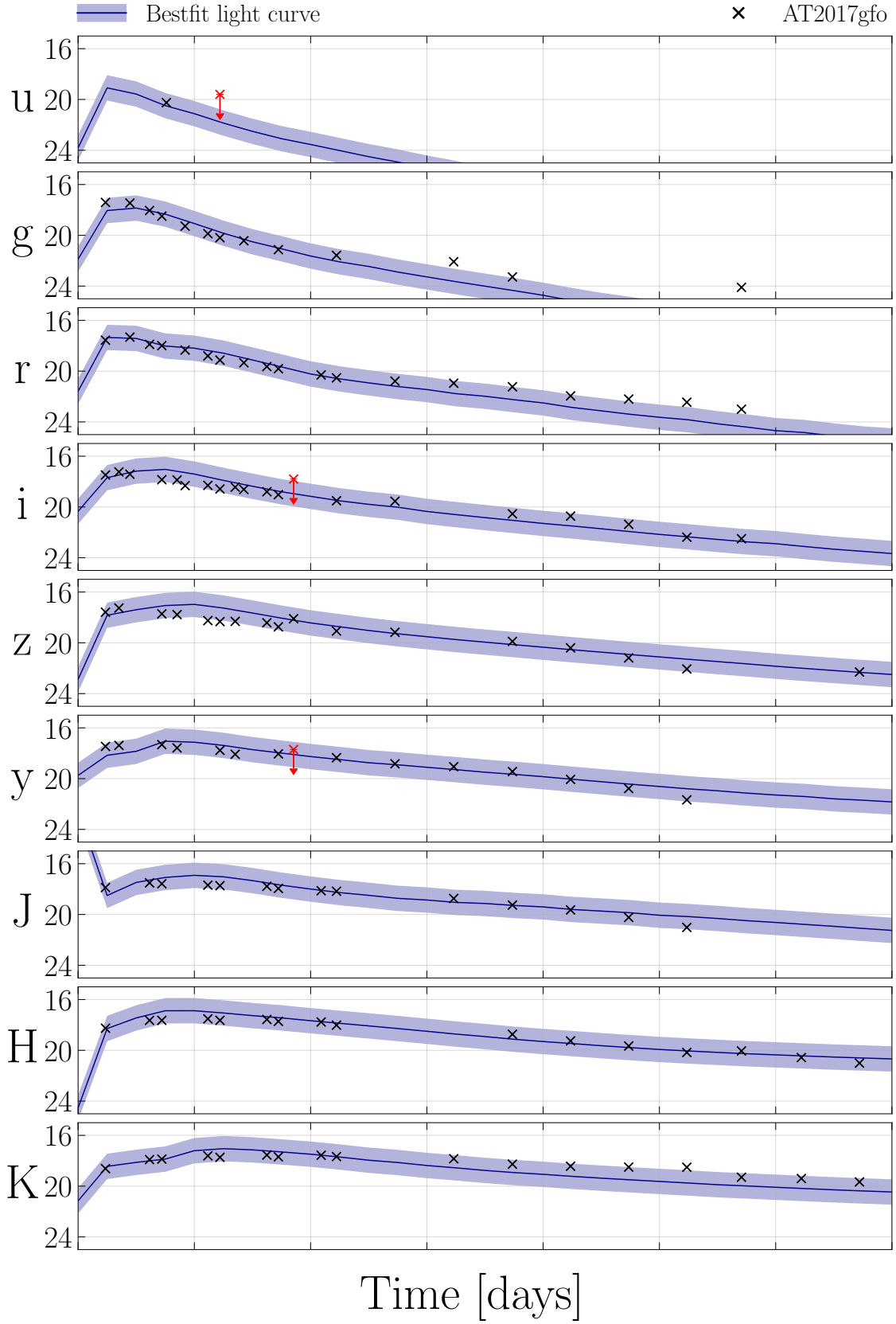
Figure B.2: Light curve fits for the `AT2017gfo` with a constant systematic uncertainty of 1 mag. The band represents the 1 mag systematic uncertainty, solid line represents the best-fit light curve, black cross represents the observed data and red cross with downward arrow represents the non detection upper limit.

Freely Sampled Systematic Uncertainty
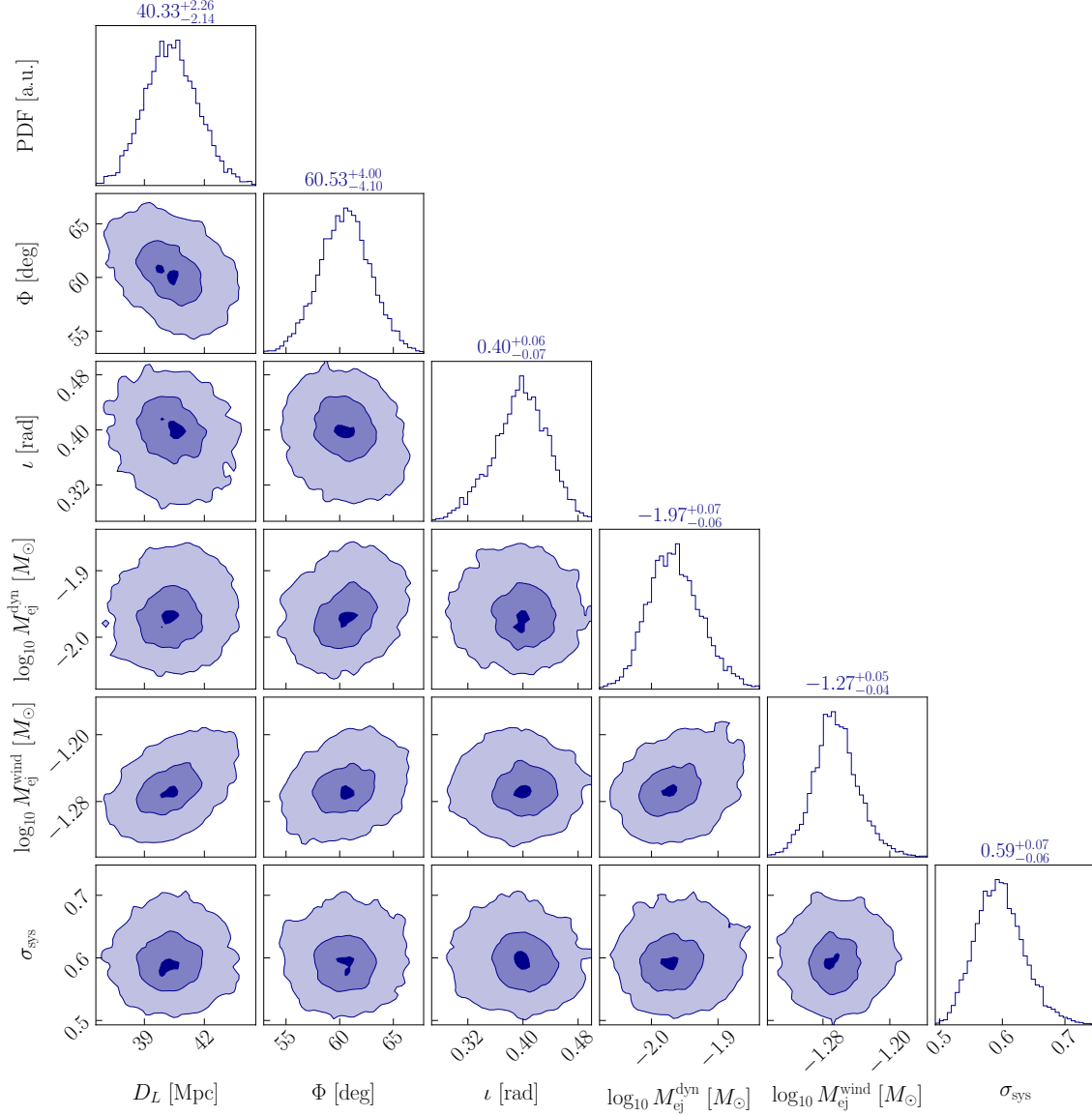
Figure B.3: 2D posterior distributions for the `AT2017gfo` with a systematic uncertainty sampled from $\mathcal{U}(0, 2)$.
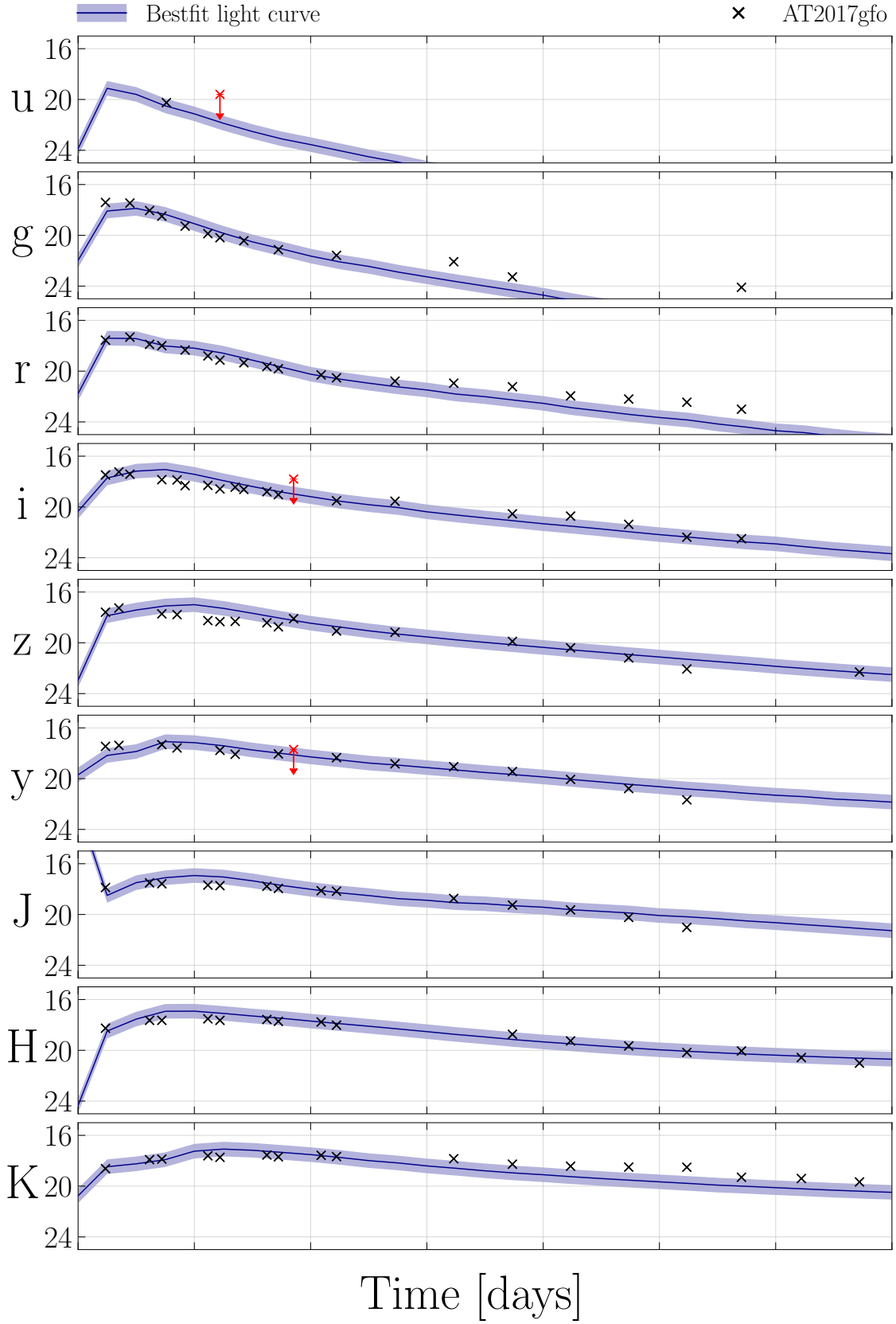
Figure B.4: Light curve fits for the `AT2017gfo` with a systematic uncertainty sampled from $\mathcal{U}(0, 2)$. The band represents the best-fit systematic uncertainty (0.58 mag), solid line represents the best-fit light curve, black cross represents the observed data and red cross with downward arrow represents the non detection upper limit.

Time- and Filter- Dependent Systematic Uncertainties

Parameter Nodes	D_L	Φ	ι	$\log_{10} M_{\text{ej}}^{\text{dyn}}$	$\log_{10} M_{\text{ej}}^{\text{wind}}$	$\ln \mathcal{L}^{\text{max}}$	$\ln \mathcal{L}_{\text{ref}}^{\text{max}}$	Runtime
4	$41.07^{+2.18}_{-2.06}$	$61.48^{+3.92}_{-3.61}$	$0.40^{+0.07}_{-0.07}$	$-1.99^{+0.07}_{-0.05}$	$-1.28^{+0.05}_{-0.05}$	-99	-5.486	35 m 11 s
6	$41.43^{+2.52}_{-2.42}$	$61.52^{+3.89}_{-3.71}$	$0.40^{+0.07}_{-0.07}$	$-1.99^{+0.08}_{-0.05}$	$-1.29^{+0.05}_{-0.05}$	-99.187	-5.673	1 h 1 m 18 s
8	$40.95^{+2.34}_{-2.13}$	$60.64^{+3.82}_{-3.91}$	$0.40^{+0.07}_{-0.07}$	$-1.99^{+0.07}_{-0.05}$	$-1.30^{+0.04}_{-0.05}$	-93.873	-0.359	1 h 11 m 42 s
10	$41.05^{+2.57}_{-2.22}$	$61.27^{+3.78}_{-3.90}$	$0.40^{+0.07}_{-0.07}$	$-1.99^{+0.08}_{-0.05}$	$-1.30^{+0.04}_{-0.05}$	-93.792	-0.278	1 h 51 m 11 s
12	$40.95^{+2.60}_{-2.14}$	$61.33^{+3.67}_{-3.49}$	$0.40^{+0.07}_{-0.07}$	$-1.99^{+0.07}_{-0.05}$	$-1.29^{+0.04}_{-0.04}$	-87.672	5.842	2 h 39 m 27 s
14	$41.94^{+2.45}_{-2.35}$	$60.74^{+3.41}_{-3.38}$	$0.40^{+0.07}_{-0.07}$	$-1.98^{+0.08}_{-0.06}$	$-1.29^{+0.05}_{-0.05}$	-88.447	5.067	3 h 25 m 29 s
16	$41.00^{+2.50}_{-2.10}$	$60.03^{+3.85}_{-3.88}$	$0.40^{+0.07}_{-0.07}$	$-1.98^{+0.08}_{-0.06}$	$-1.29^{+0.04}_{-0.05}$	-90.513	3.001	3 h 31 m 3 s

Table B.1: Posterior values with 2σ CI, maximum log-likelihoods ($\ln \mathcal{L}^{\text{max}}$), and maximum log-likelihood ratios ($\ln \mathcal{L}_{\text{ref}}^{\text{max}}$) values for `AT2017gfo` with different filter-dependent systematic configuration. $\ln \mathcal{L}_{\text{ref}}^{\text{max}}$ are computed against the $\ln \mathcal{L}^{\text{max}}$ of 8 time-node configuration from .
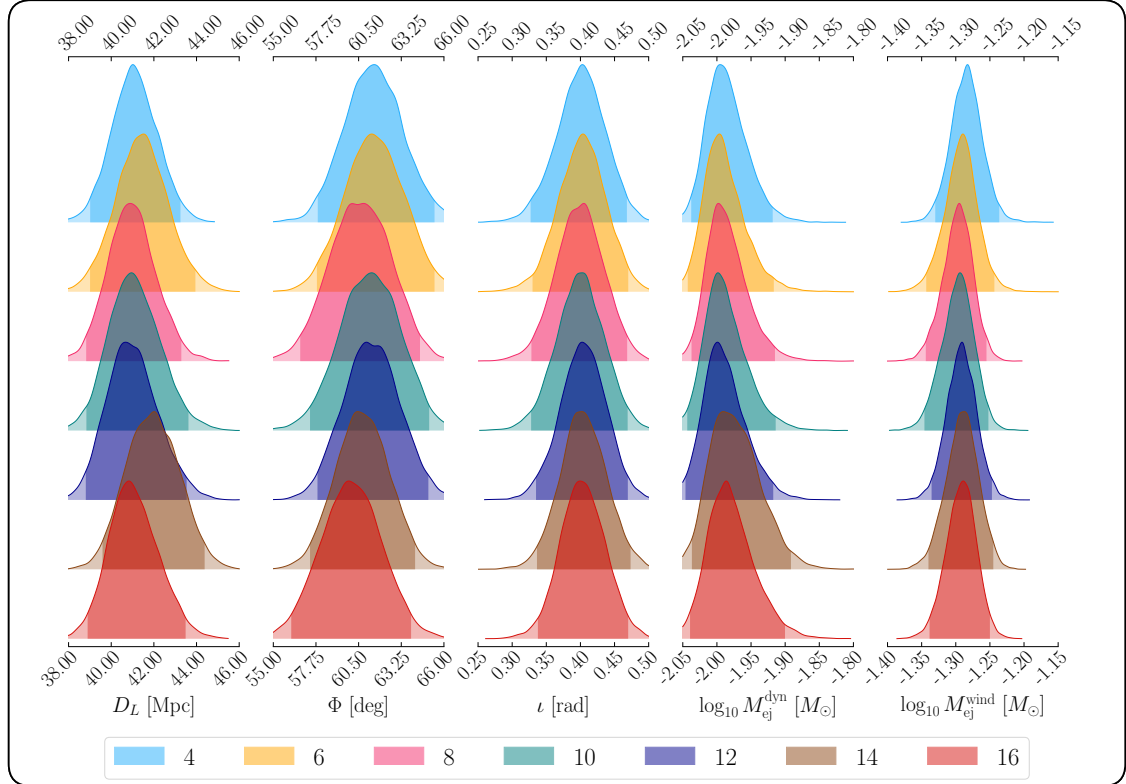
Figure B.5: Posterior distribution of the recovered source parameters of `AT2017gfo`. Different colors represent different employed number of time nodes.
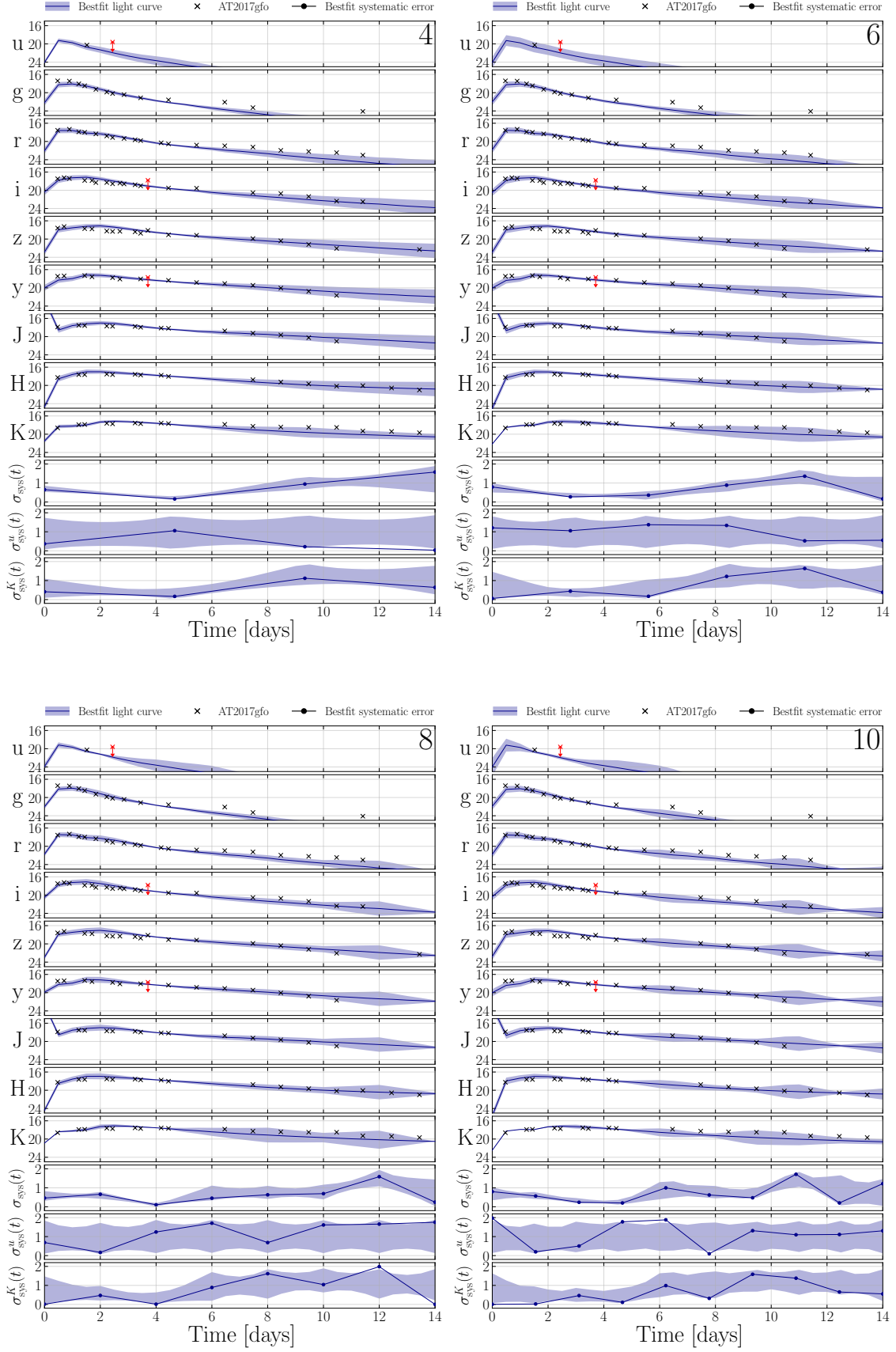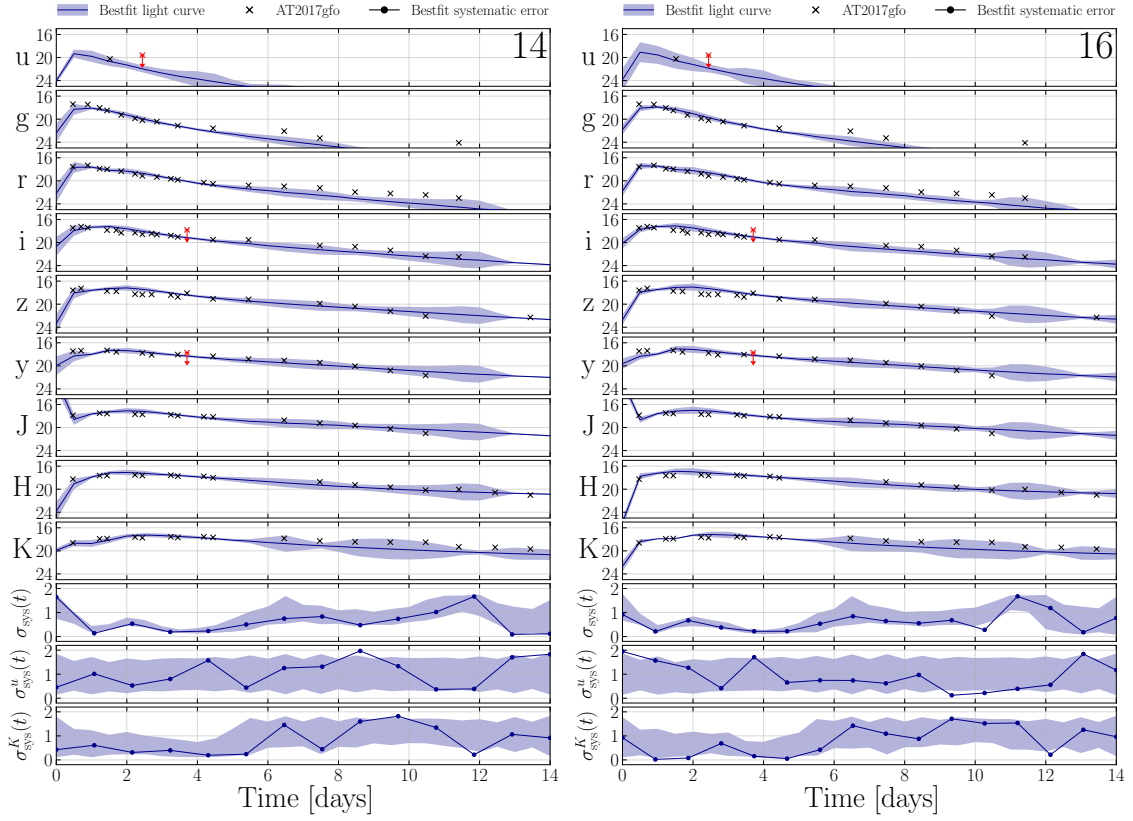
Figure B.6: Same as Fig. 7.4 → p.59. The number on the top panel indicates the number of time nodes.

SEDONA Light Curves

Here, we present eleven light curves from the `SEDONA` model grid, each exhibiting a characteristic drop in magnitude at approximately 8-10 days (gray shaded region). Given this behavior, we restricted the use of `SEDONA` light curves to the first seven days in the main text to ensure a more consistent and reliable analysis. By limiting the time range, we focus on the phase where the model remains well-constrained and avoids potential biases introduced by uncertainties in late-time evolution.
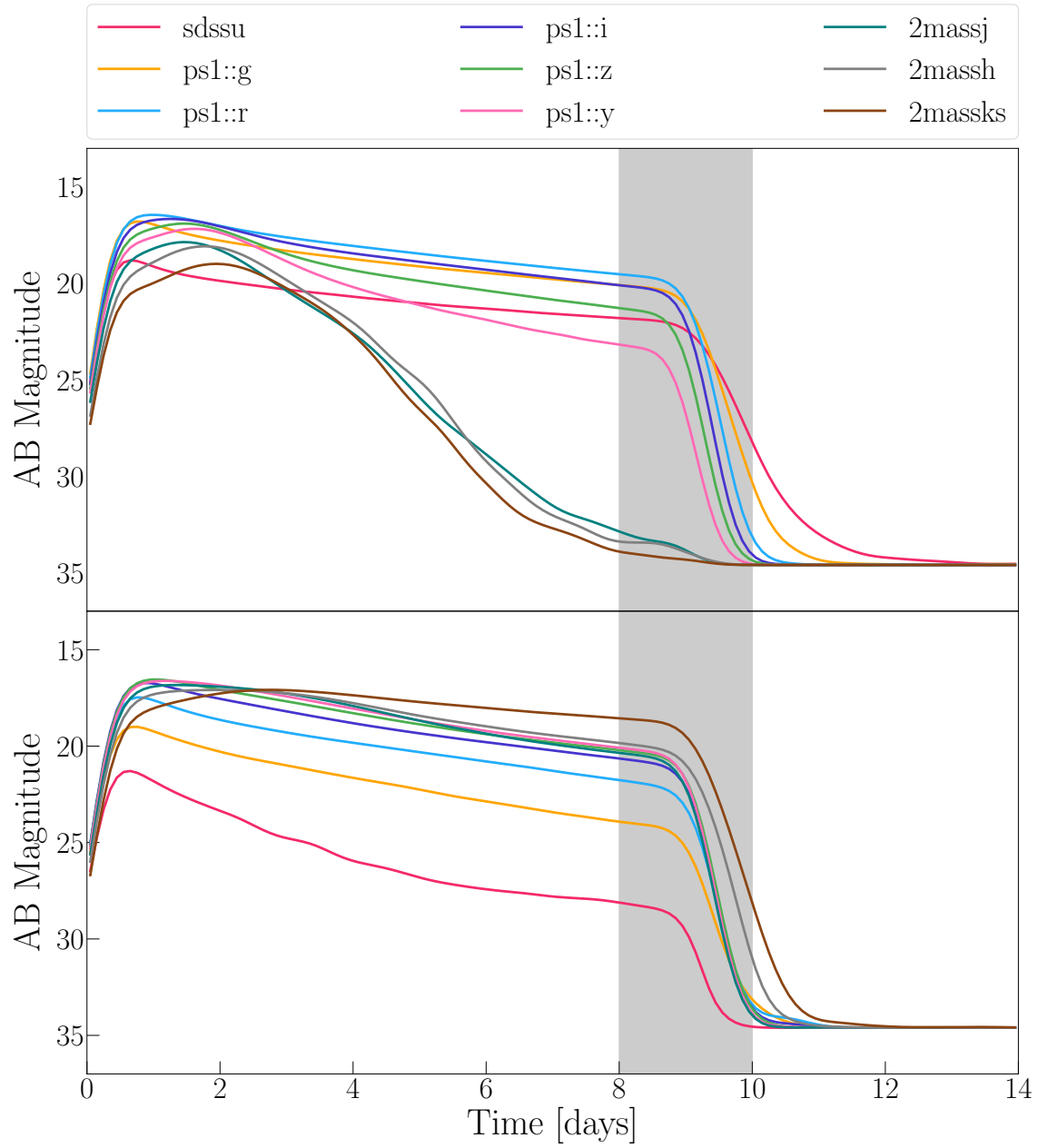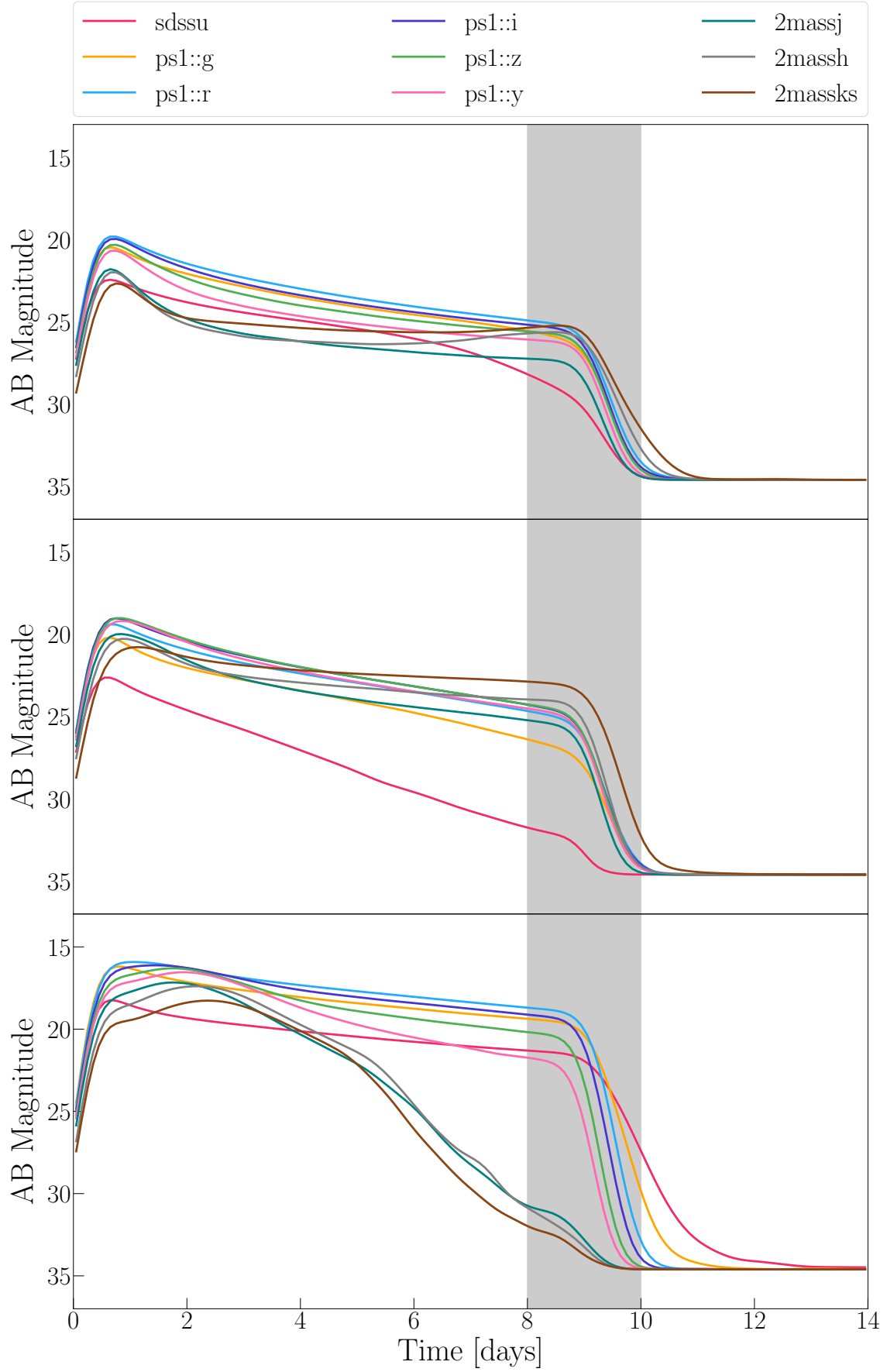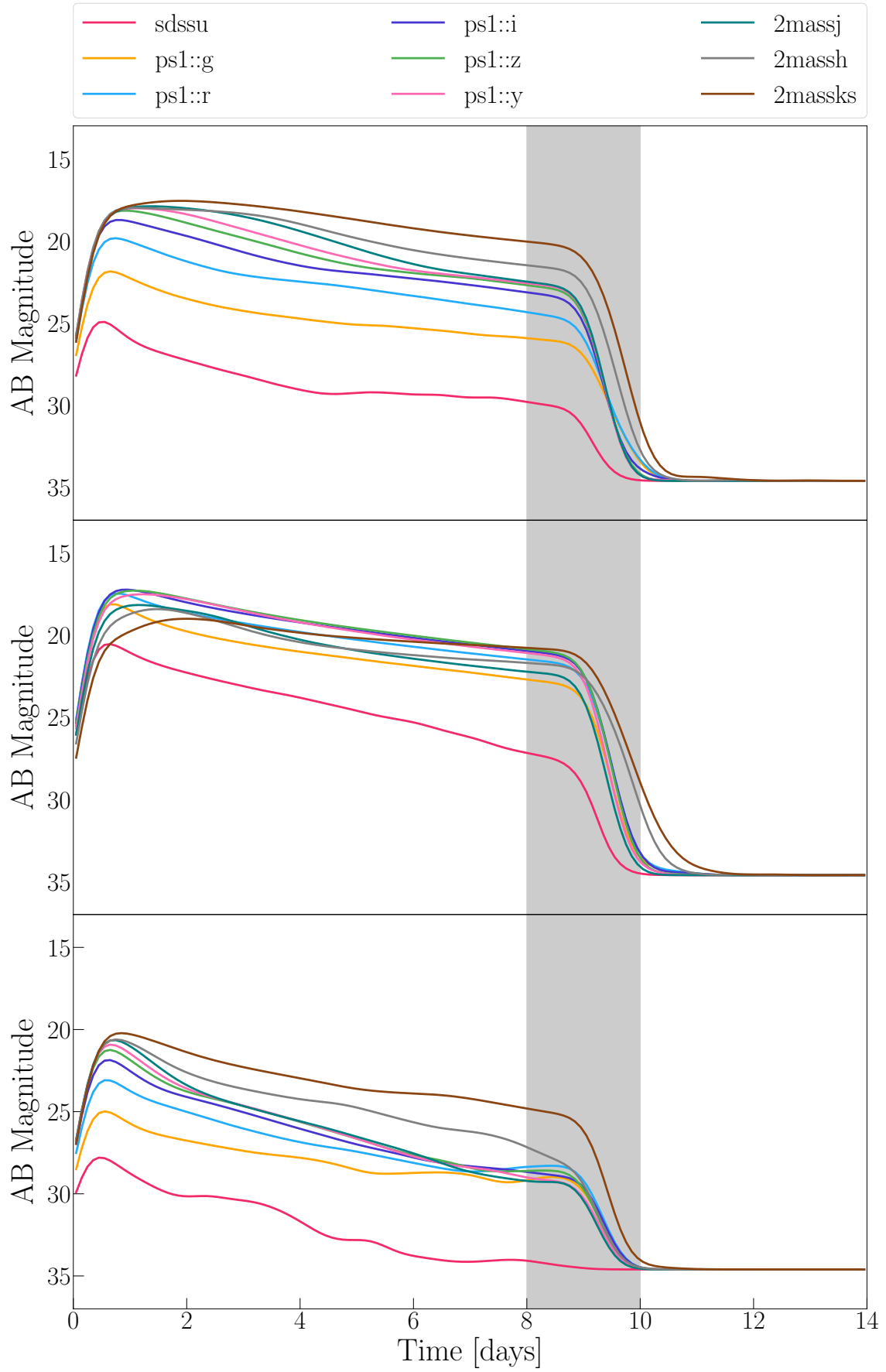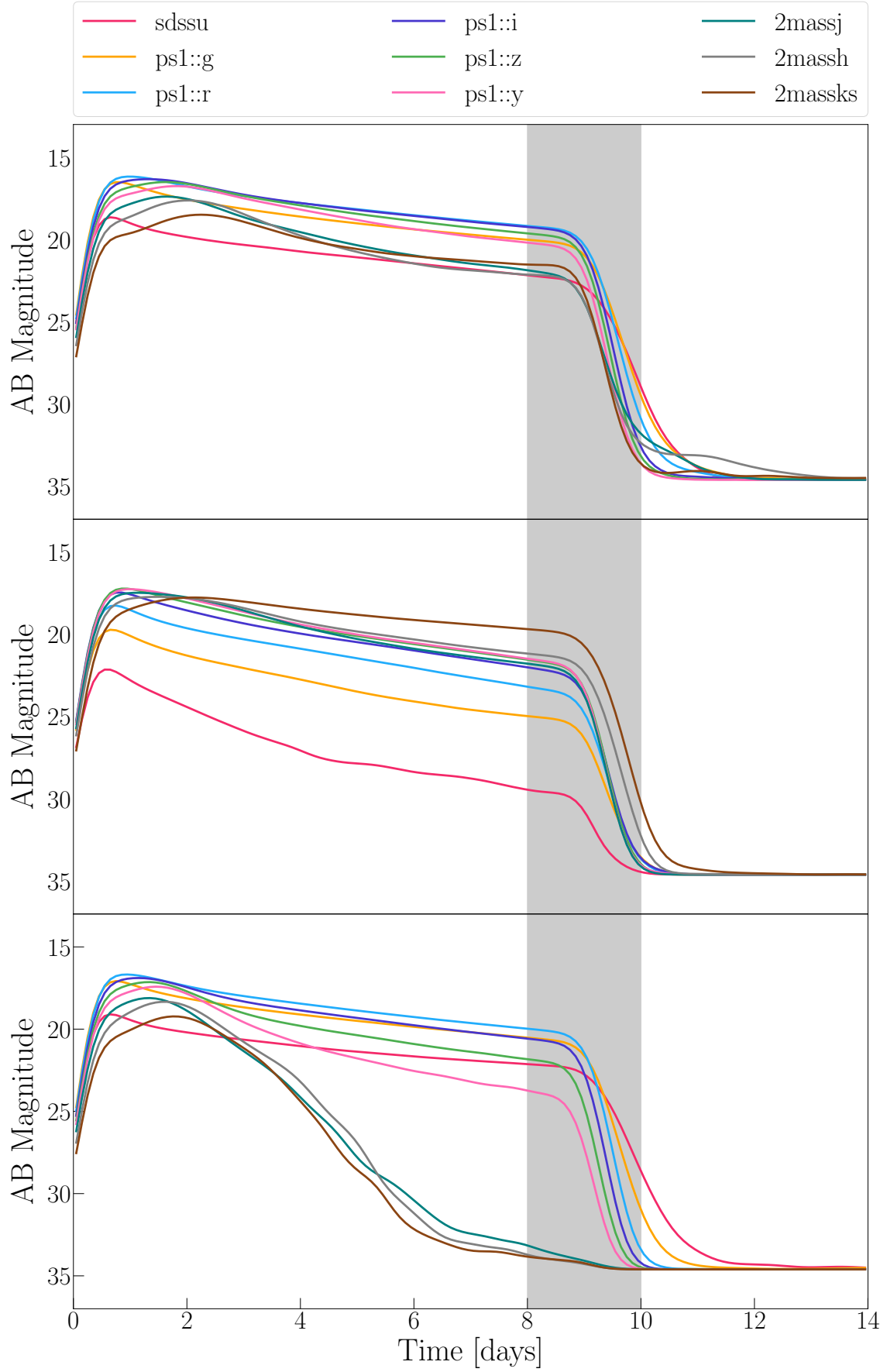
Figure C.1

Code and Documentation

D.1 Code

D.1.1 Parsing systematics from `.yaml` file

```python
import inspect
import warnings
from pathlib import Path

import yaml
from bilby.core.prior import analytical

warnings.simplefilter("module", DeprecationWarning)


class ValidationError(ValueError):
    def __init__(self, key, message):
        super().__init__(f"Validation error for '{key}': {message}")


ALLOWED_FILTERS = [
    "2massh",
    "2massj",
    "2massks",
    "atlasc",
    "atlaso",
    "bessellb",
    "besselli",
    "bessellr",
    "bessellux",
    "bessellv",
    "ps1__g",
    "ps1__i",
    "ps1__r",
    "ps1__y",
    "ps1__z",
    "sdssu",
    "uvot__b",
    "uvot__u",
    "uvot__uvm2",
    "uvot__uvw1",
    "uvot__uvw2",
```

```python
    "uvot__v",
    "uvot__white",
    "ztfg",
    "ztfi",
    "ztfr",
]


ALLOWED_DISTRIBUTIONS = dict(inspect.getmembers(analytical,
    inspect.isclass))


def get_positional_args(cls):
    init_method = cls.__init__

    signature = inspect.signature(init_method)
    params = [
        param.name
        for param in signature.parameters.values()
        if param.name != "self" and param.default ==
            inspect.Parameter.empty
    ]

    return params


DISTRIBUTION_PARAMETERS = {k: get_positional_args(v) for k, v in
    ALLOWED_DISTRIBUTIONS.items()}


def load_yaml(file_path):
    return yaml.safe_load(Path(file_path).read_text())


def validate_only_one_true(yaml_dict):
    for key, values in yaml_dict["config"].items():
        if "value" not in values or not isinstance(values["value"],
            bool):
            raise ValidationError(key, "'value' key must be present
                and be a boolean")
    true_count = sum(value["value"] for value in
        yaml_dict["config"].values())
    if true_count > 1:
        raise ValidationError("config", "Only one configuration key
            can be set to True at a time")
```

```python
    elif true_count == 0:
        raise ValidationError("config", "At least one configuration
            key must be set to True")


def validate_filters(filter_groups):
    used_filters = set()
    for filter_group in filter_groups:
        if isinstance(filter_group, list):
            filters_in_group = set()  # Keep track of filters within this group
            for filt in filter_group:
                if filt not in ALLOWED_FILTERS:
                    raise ValidationError(
                        "filters",
                        f"Invalid filter value '{filt}'. Allowed
                            values are {', '.join([str(f) for f in
                            ALLOWED_FILTERS])}",
                    )
                if filt in filters_in_group:
                    raise ValidationError(
                        "filters",
                        f"Duplicate filter value '{filt}' within the
                            same group.",
                    )
                if filt in used_filters:
                    raise ValidationError(
                        "filters",
                        f"Duplicate filter value '{filt}'. A filter
                            can only be used in one group.",
                    )
                used_filters.add(filt)
                filters_in_group.add(filt)
                # Add the filter to the set of used filters within this group
        elif filter_group is not None and filter_group not in
            ALLOWED_FILTERS:
            raise ValidationError(
                "filters",
                f"Invalid filter value '{filter_group}'. Allowed
                    values are {', '.join([str(f) for f in
                    ALLOWED_FILTERS])}",
            )
        elif filter_group in used_filters:
            raise ValidationError(
                "filters",
```

```python
                    f"Duplicate filter value '{filter_group}'. A filter
                        can only be used in one group.",
                )
            else:
                used_filters.add(filter_group)


def validate_distribution(distribution):
    dist_type = distribution.get("type")
    if dist_type not in ALLOWED_DISTRIBUTIONS:
        raise ValidationError(
            "distribution type",
            f"Invalid distribution '{dist_type}'. Allowed values are
                {', '.join([str(f) for f in ALLOWED_DISTRIBUTIONS])}",
        )

    required_params = DISTRIBUTION_PARAMETERS[dist_type]

    missing_params = set(required_params)  set(distribution.keys())
    if missing_params:
        raise ValidationError(
            "distribution", f"Missing required parameters for
                {dist_type} distribution: {', '.join(missing_params)}"
        )


def create_prior_string(name, distribution):
    dist_type = distribution.pop("type")
    _ = distribution.pop("value", None)
    _ = distribution.pop("time_nodes", None)
    _ = distribution.pop("filters", None)
    prior_class = ALLOWED_DISTRIBUTIONS[dist_type]
    required_params = DISTRIBUTION_PARAMETERS[dist_type]
    params = distribution.copy()

    extra_params = set(params.keys())  set(required_params)
    if extra_params:
        warnings.warn(f"Distribution parameters {extra_params} are
            not used by {dist_type} distribution and will be ignored")

    params = {k: params[k] for k in required_params if k in params}

    return f"{name} = {repr(prior_class(**params, name=name))}"
```

```python
def handle_withTime(values):
    validate_distribution(values)
    filter_groups = values.get("filters", [])
    validate_filters(filter_groups)
    result = []
    time_nodes = values["time_nodes"]

    for filter_group in filter_groups:
        if isinstance(filter_group, list):
            filter_name = "___".join(filter_group)
        else:
            filter_name = filter_group if filter_group is not None
                else "all"

        for n in range(1, time_nodes + 1):
            prior_name = f"sys_err_{filter_name}{n}"
            result.append(create_prior_string(prior_name,
                values.copy()))

    return result


def handle_withoutTime(values):
    validate_distribution(values)
    return [create_prior_string("sys_err", values)]


config_handlers = {
    "withTime": handle_withTime,
    "withoutTime": handle_withoutTime,
}


def main(yaml_file_path):
    yaml_dict = load_yaml(yaml_file_path)
    validate_only_one_true(yaml_dict)
    results = []
    for key, values in yaml_dict["config"].items():
        if values["value"] and key in config_handlers:
            results.extend(config_handlers[key](values))
    return results
```

D.1.2 Injecting systematic configuration into `PriorDict`

```python
from bilby.core.prior import PriorDict as _PriorDict
from . import systematics

def from_list(self, systematics):
    """
    Similar to 'from_file' but instead of file buffer, takes a list
        of Prior strings
    See 'from_file' for more details
    """

    comments = ["#", "\n"]
    prior = dict()
    for line in systematics:
        if line[0] in comments:
            continue
        line.replace(" ", "")
        elements = line.split("=")
        key = elements[0].replace(" ", "")
        val = "=".join(elements[1:]).strip()
        prior[key] = val
    self.from_dictionary(prior)

setattr(_PriorDict, "from_list", from_list)

class ConditionalGaussianIotaGivenThetaCore
            (ConditionalTruncatedGaussian):
    ...
    ...
    ...
def create_prior_from_args(model_names, args):
    AnBa2022_intersect = list(set(['AnBa2022_linear',
        'AnBa2022_log']) & set(model_names))

    if len(AnBa2022_intersect) > 0:
        ...
        ...
        ...
    else:
        priors = bilby.gw.prior.PriorDict(args.prior)

    if args.systematics_file is not None:
            systematics_priors =
                systematics.main(args.systematics_file)
            priors.from_list(systematics_priors)
```

```python
    return priors
```

D.1.3 Likelihood Calculation

```python
from __future__ import division

import numpy as np
import scipy.stats
from scipy.interpolate import interp1d
from scipy.stats import truncnorm
from pathlib import Path
import yaml


from . import utils, systematics


class OpticalLightCurve(Likelihood):
    ...
    ...
    ...
        self.systematics_file = systematics_file
    ...
    ...
    ...
    def log_likelihood(self):
        lbol, mag_abs = self.light_curve_model.generate_lightcurve(
            self.sample_times, self.parameters
        )
        ...
        ...
        ...
        if self.systematics_file is not None:
            yaml_dict = yaml.safe_load(
                Path(self.systematics_file).read_text())
            systematics.validate_only_one_true(yaml_dict)

            if yaml_dict["config"]["withTime"]["value"]:
                n = yaml_dict["config"]["withTime"]
                ["time_nodes"]
                time_array = np.round(np.linspace(self.tmin,
                    self.tmax, n), 2)
                yaml_filters = yaml_dict["config"]["withTime"]
                ["filters"]
                systematics.validate_filters(
                    yaml_filters)
```

```python
            for filter_group in yaml_filters:
                if isinstance(filter_group, list):
                    filt = "___".join(filter_group)
                elif filter_group is None:
                    filt = "all"
                else:
                    filt = filter_group

                globals()[f"sys_err_{filt}_array"] = np.array([])

                for i in range(1, n + 1):
                    value = self.parameters.get(f"sys_err_
                    {filt}{i}")
                    globals()[f"sys_err_{filt}_array"] =
                        np.append(globals()[f"sys_err_
                    {filt}_array"], value)

            for filter_group in yaml_dict["config"]["withTime"]
            ["filters"]:
                if isinstance(filter_group, list):
                    filt = "___".join(filter_group)
                elif filter_group is None:
                    filt = "all"
                else:
                    filt = filter_group
                globals()[f"sys_err_{filt}_interped"] =
                    interp1d(time_array,
                    globals()[f"sys_err_{filt}_array"],
                    fill_value="extrapolate", bounds_error=False)


    # compare the estimated light curve and the measured data
    minus_chisquare_total = 0.0
    gaussprob_total = 0.0
    for filt in self.filters:
        # decompose the data
        data_time = self.light_curve_data[filt][:, 0]
        data_mag = self.light_curve_data[filt][:, 1]
        data_sigma = self.light_curve_data[filt][:, 2]

        if self.systematics_file is not None:
            if yaml_dict["config"]["withTime"]
            ["value"]:
                yaml_filters = yaml_dict["config"]["withTime"]
```

```python
            ["filters"]

            filter_group_finite_idx_match = False

            if yaml_filters is not None and yaml_filters != []:
                for yaml_filt in yaml_filters:
                    if yaml_filt is not None and filt in
                        yaml_filt:
                        if isinstance(yaml_filt, str):
                            filters_to_use = yaml_filt
                        elif isinstance(yaml_filt, list):
                            filters_to_use = "___".join(
                                yaml_filt)
                        filter_group_finite_idx
                        _match = True
                        break
            if not filter_group_finite_idx_match:
                filters_to_use = "all"
            data_sigma = np.sqrt(data_sigma**2 +
                (globals()[f"sys_err_{filters_
            to_use}_interped"](data_time)) ** 2)

        elif yaml_dict["config"]["withoutTime"]
        ["value"]:
            data_sigma = np.sqrt(data_sigma**2 +
                self.parameters["sys_err"] ** 2)

    # include the error budget into calculation
    elif 'sys_err' in self.parameters:
        data_sigma = np.sqrt(data_sigma**2 +
            self.parameters['sys_err']**2)
    else:
        data_sigma = np.sqrt(data_sigma**2 +
            self.error_budget[filt]**2)

    # evaluate the light curve magnitude at the data points
    mag_est = mag_app_interp[filt](data_time)

    # seperate the data into bounds (inf err) and actual measurement
    infIdx = np.where(~np.isfinite(data_sigma))[0]
    finiteIdx = np.where(np.isfinite(data_sigma))[0]
    ...
    ...
    ...
```

```python
        if len(infIdx) > 0:
            if self.systematics_file is not None:
                if yaml_dict["config"]["withTime"]
                ["value"]:
                    yaml_filters = yaml_dict["config"]["withTime"]
                    ["filters"]

                    filter_group_infinite_idx_match = False

                    if yaml_filters is not None and yaml_filters
                        != []:
                        for yaml_filt in yaml_filters:
                            if yaml_filt is not None and filt in
                                yaml_filt:
                                if isinstance(yaml_
                                filt, str):
                                    upperlim_sigma = globals()[f"sys
                                    _err_{yaml_filt}_
                                    interped"]
                                    (data_time)
                                    [infIdx]
                                elif isinstance(yaml_
                                filt, list):
                                    filters_to_use = "___".join(yaml
                                    _filt)
                                    upperlim_sigma = globals()[f"sys
                                    _err_{filters_to_
                                    use}_interped"]
                                    (data_time)
                                    [infIdx]
                                filter_group_infinite
                                _idx_match = True
                                break
                    if not filter_group_infinite_idx
                    _match:
                        filters_to_use = "all"
                        upperlim_sigma = globals()[f"sys_err_
                        {filters_to_use}_interped"]
                        (data_time)[infIdx]

                    gausslogsf = scipy.stats.norm.logsf(
                        data_mag[infIdx], mag_est[infIdx],
                            upperlim_sigma)
```

```
            elif yaml_dict["config"]["withoutTime"]
            ["value"]:
                upperlim_sigma = self.parameters["sys_err"]
                gausslogsf = scipy.stats.norm.logsf(
                    data_mag[infIdx], mag_est[infIdx],
                        upperlim_sigma)
        elif 'sys_err' in self.parameters:
            upperlim_sigma = self.parameters['sys_err']
            gausslogsf = scipy.stats.norm.logsf(data_mag
            [infIdx], mag_est[infIdx], upperlim_sigma)
        else:
            ...
            ...
            ...


    return log_prob
```

D.2   Documentation

NMMA currently uses `--error-budget` to specify the constant systematic uncertainties to be added to the likelihood quadrature.

However, it is now possible to use systematic error (σ_{sys}) prior in form of a freely sampled parameter, time dependent and/or filter dependent systematic error. This can done by specifying the file path using the `--systematics-file` flag in `lightcurve-analysis` command.

For more information on systematics error, refer to the main text or Ref. [1].

D.2.1   Freely Sampled Systematic Uncertainty

In this case the systematic error is freely sampled and is not dependent on time or filter.

```
config:
    withTime:
        value: false
        filters:
            null
        time_nodes: 4
        type: Uniform
        minimum: 0
        maximum: 2
    withoutTime:
        value: true
        type: Uniform
        minimum: 0
        maximum: 2
```

D.2.2 Time Dependent Systematic Uncertainty

In this configuration, a time dependent single systematic error is applied across all filters.

```
config:
    withTime:
        value: true
        filters:
            null
        time_nodes: 4
        type: Uniform
        minimum: 0
        maximum: 2
    withoutTime:
        value: false
        type: Uniform
        minimum: 0
        maximum: 2
```

D.2.3 Time and Filter Dependent Systematic Uncertainty

In this configuration, the `sdssu` and `ztfr` filters are sampled together for systematic errors, while the `2massks` filter is sampled independently. All other filters are grouped and sampled together.

```yaml
config:
    withTime:
        value: true
        filters:
            [sdssu, ztfr]
            [2massks]
            null
        time_nodes: 4
        type: Uniform
        minimum: 0
        maximum: 2
    withoutTime:
        value: false
        type: Uniform
        minimum: 0
        maximum: 2
```

D.2.4 Distribution types

Distribution can be of any of the `analytical` prior from `bilby`. Refer to `bilby` documentation for more information on the available distribution type and their usage. Only positional arguments are required for any of the distrbutions.

References

Back-references to the pages where the publication was cited are given by ⬤.

[1] Sahil Jhawar, Thibeau Wouters, Peter T. H. Pang, Mattia Bulla, Michael W. Coughlin, and Tim Dietrich. Data-driven approach for modeling the temporal and spectral evolution of kilonova systematic uncertainties. *Phys. Rev. D*, 4 **2025**.
DOI: 10.1103/PhysRevD.111.043046 ARXIV: 2410.21978 [astro-ph.HE]
vii, 3, 85

[2] Malina Desai, Deep Chatterjee, Sahil Jhawar, Philip Harris, Erik Katsavounidis, and Michael Coughlin. Kilonova Light Curve Parameter Estimation Using Likelihood-Free Inference. **2024**.
ARXIV: 2408.06947 [astro-ph.IM] URL: https://arxiv.org/abs/2408.06947
vii

[3] T. Hussenot-Desenonges et al. Multiband analyses of the bright GRB 230812B and the associated SN2023pel. *Mon. Not. Roy. Astron. Soc.*, **2024**.
DOI: 10.1093/mnras/stae503 ARXIV: 2310.14310 [astro-ph.HE] vii, 37, 38

[4] B. P. Abbott et al. GW170817: Observation of Gravitational Waves from a Binary Neutron Star Inspiral. *Phys. Rev. Lett.*, **2017**.
DOI: 10.1103/PhysRevLett.119.161101 ARXIV: 1710.05832 [gr-qc] 1

[5] B. P. Abbott et al. Multi-messenger Observations of a Binary Neutron Star Merger. *Astrophys. J. Lett.*, **2017**.
DOI: 10.3847/2041-8213/aa91c9 ARXIV: 1710.05833 [astro-ph.HE] 1

[6] J. Aasi et al. Advanced LIGO. *Class. Quant. Grav.*, **2015**.
DOI: 10.1088/0264-9381/32/7/074001 ARXIV: 1411.4547 [gr-qc] 1

[7] F. Acernese et al. Advanced Virgo: a second-generation interferometric gravitational wave detector. *Class. Quant. Grav.*, **2015**.
DOI: 10.1088/0264-9381/32/2/024001 ARXIV: 1408.3978 [gr-qc] 1

[8] A. Goldstein et al. An Ordinary Short Gamma-Ray Burst with Extraordinary Implications: Fermi-GBM Detection of GRB 170817A. *The Astrophysical Journal Letters*, **2017**.
DOI: 10.3847/2041-8213/aa8f41 ARXIV: 1710.05446 [astro-ph.HE] 1

[9] V. Savchenko et al. INTEGRAL Detection of the First Prompt Gamma-Ray Signal Coincident with the Gravitational-wave Event GW170817. *The Astrophysical Journal Letters*, **2017**.
DOI: 10.3847/2041-8213/aa8f94 ARXIV: 1710.05449 [astro-ph.HE] 1

[10] D. A. Coulter et al. Swope Supernova Survey 2017a (SSS17a), the optical counterpart to a gravitational wave source. *Science*, **2017**.
DOI: 10.1126/science.aap9811   ARXIV: 1710.05452 [astro-ph.HE]   1, 7

[11] Albino Perego, David Radice, and Sebastiano Bernuzzi. AT 2017gfo: An Anisotropic and Three-component Kilonova Counterpart of GW170817. *Astrophys. J. Lett.*, **2017**.
DOI: 10.3847/2041-8213/aa9ab9   ARXIV: 1711.03982 [astro-ph.HE]
1, 2, 7, 10, 11

[12] B. P. Abbott et al. A gravitational-wave standard siren measurement of the Hubble constant. *Nature*, **2017**.
DOI: 10.1038/nature24471   ARXIV: 1710.05835 [astro-ph.CO]   1

[13] C. Guidorzi et al. Improved Constraints on H_0 from a Combined Analysis of Gravitational-wave and Electromagnetic Emission from GW170817. *Astrophys. J. Lett.*, **2017**.
DOI: 10.3847/2041-8213/aaa009   ARXIV: 1710.06426 [astro-ph.CO]   1

[14] Kenta Hotokezaka, Ehud Nakar, Ore Gottlieb, Samaya Nissanke, Kento Masuda, Gregg Hallinan, Kunal P. Mooley, and Adam. T. Deller. A Hubble constant measurement from superluminal motion of the jet in GW170817. *Nature Astron.*, **2019**.
DOI: 10.1038/s41550-019-0820-1   ARXIV: 1806.10596 [astro-ph.CO]   1

[15] Ehud Nakar and Tsvi Piran. Afterglow constraints on the viewing angle of binary neutron star mergers and determination of the Hubble constant. *Astrophys. J.*, **2021**.
DOI: 10.3847/1538-4357/abd6cd   ARXIV: 2005.01754 [astro-ph.HE]   1

[16] Michael W. Coughlin, Tim Dietrich, Jack Heinzel, Nandita Khetan, Sarah Antier, Mattia Bulla, Nelson Christensen, David A. Coulter, and Ryan J. Foley. Standardizing kilonovae and their use as standard candles to measure the Hubble constant. *Phys. Rev. Res.*, **2020**.
DOI: 10.1103/PhysRevResearch.2.022006   ARXIV: 1908.00889 [astro-ph.HE]   1

[17] Rahul Kashyap, Gayathri Raman, and Parameswaran Ajith. Can Kilonova Light curves be Standardized? *Astrophys. J. Lett.*, **2019**.
DOI: 10.3847/2041-8213/ab543f   ARXIV: 1908.02168 [astro-ph.SR]   1

[18] Michael W. Coughlin, Sarah Antier, Tim Dietrich, Ryan J. Foley, Jack Heinzel, Mattia Bulla, Nelson Christensen, David A. Coulter, Lina Issa, and Nandita Khetan. Measuring the Hubble Constant with a sample of kilonovae. *Nature Commun.*, **2020**.
DOI: 10.1038/s41467-020-17998-5   ARXIV: 2008.07420 [astro-ph.HE]   1

[19] Tim Dietrich, Michael W. Coughlin, Peter T. H. Pang, Mattia Bulla, Jack

Heinzel, Lina Issa, Ingo Tews, and Sarah Antier. Multimessenger constraints on the neutron-star equation of state and the Hubble constant. *Science*, **2020**. DOI: 10.1126/science.abb4317 ARXIV: 2002.11355 [astro-ph.HE] [1], [37], [42]

[20] Mattia Bulla, Michael W. Coughlin, Suhail Dhawan, and Tim Dietrich. Multi-Messenger Constraints on the Hubble Constant through Combination of Gravitational Waves, Gamma-Ray Bursts and Kilonovae from Neutron Star Mergers. *Universe*, **2022**. DOI: 10.3390/universe8050289 ARXIV: 2205.09145 [astro-ph.HE] [1]

[21] Giulia Gianfagna, Luigi Piro, Francesco Pannarale, Hendrik Van Eerten, Fulvio Ricci, Geoffrey Ryan, and Eleonora Troja. Joint analysis of gravitational-wave and electromagnetic data of mergers: breaking an afterglow model degeneracy in GW170817 and in future events. *Mon. Not. Roy. Astron. Soc.*, **2023**. DOI: 10.1093/mnras/stad1728 ARXIV: 2212.01104 [astro-ph.HE] [1]

[22] Eemeli Annala, Tyler Gorda, Aleksi Kurkela, and Aleksi Vuorinen. Gravitational-wave constraints on the neutron-star-matter Equation of State. *Phys. Rev. Lett.*, **2018**. DOI: 10.1103/PhysRevLett.120.172703 ARXIV: 1711.02644 [astro-ph.HE] [1]

[23] Andreas Bauswein, Oliver Just, Hans-Thomas Janka, and Nikolaos Stergioulas. Neutron-star radius constraints from GW170817 and future detections. *Astrophys. J. Lett.*, **2017**. DOI: 10.3847/2041-8213/aa9994 ARXIV: 1710.06843 [astro-ph.HE] [1]

[24] F. J. Fattoyev, J. Piekarewicz, and C. J. Horowitz. Neutron Skins and Neutron Stars in the Multimessenger Era. *Phys. Rev. Lett.*, **2018**. DOI: 10.1103/PhysRevLett.120.172702 ARXIV: 1711.06615 [nucl-th] [1]

[25] Collin D. Capano, Ingo Tews, Stephanie M. Brown, Ben Margalit, Soumi De, Sumit Kumar, Duncan A. Brown, Badri Krishnan, and Sanjay Reddy. Stringent constraints on neutron-star radii from multimessenger observations and nuclear theory. *Nature Astron.*, **2020**. DOI: 10.1038/s41550-020-1014-6 ARXIV: 1908.10352 [astro-ph.HE] [1]

[26] B. P. Abbott et al. Properties of the binary neutron star merger GW170817. *Phys. Rev. X*, **2019**. DOI: 10.1103/PhysRevX.9.011001 ARXIV: 1805.11579 [gr-qc] [1]

[27] B. P. Abbott et al. GW170817: Measurements of neutron star radii and equation of state. *Phys. Rev. Lett.*, **2018**. DOI: 10.1103/PhysRevLett.121.161101 ARXIV: 1805.11581 [gr-qc] [1], [6]

[28] S. Huth et al. Constraining Neutron-Star Matter with Microscopic and Macroscopic Collisions. *Nature*, **2022**. DOI: 10.1038/s41586-022-04750-w ARXIV: 2107.06229 [nucl-th] [1]

[29] Jose María Ezquiaga and Miguel Zumalacárregui. Dark Energy After GW170817: Dead Ends and the Road Ahead. *Phys. Rev. Lett.*, **2017**.
DOI: `10.1103/PhysRevLett.119.251304` ARXIV: `1710.05901 [astro-ph.CO]` [1]

[30] T. Baker, E. Bellini, P. G. Ferreira, M. Lagos, J. Noller, and I. Sawicki. Strong constraints on cosmological gravity from GW170817 and GRB 170817A. *Phys. Rev. Lett.*, **2017**.
DOI: `10.1103/PhysRevLett.119.251301` ARXIV: `1710.06394 [astro-ph.CO]` [1]

[31] Paolo Creminelli and Filippo Vernizzi. Dark Energy after GW170817 and GRB170817A. *Phys. Rev. Lett.*, **2017**.
DOI: `10.1103/PhysRevLett.119.251302` ARXIV: `1710.05877 [astro-ph.CO]` [1]

[32] P. S. Cowperthwaite et al. The Electromagnetic Counterpart of the Binary Neutron Star Merger LIGO/Virgo GW170817. II. UV, Optical, and Near-infrared Light Curves and Comparison to Kilonova Models. *Astrophys. J. Lett.*, **2017**.
DOI: `10.3847/2041-8213/aa8fc7` ARXIV: `1710.05840 [astro-ph.HE]` [1]

[33] S. J. Smartt et al. A kilonova as the electromagnetic counterpart to a gravitational-wave source. *Nature*, **2017**.
DOI: `10.1038/nature24303` ARXIV: `1710.05841 [astro-ph.HE]` [1]

[34] M. M. Kasliwal et al. Illuminating Gravitational Waves: A Concordant Picture of Photons from a Neutron Star Merger. *Science*, **2017**.
DOI: `10.1126/science.aap9455` ARXIV: `1710.05436 [astro-ph.HE]` [1]

[35] Daniel Kasen, Brian Metzger, Jennifer Barnes, Eliot Quataert, and Enrico Ramirez-Ruiz. Origin of the heavy elements in binary neutron-star mergers from a gravitational wave event. *Nature*, **2017**.
DOI: `10.1038/nature24453` ARXIV: `1710.05463 [astro-ph.HE]` [1], [10], [15], [18]

[36] Darach Watson et al. Identification of strontium in the merger of two neutron stars. *Nature*, **2019**.
DOI: `10.1038/s41586-019-1676-3` ARXIV: `1910.10510 [astro-ph.HE]` [1], [10]

[37] S. Rosswog, J. Sollerman, U. Feindt, A. Goobar, O. Korobkin, R. Wollaeger, C. Fremling, and M. M. Kasliwal. The first direct double neutron star merger detection: implications for cosmic nucleosynthesis. *Astron. Astrophys.*, **2018**.
DOI: `10.1051/0004-6361/201732117` ARXIV: `1710.05445 [astro-ph.HE]` [1], [2]

[38] B. P. Abbott et al. GW190425: Observation of a Compact Binary Coalescence with Total Mass $\sim 3.4 M_\odot$. *Astrophys. J. Lett.*, **2020**.
DOI: `10.3847/2041-8213/ab75f5` ARXIV: `2001.01761 [astro-ph.HE]` [1]

[39] Jillian C. Rastinejad et al. A kilonova following a long-duration gamma-ray burst at 350 Mpc. *Nature*, **2022**.
DOI: `10.1038/s41586-022-05390-w` ARXIV: `2204.10864 [astro-ph.HE]` [1]

[40] Geoffrey Ryan, Hendrik van Eerten, Luigi Piro, and Eleonora Troja. Gamma-

Ray Burst Afterglows in the Multimessenger Era: Numerical Models and Closure Relations. *Astrophys. J.*, **2020**.
DOI: `10.3847/1538-4357/ab93cf`   ARXIV: `1909.11691 [astro-ph.HE]`   [1]

[41] N. Kunert et al. Bayesian model selection for GRB 211211A through multiwavelength analyses. *Mon. Not. Roy. Astron. Soc.*, **2024**.
DOI: `10.1093/mnras/stad3463`   ARXIV: `2301.02049 [astro-ph.HE]`   [1], [37]

[42] Andrew J. Levan et al. Heavy-element production in a compact object merger observed by JWST. *Nature*, **2024**.
DOI: `10.1038/s41586-023-06759-1`   ARXIV: `2307.02098 [astro-ph.HE]`   [1]

[43] Anuradha Samajdar and Tim Dietrich. Waveform systematics for binary neutron star gravitational wave signals: effects of the point-particle baseline and tidal descriptions. *Phys. Rev. D*, **2018**.
DOI: `10.1103/PhysRevD.98.124030`   ARXIV: `1810.03936 [gr-qc]`   [2]

[44] Anuradha Samajdar and Tim Dietrich. Waveform systematics for binary neutron star gravitational wave signals: Effects of spin, precession, and the observation of electromagnetic counterparts. *Phys. Rev. D*, **2019**.
DOI: `10.1103/PhysRevD.100.024046`   ARXIV: `1905.03118 [gr-qc]`   [2]

[45] Rossella Gamba, Matteo Breschi, Sebastiano Bernuzzi, Michalis Agathos, and Alessandro Nagar. Waveform systematics in the gravitational-wave inference of tidal parameters and equation of state from binary neutron star signals. *Phys. Rev. D*, **2021**.
DOI: `10.1103/PhysRevD.103.124015`   ARXIV: `2009.08467 [gr-qc]`   [2]

[46] Nina Kunert, Peter T. H. Pang, Ingo Tews, Michael W. Coughlin, and Tim Dietrich. Quantifying modeling uncertainties when combining multiple gravitational-wave detections from binary neutron star sources. *Phys. Rev. D*, **2022**.
DOI: `10.1103/PhysRevD.105.L061301`   ARXIV: `2110.11835 [astro-ph.HE]`   [2]

[47] Anjali B. Yelikar, Richard O'Shaughnessy, Daniel Wysocki, and Leslie Wade. Effects of waveform systematics on inferences of neutron star population properties and the nuclear equation of state, **2024**.
ARXIV: `2410.14674 [gr-qc]`   [2]

[48] M. Punturo et al. The Einstein Telescope: A third-generation gravitational wave observatory. *Class. Quant. Grav.*, **2010**. Ed. by Fulvio Ricci.
DOI: `10.1088/0264-9381/27/19/194002`   [2]

[49] B. Sathyaprakash et al. Scientific Objectives of Einstein Telescope. *Class. Quant. Grav.*, **2012**. Ed. by Mark Hannam, Patrick Sutton, Stefan Hild, and Chris van den Broeck. [Erratum: Class.Quant.Grav. 30, 079501 (2013)].
DOI: `10.1088/0264-9381/29/12/124013`   ARXIV: `1206.0331 [gr-qc]`   [2]

[50] Marica Branchesi et al. Science with the Einstein Telescope: a comparison of different designs. *JCAP*, **2023**.
DOI: `10.1088/1475-7516/2023/07/068` ARXIV: `2303.15923 [gr-qc]` `2`

[51] Varun Srivastava, Derek Davis, Kevin Kuns, Philippe Landry, Stefan Ballmer, Matthew Evans, Evan D. Hall, Jocelyn Read, and B. S. Sathyaprakash. Science-driven Tunable Design of Cosmic Explorer Detectors. *Astrophys. J.*, **2022**.
DOI: `10.3847/1538-4357/ac5f04` ARXIV: `2201.10668 [gr-qc]` `2`

[52] Li-Xin Li and Bohdan Paczynski. Transient events from neutron star mergers. *Astrophys. J. Lett.*, **1998**.
DOI: `10.1086/311680` ARXIV: `astro-ph/9807272` `2`, `6`, `7`

[53] Brian D. Metzger. Kilonovae. *Living Rev. Rel.*, **2020**.
DOI: `10.1007/s41114-019-0024-0` ARXIV: `1910.01617 [astro-ph.HE]`
`2`, `8`, `10`, `11`, `12`

[54] Doron Grossman, Oleg Korobkin, Stephan Rosswog, and Tsvi Piran. The long-term evolution of neutron star merger remnants – II. Radioactively powered transients. *Mon. Not. Roy. Astron. Soc.*, **2014**.
DOI: `10.1093/mnras/stt2503` ARXIV: `1307.2943 [astro-ph.HE]` `2`

[55] V. Ashley Villar et al. The Combined Ultraviolet, Optical, and Near-Infrared Light Curves of the Kilonova Associated with the Binary Neutron Star Merger GW170817: Unified Data Set, Analytic Models, and Physical Implications. *Astrophys. J. Lett.*, **2017**.
DOI: `10.3847/2041-8213/aa9c84` ARXIV: `1710.11576 [astro-ph.HE]` `2`

[56] C. Barbieri, O. S. Salafia, A. Perego, M. Colpi, and G. Ghirlanda. Electromagnetic counterparts of black hole-neutron star mergers: dependence on the neutron star properties. *Eur. Phys. J. A*, **2020**.
DOI: `10.1140/epja/s10050-019-00013-x` ARXIV: `1908.08822 [astro-ph.HE]` `2`

[57] Kenta Hotokezaka and Ehud Nakar. Radioactive heating rate of r-process elements and macronova light curve, **2019**.
DOI: `10.3847/1538-4357/ab6a98` ARXIV: `1909.02581 [astro-ph.HE]` `2`

[58] Jin-Ping Zhu, Yuan-Pei Yang, Liang-Duan Liu, Yan Huang, Bing Zhang, Zhuo Li, Yun-Wei Yu, and He Gao. Kilonova Emission from Black Hole–Neutron Star Mergers. I. Viewing-angle-dependent Lightcurves. *Astrophys. J.*, **2020**.
DOI: `10.3847/1538-4357/ab93bf` ARXIV: `2003.06733 [astro-ph.HE]` `2`

[59] Matt Nicholl, Ben Margalit, Patricia Schmidt, Graham P. Smith, Evan J. Ridley, and James Nuttall. Tight multimessenger constraints on the neutron star equation of state from GW170817 and a forward model for kilonova light-curve synthesis. *Mon. Not. Roy. Astron. Soc.*, **2021**.

DOI: 10.1093/mnras/stab1523 ARXIV: 2102.02229 [astro-ph.HE] 2

[60] Giacomo Ricigliano, Albino Perego, Ssohrab Borhanian, Eleonora Loffredo, Kyohei Kawaguchi, Sebastiano Bernuzzi, and Lukas Chris Lippold. xkn: a semi-analytic framework for the modelling of kilonovae. *Mon. Not. Roy. Astron. Soc.*, **2024**.
DOI: 10.1093/mnras/stae572 ARXIV: 2311.15709 [astro-ph.HE] 2

[61] Daniel Kasen, N. R. Badnell, and Jennifer Barnes. Opacities and Spectra of the r-process Ejecta from Neutron Star Mergers. *Astrophys. J.*, **2013**.
DOI: 10.1088/0004-637X/774/1/25 ARXIV: 1303.5788 [astro-ph.HE] 2, 7

[62] Masaomi Tanaka and Kenta Hotokezaka. Radiative Transfer Simulations of Neutron Star Merger Ejecta. *Astrophys. J.*, **2013**.
DOI: 10.1088/0004-637X/775/2/113 ARXIV: 1306.3742 [astro-ph.HE] 2, 7

[63] Ryan T. Wollaeger, Oleg Korobkin, Christopher J. Fontes, Stephan K. Rosswog, Wesley P. Even, Christopher L. Fryer, Jesper Sollerman, Aimee L. Hungerford, Daniel R. van Rossum, and Allan B. Wollaber. Impact of ejecta morphology and composition on the electromagnetic signatures of neutron star mergers. *Mon. Not. Roy. Astron. Soc.*, **2018**.
DOI: 10.1093/mnras/sty1018 ARXIV: 1705.07084 [astro-ph.HE] 2, 7

[64] Mattia Bulla. POSSIS: predicting spectra, light curves and polarization for multi-dimensional models of supernovae and kilonovae. *Mon. Not. Roy. Astron. Soc.*, **2019**.
DOI: 10.1093/mnras/stz2495 ARXIV: 1906.04205 [astro-ph.HE]
2, 3, 7, 15, 16, 18

[65] J. H. Gillanders, S. J. Smartt, S. A. Sim, A. Bauswein, and S. Goriely. Modelling the spectra of the kilonova AT2017gfo – I. The photospheric epochs. *Mon. Not. Roy. Astron. Soc.*, **2022**.
DOI: 10.1093/mnras/stac1258 ARXIV: 2202.01786 [astro-ph.HE] 2, 7

[66] Christine E. Collins, Andreas Bauswein, Stuart A. Sim, Vimal Vijayan, Gabriel Martínez-Pinedo, Oliver Just, Luke J. Shingles, and Markus Kromer. 3D radiative transfer kilonova modelling for binary neutron star merger simulations. *Mon. Not. Roy. Astron. Soc.*, **2023**.
DOI: 10.1093/mnras/stad606 ARXIV: 2209.05246 [astro-ph.HE] 2, 7

[67] J. Heinzel, M. W. Coughlin, T. Dietrich, M. Bulla, S. Antier, N. Christensen, D. A. Coulter, R. J. Foley, L. Issa, and N. Khetan. Comparing inclination dependent analyses of kilonova transient. *Mon. Not. Roy. Astron. Soc.*, **2021**.
DOI: 10.1093/mnras/stab221 ARXIV: 2010.10746 [astro-ph.HE] 2, 37, 42

[68] Oleg Korobkin et al. Axisymmetric Radiative Transfer Models of Kilonovae. *Astrophys. J.*, **2021**.
DOI: 10.3847/1538-4357/abe1b5 ARXIV: 2004.00102 [astro-ph.HE] 2

[69] Donggeun Tak, Z. Lucas Uhm, and James H. Gillanders. Exploring the Impact of the Ejecta Velocity Profile on the Evolution of Kilonova: Diversity of the Kilonova Lightcurves. *Astrophys. J.*, **2023**.
DOI: `10.3847/1538-4357/ad06b0` arXiv: `2310.15608 [astro-ph.HE]`   2

[70] Chris L. Fryer, Aimee L. Hungerford, Ryan T. Wollaeger, Jonah M. Miller, Soumi De, Christopher J. Fontes, Oleg Korobkin, Atul Kedia, Marko Ristic, and Richard O'Shaughnessy. The Effect of the Velocity Distribution on Kilonova Emission. *Astrophys. J.*, **2024**.
DOI: `10.3847/1538-4357/ad1036` arXiv: `2311.05005 [astro-ph.HE]`   2

[71] Donggeun Tak, Z. Lucas Uhm, and James H. Gillanders. Impact of Ejecta Temperature and Mass on the Strength of Heavy Element Signatures in Kilonovae. *Astrophys. J.*, **2024**.
DOI: `10.3847/1538-4357/ad3af4` arXiv: `2402.05471 [astro-ph.HE]`   2

[72] Jennifer Barnes, Y. L. Zhu, K. A. Lund, T. M. Sprouse, N. Vassh, G. C. McLaughlin, M. R. Mumpower, and R. Surman. Kilonovae Across the Nuclear Physics Landscape: The Impact of Nuclear Physics Uncertainties on r-process-powered Emission. *Astrophys. J.*, **2021**.
DOI: `10.3847/1538-4357/ac0aec` arXiv: `2010.11182 [astro-ph.HE]`   3

[73] Yonglin Zhu, Jennifer Barnes, K. A. Lund, T. M. Sprouse, N. Vassh, G. C. McLaughlin, M. R. Mumpower, and R. Surman. The Impact of Nuclear Physics Uncertainties on Interpreting Kilonova Light Curves. *EPJ Web Conf.*, **2022**.
DOI: `10.1051/epjconf/202226003004`   3

[74] Mattia Bulla. The critical role of nuclear heating rates, thermalization efficiencies, and opacities for kilonova modelling and parameter inference. *Mon. Not. Roy. Astron. Soc.*, **2023**.
DOI: `10.1093/mnras/stad232` arXiv: `2211.14348 [astro-ph.HE]`
3 , 37 , 39 , 55 , 63

[75] Daniel Brethauer, Daniel Kasen, Raffaella Margutti, and Ryan Chornock. Impact of Systematic Modeling Uncertainties on Kilonova Property Estimation, **2024**.
DOI: `10.3847/1538-4357/ad7d83` arXiv: `2408.02731 [astro-ph.HE]`   3

[76] Nikhil Sarin and Stephan Rosswog. Cautionary tales on heating-rate prescriptions in kilonovae, **2024**.
DOI: `10.3847/2041-8213/ad739d` arXiv: `2404.07271 [astro-ph.HE]`   3 , 63

[77] Ryan T. Wollaeger et al. On a Spectral Method for β-particle Bound Excitation Collisions in Kilonovae. *Astrophys. J.*, **2024**.
DOI: `10.3847/1538-4357/ad37f9` arXiv: `2401.11069 [astro-ph.HE]`   3

[78] Ben Shenhar, Or Guttman, and Eli Waxman. An analytic description of electron thermalization in kilonovae ejecta. *Mon. Not. Roy. Astron. Soc.*, **2024**. DOI: 10.1093/mnras/stae1218 ARXIV: 2403.08765 [astro-ph.HE] 3, 39

[79] Or Guttman, Ben Shenhar, Arnab Sarkar, and Eli Waxman. The thermalization of γ-rays in radioactive expanding ejecta: a simple model and its application for Kilonovae and Ia SNe. *Mon. Not. Roy. Astron. Soc.*, **2024**. DOI: 10.1093/mnras/stae1795 ARXIV: 2403.08769 [astro-ph.HE] 3

[80] Nikhil Sarin and Paul D. Lasky. The evolution of binary neutron star post-merger remnants: a review. *General Relativity and Gravitation*, **2021**. DOI: 10.1007/s10714-021-02831-1 ARXIV: 2012.08172 [astro-ph.HE] 4

[81] J Robert Oppenheimer and George M Volkoff. On massive neutron cores. *Physical Review*, **1939**. DOI: 10.1103/PhysRev.55.374 4

[82] Richard Chace Tolman. Relativity, thermodynamics, and cosmology. Courier Corporation, **1987**. 4

[83] Albert Einstein. Approximative Integration of the Field Equations of Gravitation. *Sitzungsber. Preuss. Akad. Wiss. Berlin (Math. Phys.)*, **1916**. 4

[84] Feryal Özel and Paulo Freire. Masses, Radii, and the Equation of State of Neutron Stars. *Annual Review of Astronomy and Astrophysics*, **2016**. DOI: 10.1146/annurev-astro-081915-023322 ARXIV: 1603.02698 [astro-ph.HE] 6

[85] Andrew W. Steiner, James M. Lattimer, and Edward F. Brown. The Neutron Star Mass-Radius Relation and the Equation of State of Dense Matter. *Astrophys. J. Lett.*, **2013**. DOI: 10.1088/2041-8205/765/1/L5 ARXIV: 1205.6871 [nucl-th] 6

[86] Thomas E. Riley et al. A NICER View of the Massive Pulsar PSR J0740+6620 Informed by Radio Timing and XMM-Newton Spectroscopy. *The Astrophysical Journal Letters*, **2021**. DOI: 10.3847/2041-8213/ac0a81 ARXIV: 2105.06980 [astro-ph.HE] 6

[87] B. D. Metzger, G. Martinez-Pinedo, S. Darbha, E. Quataert, A. Arcones, D. Kasen, R. Thomas, P. Nugent, I. V. Panov, and N. T. Zinner. Electromagnetic Counterparts of Compact Object Mergers Powered by the Radioactive Decay of R-process Nuclei. *Mon. Not. Roy. Astron. Soc.*, **2010**. DOI: 10.1111/j.1365-2966.2010.16864.x ARXIV: 1001.5029 [astro-ph.HE] 6, 7, 11

[88] N. Gehrels et al. A new -ray burst classification scheme from GRB 060614. *Nature*, **2006**.

7

[89] A. Gal-yam et al. A novel explosive process is required for the -ray burst GRB
      060614. *Nature*, **2006**.

7

[90] Zhi-Ping Jin, Stefano Covino, Neng-Hui Liao, Xiang Li, Paolo D'Avanzo,
      Yi-Zhong Fan, and Da-Ming Wei. A kilonova associated with GRB 070809.
      Nature Astron., **2020**.
      ARXIV: 1901.06269 [astro-ph.HE]   7

[91] D. A. Perley et al. GRB 080503: Implications of a Naked Short Gamma-Ray
      Burst Dominated by Extended Emission., **2009**.
      DOI: 10.1088/0004-637X/696/2/1871 ARXIV: 0811.1044 [astro-ph]   7

[92] N. R. Tanvir, A. J. Levan, A. S. Fruchter, J. Hjorth, R. A. Hounsell, K.
      Wiersema, and R. L. Tunnicliffe. A 'kilonova' associated with the short-duration
       -ray burst GRB 130603B. *Nature*, **2013**.
      DOI: 10.1038/nature12505   7

[93] K. Hotokezaka, K. Kiuchi, K. Kyutoku, H. Okawa, Y.-I. Sekiguchi, M. Shi-
      bata, and K. Taniguchi. Mass ejection from the merger of binary neutron stars.
      Phys. Rev. D, 024001, **2013**.
      DOI: 10.1103/PhysRevD.87.024001 ARXIV: 1212.0905 [astro-ph.HE]   7, 8

[94] D. Radice, F. Galeazzi, J. Lippuner, L. F. Roberts, C. D. Ott, and L. Rez-
      zolla. Dynamical Mass Ejection from Binary Neutron Star Mergers. *Mon. Not.
      R. Astron. Soc.*, **2016**.
      DOI: 10.1093/mnras/stw1227 ARXIV: 1601.02426 [astro-ph.HE]   7, 8

[95] Luke Bovard, Dirk Martin, Federico Guercilena, Almudena Arcones, Luciano
      Rezzolla, and Oleg Korobkin. r -process nucleosynthesis from matter ejected
      in binary neutron star mergers., 124005, **2017**.
      DOI: 10.1103/PhysRevD.96.124005 ARXIV: 1709.09630 [gr-qc]   7

[96] S. Rosswog, N. Sarin, E. Nakar, and P. Diener. Fast dynamic ejecta in neutron
      star mergers. **2025**.
      ARXIV: 2411.18813 [astro-ph.HE] URL: https://arxiv.org/abs/2411.18813
                                                                               7

[97] W. E. East, F. Pretorius, and B. C. Stephens. Eccentric black hole-neutron
      star mergers: Effects of black hole spin and equation of state. *Phys. Rev. D*,
      124009, **2012**.
      DOI: 10.1103/PhysRevD.85.124009 ARXIV: 1111.3055 [astro-ph.HE]   7

[98] R. Gold, S. Bernuzzi, M. Thierfelder, B. Brügmann, and F. Pretorius. Ec-
      centric binary neutron star mergers. *Phys. Rev. D*, 121501, **2012**.
      DOI: 10.1103/PhysRevD.86.121501 ARXIV: 1109.5128 [gr-qc]   7

[99]   D. Tsang. Shattering Flares during Close Encounters of Neutron Stars. *Astrophys. J.*, 103, **2013**.
DOI: 10.1088/0004-637X/777/2/103   arXiv: 1307.3554 [astro-ph.HE]   7

[100] Tim Dietrich, Sebastiano Bernuzzi, Maximiliano Ujevic, and Wolfgang Tichy. Gravitational waves and mass ejecta from binary neutron star mergers: Effect of the stars' rotation. *Physical Review D*, 044045, **2017**.
DOI: 10.1103/PhysRevD.95.044045   arXiv: 1611.07367 [gr-qc]   8

[101] William E. East, Vasileios Paschalidis, Frans Pretorius, and Antonios Tsokaros. Binary neutron star mergers: effects of spin and post-merger dynamics. *arXiv e-prints*, arXiv:1906.05288, **2019**.
DOI: 10.1103/PhysRevD.100.124042   arXiv: 1906.05288 [astro-ph.HE]   8

[102] Elias R. Most, L. Jens Papenfort, Antonios Tsokaros, and Luciano Rezzolla. Impact of high spins on the ejection of mass in GW170817. *arXiv e-prints*, arXiv:1904.04220, **2019**.
DOI: 10.3847/1538-4357/ab3ebb   arXiv: 1904.04220 [astro-ph.HE]   8

[103] K. Kyutoku, K. Ioka, and M. Shibata. Anisotropic mass ejection from black hole-neutron star binaries: Diversity of electromagnetic counterparts. *Phys. Rev. D*, 041503, **2013**.
DOI: 10.1103/PhysRevD.88.041503   arXiv: 1305.6309 [astro-ph.HE]   8

[104] K. Kyutoku, K. Ioka, H. Okawa, M. Shibata, and K. Taniguchi. Dynamical mass ejection from black hole-neutron star binaries. *Phys. Rev. D*, 044028, **2015**.
DOI: 10.1103/PhysRevD.92.044028   arXiv: 1502.05402 [astro-ph.HE]   8

[105] F. Foucart, D. Desai, W. Brege, M. D. Duez, D. Kasen, D. A. Hemberger, L. E. Kidder, H. P. Pfeiffer, and M. A. Scheel. Dynamical ejecta from precessing neutron star-black hole mergers with a hot, nuclear-theory based equation of state. *Classical and Quantum Gravity*, 044002, **2017**.
DOI: 10.1088/1361-6382/aa573b   arXiv: 1611.01159 [astro-ph.HE]   8

[106] R. Oechslin, H.-T. Janka, and A. Marek. Relativistic neutron star merger simulations with non-zero temperature equations of state. I. Variation of binary parameters and equation of state. *Astron. Astrophys.*, **2007**.
DOI: 10.1051/0004-6361:20066682   eprint: astro-ph/0611047   8

[107] A. Bauswein, S. Goriely, H. J. M. Astrophysics, Garching, and Universite Libre de Bruxelles. SYSTEMATICS OF DYNAMICAL MASS EJECTION, NUCLEOSYNTHESIS, AND RADIOACTIVELY POWERED ELECTROMAGNETIC SIGNALS FROM NEUTRON-STAR MERGERS. *The Astrophysical Journal*, **2013**.
DOI: 10.1088/0004-637X/773/1/78   arXiv: 1302.6530 [astro-ph.SR]   8, 12

[108] L. Lehner, S. L. Liebling, C. Palenzuela, O. L. Caballero, E. O'Connor,

M. Anderson, and D. Neilsen. Unequal mass binary neutron star mergers and multimessenger signals. *Class. Quantum Grav.*, 184002, **2016**.
DOI: 10.1088/0264-9381/33/18/184002 ARXIV: 1603.00501 [gr-qc] 8

[109] K. Kawaguchi, K. Kyutoku, H. Nakano, H. Okawa, M. Shibata, and K. Taniguchi. Black hole-neutron star binary merger: Dependence on black hole spin orientation and equation of state. *Phys. Rev. D*, 024014, **2015**.
DOI: 10.1103/PhysRevD.92.024014 ARXIV: 1506.05473 [astro-ph.HE] 8

[110] S. Goriely, A. Bauswein, and H.-T. Janka. *r*-process Nucleosynthesis in Dynamically Ejected Matter of Neutron Star Mergers. *Astrophys. J. Lett.*, L32, **2011**.
DOI: 10.1088/2041-8205/738/2/L32 ARXIV: 1107.0899 [astro-ph.SR] 8

[111] O Korobkin, Stephan Rosswog, A Arcones, and C Winteler. On the astrophysical robustness of the neutron star merger r-process. *Monthly Notices of the Royal Astronomical Society*, **2012**.
8, 11

[112] Joel Jesús Mendoza-Temis, Meng-Ru Wu, Karlheinz Langanke, Gabriel Martínez-Pinedo, Andreas Bauswein, and Hans-Thomas Janka. Nuclear robustness of the *r* process in neutron-star mergers. *Phys. Rev. C*, **2015**.
DOI: 10.1103/PhysRevC.92.055805 8

[113] Y. Sekiguchi, K. Kiuchi, K. Kyutoku, and M. Shibata. Dynamical mass ejection from binary neutron star mergers: Radiation-hydrodynamics study in general relativity. *Phys. Rev. D*, 064059, **2015**.
DOI: 10.1103/PhysRevD.91.064059 ARXIV: 1502.06660 [astro-ph.HE] 8

[114] S. Wanajo, Y. Sekiguchi, N. Nishimura, K. Kiuchi, K. Kyutoku, and M. Shibata. Production of All the *r*-process Nuclides in the Dynamical Ejecta of Neutron Star Mergers. *Astrophys. J.*, L39, **2014**.
DOI: 10.1088/2041-8205/789/2/L39 ARXIV: 1402.7317 [astro-ph.SR] 8

[115] R. Oechslin and H.-T. Janka. Torus formation in neutron star mergers and well-localized short gamma-ray bursts. *Mon. Not. R. Astron. Soc.*, **2006**.
DOI: 10.1111/j.1365-2966.2006.10238.x eprint: arXiv:astro-ph/0507099 8

[116] B. D. Metzger, A. L. Piro, and E. Quataert. Neutron-rich freeze-out in viscously spreading accretion discs formed from compact object mergers. *Mon. Not. R. Astron. Soc.*, **2009**.
DOI: 10.1111/j.1365-2966.2008.14380.x ARXIV: 0810.2535 8, 9

[117] O. Just, A. Bauswein, R. A. Pulpillo, S. Goriely, and H.-T. Janka. Comprehensive nucleosynthesis analysis for ejecta of compact binary mergers. *Mon. Not. R. Astron. Soc.*, **2015**.
DOI: 10.1093/mnras/stv009 ARXIV: 1406.2687 [astro-ph.SR] 8, 9

[118] R. Popham, S. E. Woosley, and C. Fryer. Hyperaccreting Black Holes and Gamma-Ray Bursts. *Astrophys. J.*, **1999**.
DOI: `10.1086/307259`   eprint: `astro-ph/9807028`   9

[119] A. Perego, S. Rosswog, R. M. Cabezón, O. Korobkin, R. Käppeli, A. Arcones, and M. Liebendörfer. Neutrino-driven winds from neutron star merger remnants. *Mon. Not. R. Astron. Soc.*, **2014**.
DOI: `10.1093/mnras/stu1352`   arXiv: `1405.6730 [astro-ph.HE]`   9

[120] D. Martin, A. Perego, A. Arcones, F.-K. Thielemann, O. Korobkin, and S. Rosswog. Neutrino-driven Winds in the Aftermath of a Neutron Star Merger: Nucleosynthesis and Electromagnetic Transients. *Astrophys. J.*, 2, **2015**.
DOI: `10.1088/0004-637X/813/1/2`   arXiv: `1506.05048 [astro-ph.SR]`   9

[121] S. Richers, D. Kasen, E. O'Connor, R. Fernández, and C. D. Ott. Monte Carlo Neutrino Transport through Remnant Disks from Neutron Star Mergers. *Astrophys. J.*, 38, **2015**.
DOI: `10.1088/0004-637X/813/1/38`   arXiv: `1507.03606 [astro-ph.HE]`   9

[122] Vsevolod Nedora, Sebastiano Bernuzzi, David Radice, Albino Perego, Andrea Endrizzi, and Néstor Ortiz. Spiral-wave wind for the blue kilonova. *arXiv e-prints*, arXiv:1907.04872, **2019**.
DOI: `10.3847/2041-8213/ab5794`   arXiv: `1907.04872 [astro-ph.HE]`   9

[123] B. D. Metzger, A. L. Piro, and E. Quataert. Time-dependent models of accretion discs formed from compact object mergers., **2008**.
DOI: `10.1111/j.1365-2966.2008.13789.x`   arXiv: `0805.4415 [astro-ph]` 9

[124] W. H. Lee, E. Ramirez-Ruiz, and D. López-Cámara. Phase Transitions and He-Synthesis-Driven Winds in Neutrino Cooled Accretion Disks: Prospects for Late Flares in Short Gamma-Ray Bursts. *Astrophys. J. Lett.*, **2009**.
DOI: `10.1088/0004-637X/699/2/L93`   arXiv: `0904.3752`   9

[125] A. M. Beloborodov. Hyper-accreting black holes. In: *Cool Discs, Hot Flows: The Varying Faces of Accreting Compact Objects*. Ed. by M. Axelsson. American Institute of Physics, **2008**.
DOI: `10.1063/1.3002509`   arXiv: `0810.2690`   9

[126] K. Kohri, R. Narayan, and T. Piran. Neutrino-dominated Accretion and Supernovae. *Astrophys. J.*, **2005**.
DOI: `10.1086/431354`   eprint: `astro-ph/0502470`   9

[127] R. Fernández and B. D. Metzger. Delayed outflows from black hole accretion tori following neutron star binary coalescence. *Mon. Not. R. Astron. Soc.*, **2013**.
DOI: `10.1093/mnras/stt1312`   arXiv: `1304.6720 [astro-ph.HE]`   9

[128] M.-R. Wu, R. Fernández, G. Martínez-Pinedo, and B. D. Metzger. Production of the entire range of r-process nuclides by black hole accretion disk outflows from neutron star mergers. *Mon. Not. R. Astron. Soc.*, **2016**.

DOI: 10.1093/mnras/stw2156   ARXIV: 1607.05290 [astro-ph.HE]   9

[129]   Daniel Kasen, Rodrigo Fernandez, and Brian Metzger. Kilonova light curves from the disc wind outflows of compact object mergers. *Mon. Not. Roy. Astron. Soc.*, **2015**.
DOI: 10.1093/mnras/stv721   ARXIV: 1411.3726 [astro-ph.HE]   9

[130]   Jonas Lippuner, Rodrigo Fernández, Luke F. Roberts, Francois Foucart, Daniel Kasen, Brian D. Metzger, and Christian D. Ott. Signatures of hypermassive neutron star lifetimes on r-process nucleosynthesis in the disc ejecta from neutron star mergers., **2017**.
DOI: 10.1093/mnras/stx1987   ARXIV: 1703.06216 [astro-ph.HE]   9

[131]   Daniel M. Siegel and Brian D. Metzger. Three-Dimensional General-Relativistic Magnetohydrodynamic Simulations of Remnant Accretion Disks from Neutron Star Mergers: Outflows and r -Process Nucleosynthesis., 231102, **2017**.
DOI: 10.1103/PhysRevLett.119.231102   ARXIV: 1705.05473 [astro-ph.HE]   9

[132]   Rodrigo Fernández, Alexander Tchekhovskoy, Eliot Quataert, Francois Foucart, and Daniel Kasen. Long-term GRMHD simulations of neutron star merger accretion discs: implications for electromagnetic counterparts., **2019**.
DOI: 10.1093/mnras/sty2932   ARXIV: 1808.00461 [astro-ph.HE]   9

[133]   Brian D. Metzger and Rodrigo Fernández. Red or blue? A potential kilonova imprint of the delay until black hole formation following a neutron star merger. *Monthly Notices of the Royal Astronomical Society*, **2014**.
DOI: 10.1093/mnras/stu802   ARXIV: 1402.4803 [astro-ph.HE]   9

[134]   Steven Fahlman and Rodrigo Fernández. Hypermassive Neutron Star Disk Outflows and Blue Kilonovae., L3, **2018**.
DOI: 10.3847/2041-8213/aaf1ab   ARXIV: 1811.08906 [astro-ph.HE]   9

[135]   T. A. Thompson, P. Chang, and E. Quataert. Magnetar Spin-Down, Hyperenergetic Supernovae, and Gamma-Ray Bursts. *Astrophys. J.*, **2004**.
DOI: 10.1086/421969   eprint: astro-ph/0401555   9

[136]   Brian D. Metzger, Todd A. Thompson, and Eliot Quataert. A Magnetar Origin for the Kilonova Ejecta in GW170817., 101, **2018**.
DOI: 10.3847/1538-4357/aab095   ARXIV: 1801.04286 [astro-ph.HE]   9

[137]   Daniel M. Siegel and Brian D. Metzger. Three-dimensional GRMHD Simulations of Neutrino-cooled Accretion Disks from Neutron Star Mergers., 52, **2018**.
DOI: 10.3847/1538-4357/aabaec   ARXIV: 1711.00868 [astro-ph.HE]   9

[138]   K. Kiuchi, Y. Sekiguchi, K. Kyutoku, M. Shibata, K. Taniguchi, and T. Wada. High resolution magnetohydrodynamic simulation of black hole-neutron star merger: Mass ejection and short gamma ray bursts. *Phys. Rev. D*, 064034, **2015**.
DOI: 10.1103/PhysRevD.92.064034   ARXIV: 1506.06811 [astro-ph.HE]   9

[139] Jonas Lippuner and Luke F Roberts. r-Process lanthanide production and
       heating rates in kilonovae. *The Astrophysical Journal*, **2015**.
       DOI: 10.1088/0004-637X/815/2/82 ARXIV: 1508.03133 [astro-ph.HE]   10

[140] Albert Sneppen and Darach Watson. Discovery of a 760 nm P Cygni line in
       AT2017gfo: Identification of yttrium in the kilonova photosphere. *Astronomy
       amp; Astrophysics*, **2023**.
       DOI: 10.1051/0004-6361/202346421 ARXIV: 2306.14942 [astro-ph.HE]   10

[141] W David Arnett. Type I supernovae. I-Analytic solutions for the early part of
       the light curve. *Astrophysical Journal, Part 1, vol. 253, Feb. 15, 1982, p.
       785-797.*, **1982**.
       DOI: 10.1086/159681   12

[142] Masaomi Tanaka, Daiji Kato, Gediminas Gaigalas, and Kyohei Kawaguchi.
       Systematic Opacity Calculations for Kilonovae. *Mon. Not. Roy. Astron. Soc.*,
       2020.
       DOI: 10.1093/mnras/staa1576 ARXIV: 1906.08914 [astro-ph.HE]
                                                          12, 17, 37, 39, 55, 63

[143] S. Rosswog, O. Korobkin, A. Arcones, F. Thielemann, T. University, Okc, I.
       Darmstadt, U. Basel, and R. I. O. Physics. The long-term evolution of neutron
       star merger remnants – I. The impact of r-process nucleosynthesis. *Monthly
       Notices of the Royal Astronomical Society*, **2013**.
       DOI: 10.1093/mnras/stt2502 ARXIV: 1307.2939 [astro-ph.HE]   12

[144] Nicholas Metropolis, Arianna W Rosenbluth, Marshall N Rosenbluth, Au-
       gusta H Teller, and Edward Teller. Equation of state calculations by fast com-
       puting machines. *The journal of chemical physics*, **1953**.
       DOI: 10.1063/1.1699114   25

[145] W Keith Hastings. Monte Carlo sampling methods using Markov chains and
       their applications, **1970**.
       DOI: 10.1093/biomet/57.1.97   25

[146] John Skilling. Nested sampling. *Bayesian inference and maximum entropy
       methods in science and engineering*, **2004**.
       DOI: 10.1007/s11222-010-9198-8 ARXIV: 0912.2380 [stat.CO]   27

[147] G. Ashton et al. Nested sampling for physical scientists. *Nature Reviews Meth-
       ods Primers*, **2022**.
       DOI: 10.1038/s43586-022-00121-x ARXIV: 2205.15570 [stat.CO]   28

[148] Gregory Ashton et al. Bilby: A User-friendly Bayesian Inference Library for
       Gravitational-wave Astronomy. *The Astrophysical Journal Supplement Series*,
       2019.
       DOI: 10.3847/1538-4365/ab06fc ARXIV: 1811.02042 [astro-ph.IM]   30

[149] Rory J E Smith, Gregory Ashton, Avi Vajpeyi, and Colm Talbot. Massively

parallel Bayesian inference for transient gravitational-wave astronomy. *Monthly Notices of the Royal Astronomical Society*, **2020**.
DOI: 10.1093/mnras/staa2483 ARXIV: 1909.11873 [gr-qc]   30

[150] Tsun Ho Pang. From spacetime to nucleus: Probing nuclear physics and testing general relativity. English. Doctoral thesis 1 (Research UU / Graduation UU). Universiteit Utrecht, **2022**.
DOI: 10.33540/1550   31, 32

[151] Peter T. H. Pang et al. An updated nuclear-physics and multi-messenger astrophysics framework for binary neutron star mergers. *Nature Communications*, **2023**.
DOI: 10.1038/s41467-023-43932-6 ARXIV: 2205.08513 [astro-ph.HE]
                                                         31, 32, 37, 42

[152] LIGO Scientific Collaboration. LALSuite: LIGO Scientific Collaboration Algorithm Library Suite. Astrophysics Source Code Library, record ascl:2012.021. **2020**.
                                                                          31

[153] G. Ryan, H. V. Eerten, L. Piro, and E. Troja. Gamma-Ray Burst Afterglows in the Multimessenger Era: Numerical Models and Closure Relations. *The Astrophysical Journal*, **2019**.
DOI: 10.3847/1538-4357/ab93cf ARXIV: 1909.11691 [astro-ph.HE]   32

[154] H. van Eerten, Weiqun Zhang, and A. MacFadyen. OFF-AXIS GAMMA-RAY BURST AFTERGLOW MODELING BASED ON A TWO-DIMENSIONAL AXISYMMETRIC HYDRODYNAMICS SIMULATION. *The Astrophysical Journal*, **2010**.
DOI: 10.1088/0004-637X/722/1/235 ARXIV: 1006.5125 [astro-ph.HE]   32

[155] Peter T. H. Pang, Ingo Tews, Michael W. Coughlin, Mattia Bulla, Chris Van Den Broeck, and Tim Dietrich. Nuclear Physics Multimessenger Astrophysics Constraints on the Neutron Star Equation of State: Adding NICER's PSR J0740+6620 Measurement. *The Astrophysical Journal*, **2021**.
DOI: 10.3847/1538-4357/ac19ab ARXIV: 2105.08688 [astro-ph.HE]   32

[156] M. Coughlin, T. Dietrich, Zoheyr Doctor, D. Kasen, S. Coughlin, A. Jerkstrand, G. Leloudas, O. McBrien, B. Metzger, R. O'Shaughnessy, and S. Smartt. Constraints on the neutron star equation of state from AT2017gfo using radiative transfer simulations. *Monthly Notices of the Royal Astronomical Society*, **2018**.
DOI: 10.1093/mnras/sty2174 ARXIV: 1805.09371 [astro-ph.HE]   33

[157] Carl E. Rasmussen and Christopher K. I. Williams. Gaussian Processes for Machine Learning. IN: *Adaptive computation and machine learning*. **2005**.
                                                                          34

[158] Fabian Pedregosa et al. Scikit-learn: Machine Learning in Python. *ArXiv*, **2011**.
ArXiv: 1201.0490 [cs.LG] 34

[159] M. Almualla, Yuhong Ning, P. Salehi, M. Bulla, T. Dietrich, M. Coughlin, and N. Guessoum. Using Neural Networks to Perform Rapid High-Dimensional Kilonova Parameter Inference. In: **2021**.
ArXiv: 2112.15470 [astro-ph.HE] 34

[160] Martín Abadi et al. TensorFlow: Large-Scale Machine Learning on Heterogeneous Systems. Software available from tensorflow.org. **2015**.
URL: https://www.tensorflow.org/ 34

[161] Diederik P. Kingma and Jimmy Ba. Adam: A Method for Stochastic Optimization. In: **2014**.
ArXiv: 1412.6980 [cs.LG] 34

[162] Vinod Nair and Geoffrey E. Hinton. Rectified linear units improve restricted boltzmann machines. In: *Proceedings of the 27th International Conference on International Conference on Machine Learning*. Omnipress, **2010**.
34

[163] D. A. Kann et al. GRANDMA and HXMT Observations of GRB 221009A: The Standard Luminosity Afterglow of a Hyperluminous Gamma-Ray Burst—In Gedenken an David Alexander Kann. *Astrophys. J. Lett.*, **2023**.
DOI: 10.3847/2041-8213/acc8d0 ArXiv: 2302.06225 [astro-ph.HE] 37

[164] Yinglei Peng, Marko Ristić, Atul Kedia, Richard O'Shaughnessy, Christopher J. Fontes, Chris L. Fryer, Oleg Korobkin, Matthew R. Mumpower, V. Ashley Villar, and Ryan T. Wollaeger. Kilonova light-curve interpolation with neural networks. *Phys. Rev. Res.*, **2024**.
DOI: 10.1103/PhysRevResearch.6.033078 ArXiv: 2402.05871 [astro-ph.HE]
37

[165] Matteo Breschi, Rossella Gamba, Gregorio Carullo, Daniel Godzieba, Sebastiano Bernuzzi, Albino Perego, and David Radice. Bayesian inference of multimessenger astrophysical data: Joint and coherent inference of gravitational waves and kilonovae. *Astron. Astrophys.*, **2024**.
DOI: 10.1051/0004-6361/202449173 ArXiv: 2401.03750 [astro-ph.HE] 37

[166] Quentin Pognan, Anders Jerkstrand, and Jon Grumer. NLTE effects on kilonova expansion opacities. *Mon. Not. Roy. Astron. Soc.*, **2022**.
DOI: 10.1093/mnras/stac1253 ArXiv: 2202.09245 [astro-ph.HE] 37, 39, 55

[167] Quentin Pognan, Anders Jerkstrand, and Jon Grumer. On the validity of steady-state for nebular phase kilonovae. *Mon. Not. Roy. Astron. Soc.*, **2022**.
DOI: 10.1093/mnras/stab3674 ArXiv: 2112.07484 [astro-ph.HE] 37, 55

[168] A Flörs, R F Silva, J Deprince, H Carvajal Gallego, G Leck, L J Shingles, G Martínez-Pinedo, J M Sampaio, P Amaro, J P Marques, S Goriely, P

Quinet, P Palmeri, and M Godefroid. Opacities of singly and doubly ionized neodymium and uranium for kilonova emission modeling. *Monthly Notices of the Royal Astronomical Society*, **2023**.
DOI: 10.1093/mnras/stad2053 ARXIV: 2302.01780 [astro-ph.HE]   39

[169]   Jennifer Barnes, Daniel Kasen, Meng-Ru Wu, and Gabriel Martínez-Pinedo. RADIOACTIVITY AND THERMALIZATION IN THE EJECTA OF COMPACT OBJECT MERGERS AND THEIR IMPACT ON KILONOVA LIGHT CURVES. *The Astrophysical Journal*, **2016**.
DOI: 10.3847/0004-637x/829/2/110 ARXIV: 1605.07218 [astro-ph.HE]   39

[170]   S. Dhawan, M. Bulla, A. Goobar, A. Sagués Carracedo, and C. N. Setzer. Constraining the Observer Angle of the Kilonova AT2017gfo Associated with GW170817: Implications for the Hubble Constant. *The Astrophysical Journal*, **2020**.
DOI: 10.3847/1538-4357/ab5799 ARXIV: 1909.13810 [astro-ph.HE]   39

[171]   Y. Shvartzvald et al. ULTRASAT: A Wide-field Time-domain UV Space Telescope. *Astrophys. J.*, **2024**.
DOI: 10.3847/1538-4357/ad2704 ARXIV: 2304.14482 [astro-ph.IM]   55

[172]   Daiji Kato, Masaomi Tanaka, Gediminas Gaigalas, Laima Kitovienė, and Pavel Rynkun. Systematic opacity calculations for kilonovae – II. Improved atomic data for singly ionized lanthanides. **2025**.
ARXIV: 2501.13286 [astro-ph.HE] URL: https://arxiv.org/abs/2501.13286
63